

ABSTRACT

CRILL, JOHN WESLEY. Ad-hoc Solutions for Capturing Electronic Structure Details in Classical Dynamics Simulations. (Under the direction of Prof. Donald W. Brenner. and Prof. Douglas L. Irving.)

Traditional empirical potentials used in molecular dynamics (MD) simulations replace an explicit treatment of the electronic structure with an appropriate interatomic potential energy expression. This enables MD simulations to model atomistic processes, such as dislocation dynamics and plastic deformation, which typically require size and time domains exceeding what is currently feasible with computationally-demanding first principles techniques. However, discarding the electronic degrees of freedom prevents MD simulations from properly resolving certain phenomena which are dominated by electronic interactions. One example is thermal transport in metals, which is often underestimated by orders of magnitude in MD simulations. A recently-developed multi-scale simulation approach, allowing ad-hoc feedback from continuum heat flow solutions to thermostat atoms in an MD simulation, is used to model Joule-heating in nano-scale metallic contacts under electromagnetic stress. The simulations are carried out under conditions representative of contact surfaces in Radio Frequency Electromechanical Switches (RF MEMS) and rail/armature components of Electromagnetic Launchers (EMLs) and are used to speculate on the mechanisms for experimentally-observed material transfer.

Another phenomenon that is typically neglected in MD simulations is charge transfer between atoms of dissimilar electronegativity. A common approach to incorporating a dynamic treatment of charge in a classical potential simulation is to solve atomic charges using an equalization of electronegativity in the charge equilibration (QEq) method. The current work studies the effectiveness of the QEq to mimic the charge distribution properties

of f-center defects in a sodium chloride crystal. The results indicate that the QEq is able to replicate some of the electrostatic energy features of an f-center, which include an extremely localized potential well in the vicinity of the defect.

Ad-hoc Solutions for Capturing Electronic Structure Details in Classical Dynamics
Simulations

by
John Wesley Crill

A dissertation submitted to the Graduate Faculty of
North Carolina State University
in partial fulfillment of the
requirements for the degree of
Doctor of Philosophy

Materials Science and Engineering

Raleigh, North Carolina

2013

APPROVED BY:

Prof. Donald Brenner
Committee Chair

Prof. Douglas Irving
Committee Co-Chair

Prof. Yaroslava Yingling

Prof. Mohammed Zikry

DEDICATION

To Ashley, Vickie, John, and Teresa, for all their love, understanding, and support.

BIOGRAPHY

Wes Crill was born in Durham, North Carolina, on January 24th, 1982. He attended Durham Academy from kindergarten through twelfth grade, dedicating the bare minimum attention to scholastic studies but participating in sporting activities throughout. An early predilection for the quantitative and scientific burgeoned into a desire to pursue engineering, and in the fall of 2000, Wes began his undergraduate studies in Materials Science and Engineering at North Carolina State University. A desire for a career in research resulted in pursuing of a PhD in Materials Science and Engineering with a focus on theory/simulation. Wes ultimately elected to trade in atoms for stocks, and accepted a job in quantitative finance with Dimensional Fund Advisors in Austin, TX, in the summer of 2010. In addition to employment, Wes also found his soulmate in Texas. He married his wife, Ashley, in March of 2013, and became the proud adoptive father to her goldendoodle, Weller.

ACKNOWLEDGEMENTS

In addition to my wife and family, there are many people to whom I would like to express my gratitude for their support throughout the arduous process of the doctoral program.

I wish to thank Professor Donald Brenner for his guidance and support from the beginning. He has made invaluable contributions to my abilities as a researcher, critical thinker, writer, and public speaker. Thanks are also due to Professor Douglas Irving for his assistance along the way, beginning when he was still a post-doctoral researcher and continuing into his days as a faculty member. I'm also grateful to the other members of my committee, Professors Yaroslava Yingling and Mohammed Zikry, for their guidance and suggestions.

I would like to thank Professor Hans Conrad, under whom I developed a desire for research, and without whom I likely would not have pursued graduate studies in materials science.

I'd be remiss if I didn't acknowledge my high school chemistry teacher and home room advisor, Dennis Sullivan, who saw great potential in me and challenged me to achieve big things.

To the O'Quinns, Androneys, Morrisons, and Taveners: thank you for making my time in Raleigh the best experience a guy could ask for.

And finally, I must thank the leaders of the research department at Dimensional for all their patience and understanding during the long struggle of my dissertation process.

TABLE OF CONTENTS

LIST OF TABLES	vi
LIST OF FIGURES	vii
CHAPTER 1 – MOTIVATION	1
1.1 Classes of Atomistic Simulations	1
1.2 Evolution of Empirical Potentials	3
1.3 Multiscale Approaches to Atomistic Simulations	8
1.4 Context of Current Work	13
1.5 References	15
1.6 Tables and Figures	21
CHAPTER 2 – THEORY AND MODELING METHODS	24
2.1 Embedded Atom Method	24
2.2 Molecular Dynamics Simulations	29
2.3 Continuum Principles of Current Flow at Metal-Metal Contacts	31
2.4 Continuum-Atomistic Thermostat	33
2.5 Charge Equilibration	39
2.6 References	44
2.7 Tables and Figures	49
CHAPTER 3 – ASPERITIES UNDER ELECTROMAGNETIC STRESS	54
3.1 Nanotribology	54
3.2 Radio Frequency Micro-Electromechanical Systems	56
3.3 Electromagnetic Launchers	59
3.4 Pull-Apart of Gold RF MEMS Asperity Contacts	61
3.5 Sliding of Asperity Contacts in Electromagnetic Launchers (EMLs)	71
3.6 References	75
3.7 Tables and Figures	80
CHAPTER 4 – MODELING AN F-CENTER WITH THE CHARGE EQUILIBRATION SCHEME	101
4.1 F-centers	101
4.2 Charge Equilibration (QEq) Scheme	105
4.3 Convergence of Lattice Sums	108
4.4 Charge Distribution with an Anionic Vacancy	111
4.5 Charge Distribution with an F-center	112
4.6 Conclusions	114
4.7 References	117
4.8 Tables and Figures	122

LIST OF TABLES

Table 2.1 Parameters used for fitting the pair interaction in the Embedded Atom Method potential for Au.	49
Table 3.1 Atomistic system size and dimensions for the gold asperity contacts.....	80

LIST OF FIGURES

Figure 1.1 Schematic illustration of host atoms' (black dots) electron density (red cloud) contributing to the binding energy of an "embedded" atom (blue dot).	21
Figure 1.2 Schematic illustration of the broadening of density of states as the orbitals of two atoms transition from far apart (a) to overlapped (d).	22
Figure 1.3 Illustration depicting the different bonding characteristics of atoms (red) with the same coordination (three) but different bond character in two different molecules: (a) graphite; (b) $(\text{CH}_3)_2\text{C}=\text{C}(\text{CH}_3)_2$	23
Figure 2.1 Figure from Kelchner et al depicting subsurface dislocation loop formation during nanoindentation	50
Figure 2.2 Multi-scale scheme of Wagner in which the molecular dynamics simulation is embedded within a finite element domain, and continuum heat flow solutions are conveyed to the atoms at the nodal points.	51
Figure 2.3 Illustration of the FD/MD multiscale approach in which a network of resistors is superimposed over an atomistic system, allowing finite difference solutions of continuum thermal and electrical current to be determined.	52
Figure 2.4 Illustration of the increase in current density and heat flow (black lines) and thermal gradients (white lines) as contact area broadens from left to right.	53
Figure 3.1 Schematic illustration of basic classes of RF MEMS switches. Left: Series-configured resistive; Right: Parallel-configured capacitive.	81
Figure 3.2 Left: SEM image of nanowires on failed gold contact surface; Right: schematic illustration of a theoretical mechanism for nanowire formation.	82
Figure 3.3 Schematic illustration of railgun components (top) and operation (bottom).	83
Figure 3.4 Top: Wear on contact surface of armature; Bottom: molten Al accumulated in throat of armature.	84
Figure 3.5 Scale progression of a gold RF MEMS contact surface from (a) fractal model μm -level topography to (b) nm-level single asperity to (c) atomistic tip with \AA -level detail.	85
Figure 3.6 Illustration of atomistic system for the gold RF MEMS asperity contact simulations. Atoms colored by local symmetry. Blue indicates bulk, and red indicates a surface. Crystallographic directions are labeled.	86
Figure 3.7 Sequential snapshots of a null-voltage simulation of nanowire formation and fracture during pull-apart of a gold asperity contact. Simulation time is noted in picoseconds. Atoms colored by symmetry; bulk atoms removed.	87
Figure 3.8 Snapshot of Thompson tetrahedron forming under the surface after 15 picoseconds of pull-apart in a gold asperity contact simulation. Atoms colored by local symmetry; bulk atoms removed.	88

Figure 3.9 Log-log plot of the number of atoms comprising the wire drawn for each initial contact area (blue points) during simulation of pull-apart for gold contacts. A linear regression line fitted to the data is used to extrapolate out to the device-scale contact area of $1 \times 10^6 \text{ nm}^2$ (one square micrometer).	89
Figure 3.10 Sequential configurations from two gold asperity contact pull-apart simulations. Top row: 0.1 V; bottom row: 0.2 V. Atoms colored by local symmetry; bulk atoms (blue) present, but transparent. The apparent disorder in the 0.2 V simulation is from thermal noise.	90
Figure 3.11 Comparison of wire-drawing and deformation after 15 ps of strain for the three gold asperity contact simulations with Joule heating contribution. Atoms colored by local symmetry.	91
Figure 3.12 Electrical potential drop across contact as a function of time during gold contact pull-apart simulation with constant current of 0.01 A and 0.43 V cutoff.	92
Figure 3.13 Temperature evolution during simulation of gold asperity contact pull-apart. Top: 0.01 A; bottom: 0.2 V. Atoms colored by temperature as indicated in the scale.	93
Figure 3.14 Snapshot from simulation of gold asperity contact pull-apart with constant current of 0.01 A after 16 picoseconds with two-volt cutoff employed. Atoms colored by temperature as indicated in scale; all atoms in red are above gold's boiling point of 3239 K.	94
Figure 3.15 Details for atomistic asperity contact used in aluminum/copper sliding simulations.	95
Figure 3.16 Illustration of continuum and atomistic domains for aluminum/copper asperity sliding simulations.	96
Figure 3.17 Snapshots of Al (light gray) asperity sliding on Cu (orange) substrate with 0 V (left) and 0.2 V (right) taken at 5, 10, and 15 picoseconds (top to bottom, respectively). Atoms with bulk symmetry removed.	97
Figure 3.18 Close-up view of stacking faults emanating from the base of an Al asperity inside the Al substrate as the asperity slides on Cu. Atoms with bulk symmetry removed.	98
Figure 3.19 Snapshots of Cu (orange) asperity sliding on Al (silver) substrate with 0 V (left) and 0.2 V (right) taken at 5, 10, and 15 picoseconds (top to bottom, respectively). Atoms with bulk symmetry removed.	99
Figure 3.20 Close-up snapshot of Cu (orange) atoms dissolving in Al (light gray) during sliding of a Cu asperity on an Al substrate with 0.2 V applied. Atoms with bulk symmetry removed. Al atoms made transparent.	100
Figure 4.1 Illustration of $\text{Na}_{14}\text{Cl}_{13}^{1-}$ seed structure. Sodium atoms in red; chlorine atoms in blue.	122
Figure 4.2 Calculated bulk Madelung constant for center sodium atom as a function of the number of atoms in a NaCl lattice seeded by the $\text{Na}_{14}\text{Cl}_{13}$ cube. Experimental value of 1.74756 is denoted in black	123

Figure 4.3 Illustration of Na_4Cl_4^0 seed structure. Sodium atoms in red; chlorine atoms in blue	124
Figure 4.4 Calculated bulk Madelung constant for center sodium atom as a function of the number of atoms in a NaCl lattice seeded by the Na_4Cl_4 cube. Experimental value of 1.74756 is denoted in black	125
Figure 4.5 Average charge, in electrons, by radial distance from center site of NaCl cube for (a) sodium atoms and (b) chlorine atoms. Charges labeled in blue refer to the ideal bulk crystal; the red points denote system with anionic vacancy.	126
Figure 4.6 Average Madelung energy of chlorine atoms by radial distance from the anionic vacancy in NaCl.	127
Figure 4.7 Average charges, in electrons, for chlorine atoms by radial distance from the f-center in NaCl as a function of fixed charge localized in the anionic vacancy.	128
Figure 4.8 Average Madelung energy of chlorine atoms by radial distance from the f-center in NaCl.	129
Figure 4.9 Top: Sum of Madelung energies and self-energies for all ions within 1.5 nm of the f-center. Self-energy is computed using the second-order Taylor expansion of energy with respect to on-site charge (Equation 4.2). The energy summations are reported as a function of fixed charge in the f-center. Bottom: Total energy (Madelung + self) as a function of f-center charge.	130

CHAPTER 1 – MOTIVATION

1.1 Classes of atomistic simulations

Atomistic simulations can be conveniently divided into two general classes: 1) quantum mechanical methods that account for electronic structure and 2) classical dynamics methods that replace the electronic structure with appropriate empirical potentials. Each class has its strengths and weaknesses, making the choice of simulation method entirely dependent upon the problem being studied. While the goal of all simulations is to achieve physical accuracy, no model is perfect, and performing theoretical calculations is therefore a task of managing compromises.

Quantum mechanical approaches often include first principles techniques which, as the name suggests, involve the most basic principles of quantum mechanics without introducing empirical parameters. These approaches attempt to solve the electronic energy levels of atoms to predict physical properties not easily observed, such as binding energies. But solving these energy levels is difficult; an exact solution for Schrödinger's equation only exists for hydrogen. As the problem expands to multiple atoms multiple interacting nuclei and electrons, approximations must be made to allow for more tractable calculations. The Born-Oppenheimer (BO) approximation^{1,2} uses the huge nucleus/electron mass ratio to treat the nuclei as stationary relative to the electrons. This allows the electronic wavefunctions to be solved without considering the nuclear degrees of freedom.

Within first principles methods, there are different approaches to solving the many-body quantum mechanical problems. The Hartree-Fock method³ approximates the true N -

body wavefunction using N single electron orbitals. The orbital wavefunctions form a Slater determinant⁴, or matrix of the wavefunctions whose products must satisfy certain physical conditions, namely anti-symmetry with respect to the interchange of electron positions.

While the Hartree-Fock method approaches the quantum mechanical problem through the lens of molecular orbits, an alternative approach is to model energy levels and bonding characteristics using electron density. The Hohenberg-Kohn^{5,6} theorems state that the physical properties of a many-body system are a functional of the ground-state electron density. This is the basis for density functional theory (DFT)^{5,6}. DFT calculations are one of the more widely used first principles techniques, and can be carried out by downloadable packages, such as the Vienna Ab Initio Simulation Package (VASP)⁷ and QuantumEspresso⁸.

Although often powerfully accurate, first principles calculations are extremely computationally demanding with processing power typically scaling with the cube of the system size. In other words, an eight-fold increase in processing resources only nets a two-fold increase in the number of atoms that can be simulated. Because of this, first principles methods are generally restricted to systems containing 10^2 - 10^3 atoms. The size and time scales of many materials science phenomena cannot be captured on such a restricted scale. These processes, including dislocation dynamics and plastic deformation, are better served by simulations using models with more simplistic approximations of electronic structures.

Classical empirical potentials attempt to model interatomic forces that arise from the quantum mechanical interactions using relatively simple functions of the positions of the atoms. Forces on each atom can be computed analytically using derivatives of the potential,

and accelerations and trajectories can then be determined by solving classical equations of motion. Empirical potentials allow for much larger simulation scales in terms of size and time, because the electronic degrees of freedom have been discarded.

Because explicit calculation of electronic states is omitted, construction of suitable empirical potentials is a balancing act between accuracy and transferability. The former entails reproducing physical properties that are consistent with experimental measurements. To accomplish this, empirical potentials are typically *fitted* to experimental parameters. However, a good empirical potential function must also exhibit transferability, or the ability to reproduce properties to which it was not fitted. Furthermore, these qualities must be achieved while preserving the computational efficiency that makes such potentials attractive. The pursuit of these objectives has led to great advances in the state of the art in empirical potentials; the challenges faced and the solutions that have been developed are detailed in the next section.

1.2 Evolution of empirical potentials

Beginning in the 1980s, many-body interatomic potentials begin to emerge which permitted a description of atomic interactions beyond a simple pair-additive relation. Pair potentials were qualitatively useful in chemistry and physics for describing local configurations⁹, but were deficient in applications studying deformation in materials. This is because energies associated with dislocation dynamics and plastic deformation in materials require large volumes of material to be accurately modeled. Additionally, by virtue of describing pairwise interactions only, pair potentials do not include contributions from the local environment.

This results in difficulty in modeling the diminishing energetic benefits of forming additional bonds because the weakening of bond strength due to over-crowding, a consequence of Pauli's principle, is not captured.

The first step towards a many-body representation of atomic bonding energy came in the form of effective medium approximation¹⁰. Starting from the result that the energy of hydrogen impurities was primarily dependent on the local environment, Norskov developed an expression for the energy of embedding a defect that treated the "host" material as a gas with density equivalent to the host material, illustrated schematically in Figure 1.1. This gave rise to new understanding of interatomic bonding that would later be utilized in many-body potential energy expressions such as the Finnis-Sinclair (F-S)¹¹, Embedded Atom Method (EAM)¹², and glue potentials¹³.

Although derived from different approaches, the F-S, EAM, and glue potentials have the appeal of containing elements of DFT. Recall the Hohenberg and Kohn statement that energy is a functional of electron density. This contribution to potential energy is apparent in the functional form shared by the F-S, EAM and glue potentials. Each is constructed similarly from two terms: a two-center pair potential, and a cohesive energy "density" term. The latter is rooted in the tight-binding description of bonding. When the valence orbitals of two atoms overlap, the band of potential energy states for the electrons broadens, as depicted in Figure 1.2. The bond energy of an atom can therefore be approximated by the width, or second moment, of the density of states. Empirically, the density of states is proportional to the number of nearest neighbors¹⁴. This simple, yet elegant, "second moment approximation" allows much of the essence of quantum mechanical bonding characteristics

of atoms to be modeled using only the Cartesian coordinates of its neighbors and thus being much less computationally expensive than explicitly solving electronic energy states.

The functional form of these potentials and that of the Tersoff potential¹⁵⁻¹⁷ are essentially the same¹⁸. Tersoff developed interatomic potentials for Si and other covalent materials using the energy expression of Abel¹⁹, which gives the binding energy as sum of near-neighbor pair interactions modified by the local atomic environment. The local environment term is a function of the local coordination; since nearest-neighbor density changes with the order of a covalent bond, this approximation is successful in describing single-, double- and triple-bond energies in hydrocarbons. However, this environment term encounters difficulties with intermediate bonding systems. Two examples are illustrated in Figure 1.3: graphite and $(\text{CH}_3)_2\text{C}=\text{C}(\text{CH}_3)_2$. The atoms in red have the same local coordination in each molecule, but the bond between them has much different characteristics in one molecule compared to the other. The bond in graphite, due to the conjugated double bonds, has 1/3 double-bond and 2/3 single-bond character; in contrast, the bond in $(\text{CH}_3)_2\text{C}=\text{C}(\text{CH}_3)_2$ is purely double-bond in character.

Brenner addressed this deficiency of the Tersoff formalism in developing the reactive empirical bond order (REBO) potential²⁰ through a correction factor to the local environment term that couples atomic coordination to bond energy. The coupling parameter for each bond is given by an average of terms associated with each atom in the bond, with additional terms for the number of carbon, hydrogen, and conjugated bonds that provide a more complete description of the local atomic environment. The REBO potential was able to correctly predict π -bonded reconstruction as the most stable for the (111) surface of diamond.

Pettifor subsequently developed an analytic bond order potential²¹ that circumvented the *ad hoc* correction terms used by the REBO. Although these corrections eliminated the spurious “averaging” of bond strengths, they added many parameters to the fitting process. Transferability of classical potentials generally suffers as the number of fitting parameters increases. Pettifor’s solution was to explicitly treat π -bonding by going beyond nearest neighbors and including higher moments of electronic bond energy. The second moment describes only the width of an energy distribution (or density of states); the third and fourth moments describe the skewness of the distribution and the tendency to form a gap in the middle of the distribution, respectively. From the standpoint of bond energy, this involves including the contributions of atoms beyond the first shell of nearest neighbors. The moments theorem states that the *n*th moment of the local density of states is determined by the sum of all paths around neighboring atoms that begin and end at the same atom. The fourth moment approximation includes all neighbors of an atom that can be hopped to and back in four atom-hops or less.

Pettifor would later expand his bond order potential to encompass up to six moments²² in an effort to model magnetism in transition metals. The Stoner model²³ describes magnetism using density of states concepts. When filling orbitals, it is energetically preferable for electrons to reside in the lowest possible energy level. An electron can change its spin in order to share a lower, already-occupied orbital; this is the result of a balance between achieving the lowest possible quantum number and the energy required to flip spins. In most materials, the energy reduction associated with entering a lower orbital dominates. However, some transition metals such as iron have *d* electron

valance bands that span a very narrow range of energies; the energy reduction from occupying a lower orbital does not offset the exchange energy penalty of changing spin. The result is electrons with aligned spin, giving these metals ferromagnetic properties.

The magnetic contribution to binding energy results in iron taking the bcc phase as its ground state, in contrast to the transition metals ruthenium and osmium, which assume an hcp structure. Therefore, constructing an interatomic potential that captures the quantum mechanical forces behind magnetism is essential for successfully modeling ferromagnetic elements. Pettifor's higher-moment approximation bond order potential effectively predicts the structural preferences of iron as well as the trend in crystal structures (hcp \rightarrow bcc \rightarrow hcp \rightarrow fcc) that is observed across the non-magnetic $4d$ and $5d$ transition metal series.

The success of classical potentials comes from the use of approximations that allow for energy expressions to reflect the underlying quantum mechanical principles of bonding. Indeed, as the potentials incorporate more components of the electronic structure, as is the case with higher moment approximation potentials, greater capabilities in predicting and reproducing physical properties follow. But the increasingly detailed electronic structure approximation comes at a cost of computational resource demands. For instance, although several orders of magnitude faster than standard tight-binding calculations, fourth-moment approximation potentials are still at least an order of magnitude slower than second-moment approximation based models²⁴. Further, while increases in the number of moments allows for the capture of more of the physics in electronic bonds, it does not aid in describing effects that are primarily driven by electronic degrees of freedom. In some cases these effects can be recovered using multiscale schemes designed to compensate for the lack of explicit

treatment of electrons. These approaches and their applications are discussed in the next section.

1.3 Multiscale approaches to atomistic simulations

Atomic simulations sufficiently large to model plastic deformation typically require replacing energies from explicit electronic states with some effective inter-atomic potential. The embedded-atom method (EAM) potentials, for example, have proven to reproduce many of the structural, energetic and vibrational frequencies of a wide range of metals, from which reasonable thermodynamic properties (such as melting temperature) can follow¹². At room temperature, however, the thermal transport properties of metals are dominated by electrons, and therefore thermal transport coefficients are not typically reproduced by analytic potentials. In addition, in a typical large-scale atomic simulation, vibrational modes and phonon states are populated classically, and therefore quantum heat capacities and phonon propagation are not properly treated, again regardless of the quality of the potential energy function.

Schall *et al.* demonstrated the significance of neglecting electronic degrees of freedom in treating thermal transport coefficients²⁵. Modeling the flow of heat from a constant temperature surface through the bulk using EAM potentials, Schall *et al.* calculated the implied thermal diffusivities for several metals by fitting a continuum heat flow equation to the simulation temperature profile. The thermal diffusivities from the EAM were far smaller than experiment, up to three orders of magnitude too small in the case of silver and

gold. The resulting temperature profile implies excessively localized heating; the net result will be a tendency to overstate thermally-induced deformation effects.

Several groups have sought to incorporate electronic heat transfer into molecular dynamics simulations using a two temperature model (TTM)²⁶⁻³². The TTM decouples electronic and lattice temperatures, and expresses the time evolution of temperatures using nonlinear different equations of continuum heat flow. Solutions to the heat flow equations are typically obtained by finite difference method. When combined with the MD simulation, the lattice temperatures of the TTM are replaced by those calculated from the MD potential, and the electronic temperatures are coupled to the lattice using an electron-phonon scattering mechanism. In an extensive set of studies²⁶⁻²⁸, Zhigilei and co-workers, for example, have used this concept to model laser interactions with metals. In laser super-heating of metals, where electron temperatures can instantaneously exceed several thousand K, electrons below the Fermi level can be excited and increase the electron-phonon coupling. This makes it difficult to specify a functional form of heat capacity, and heat capacity thus requires density of states calculations.

Rather than using the fine grain two-temperature model to improve thermal transport, one alternative is treat the heat flow dynamics at a scale separate from the atomistic dynamics. This is conceptually analogous to the multiscale nature of the quasicontinuum (QC) method³³. The QC method was developed in order to simulate mechanical properties at longer length scales than what was afforded by atomistic-only simulations, but still incorporate the influence of atomistic-level structures. This was accomplished by adapting the mesh size of a finite element simulation in environments where stress gradients are

particularly high (e.g. near a point defect); as the mesh size decreases to atomistic dimensions, force calculations are handed off to an interatomic potential. This methodology was later used to model nanoindentation into a solid with a subsurface grain boundary³⁴.

A potential issue with the QC method is that, while there are multiple size scales simulated, both scales are limited to the time step size of the atomistic simulation. Therefore, stringent limits will be imposed on the material processes that can be simulated. For example, simulating strain in a crystal will require extremely high strain rates that may not be physically relevant. A multiscale method was developed³⁵ to directly address this limitation by separating the atomistic and continuum simulations. A continuum simulation is run across the entirety of the material volume, while an atomistic simulation is carried out only in a localized region of interest, such as a dislocation. The atomistic forces are then projected to the continuum simulation, allowing for a bridging of the two size scales. And because the two simulations are independent, separate time steps can be used as appropriate for each scale.

The concept of incorporating electronic temperatures combined with a two-scale concurrent simulation approach treating both the atomistic and continuum scales forms the foundation of the methodology developed by Schall et al²⁵. This scheme uses a parallel continuum calculation of heat flow carried out on a grid that is a coarse grained representation of the atomic simulation. A major advantage of using a continuum simulation of heat flow compared to the TTM-MD method is the ability to use experimental thermal diffusivity (or, equivalently, thermal conductivity and heat capacity), providing a great degree of flexibility in simulating materials. Using an *ad hoc* feedback between the grid and

atom simulation, the thermal transport in the latter is effectively corrected. This methodology was first implemented in simulations of a spherical metallic tip sliding on a silver surface. Without the thermal transport correction from the continuum simulation, the sliding resistance for the tip was exaggerated due to non-physical localized heating that resulted in melting of the tip.

Describing electronic effects on a continuum scale using experimental input parameters opens up doors for other capabilities to be introduced into atomistic simulations. Building on this coarse graining approach, Padgett and Brenner³⁶ developed a method in which grid regions are connected by electrical resistors with resistances that are determined from the density and temperature profiles of the atomic simulation. Heat generated from current flow through these resistors is then coupled into the simulation via velocity scaling combined with a local thermostat. Together with the thermal transport corrections, this method is able to introduce Joule heating into a simulation. In addition, because a current flow through the system is known, other effects such as magnetic forces due to current constriction can in principle be included in a simulation.

Another phenomenon that plays an important role in the properties of some materials but which is neglected in most empirical potentials is the role of Coulombic forces arising from atomic charges. Most engineering metals form oxides quite readily, and the electrostatic interactions between the cations and anions is one of the dominant sources of energy in oxides. As another example, intermetallic compounds formed by the mixing of two species at an interface such as aluminum-copper result in charge transfer due to

electronegativity differences. Modeling the charge distribution therefore plays a critical role in the simulating metal/metal-oxide interfaces and intermetallic compounds.

An obvious starting point would be to assign fixed charges to atoms at the beginning of a simulation and incorporate the electrostatic energy into the potential function as a constant. However, atomic charges cannot be considered constant for an evolving system. On-site charges in a metallic system containing a surface oxide, for example, will range from near-zero in the bulk metal to nearly fully ionic in the oxide. Hence, accurately describing the Coulombic energy contributions requires the charge states to be continuously solved.

Rappe and Goddard³⁷ developed a method of predicting atomic charges using a method of Charge Equilibration (QEq). The QEq scheme starts from the basis of atoms minimizing chemical potential energy with respect to the addition of charge. The chemical potential for each atom is the derivative of energy with respect to charge, and is a function of empirical parameters derived from atomic data, and an appropriate Coulomb interaction term. This scheme was successfully used to calculate charges on atoms in a variety of organic, inorganic, biological, and polymer systems.

Several groups have incorporated QEq into empirical potentials. Streitz and Mintmire³⁸ combined the QEq methodology with the EAM to simulate aluminum systems containing oxides. The resulting potential accurately described the cohesive, structural, and elastic properties of both fcc aluminum and α -alumina, and the properties of alumina interfaces were in good agreement with first principles calculations. Given the functional similarity between EAM and bond order potentials, it follows that the QEq has also been

incorporated into the latter. The charge optimized many-body (COMB) potential³⁹ was developed to simulate Si/SiO₂ systems, and was found to effectively predict structures and parameters for silicon and five polymorphs of silica.

The QEq scheme is an approximation of the redistribution of charge, and is not appropriate for all systems. The model allows transferal of partial charges across long distances. For example, when the chemical bond of a HF molecule is broken, the atoms become neutral as the ionization potential of hydrogen exceeds the electronegativity of fluorine. This non-local charge transfer also results in inaccurate polarizability of alkane chains⁴⁰. This has led to the formulation of charge transfer mechanisms based on pairs of atoms rather than individual atoms. An example is the atom-atom charge transfer (AACT)⁴⁰ model that circumvents non-physical long-range charge transfer by constraining transfer of charge to atoms which are directly bonded. The AACT scheme effectively fixes some of the problems associated with the entire atomic system being treated as a single conductor. However, the AACT utilizes parameters that are fitted using small structures that are assumed to be representative of larger and more complex molecules. But this discards one of the more attractive features of the QEq formalism, and that is the use of parameters that are motivated by first principles calculations that likely enhance its transferability.

1.4 Context of current work

One of the key advantages to the multiscale FD/MD methodology used by the Brenner group is that it offers an extremely flexible platform for studying a wide variety of atomic systems. This provides the opportunity to continually expand its reach to investigate atomistic

processes where the ability to model Joule heating captures physics that would otherwise be inaccessible to an MD simulation. The current work applies the methodology to simulate asperity tips between contacts of various metals in the presence of electromagnetic stress. The multi-scale approach is especially suitable for “hot” metallic contacts, because some of the experimentally-observed deformation effects, such as adhesion and material transfer, are exacerbated with Joule heating. Building back in the thermal physics will allow the simulations to capture the atomistic detail that eludes typical continuum simulations while still preserving the continuum descriptions of heat flow and electrical current. These “tribological” wear simulations comprise Chapter 3 of the present work.

The other topic investigated and presented in Chapter 4 is the transferability of the QEq methodology. Although this scheme has proven to successfully mimic the equilibrium charges in ionic bonds of oxides, it is unclear whether it would be able to accurately mimic the redistribution of charge that occurs when an F-center anion vacancy is formed in bulk sodium chloride. The influence on electrostatic energy of a NaCl crystal is analyzed using the equilibrated charges and compared to first principles data.

1.5 References

1. Born M. Quantum mechanics in impact processes. *Z Phys.* 1926;38(11/12):803-840. doi: 10.1007/BF01397184.
2. Oppenheimer J. On the quantum theory of electronic impacts. *Phys Rev.* 1928;32(3):0361-0376. doi: 10.1103/PhysRev.32.361.
3. Fock V. Approximation method for the solution of the quantum mechanical multibody problems. *Z Phys.* 1930;61(1-2):126-148. doi: 10.1007/BF01340294.
4. SLATER J. A simplification of the hartree-fock method. *Physical Review.* 1951;81(3):385-390. doi: 10.1103/PhysRev.81.385.
5. HOHENBERG P, KOHN W. Inhomogeneous electron gas. *Phys Rev B.* 1964;136(3B):B864-&. doi: 10.1103/PhysRev.136.B864.
6. KOHN W, SHAM L. Self-consistent equations including exchange and correlation effects. *Physical Review.* 1965;140(4A):1133-&.
7. Vienna ab initio simulation package (VASP). <http://www.vasp.at/2012>.
8. Quantum espresso. <http://www.quantum-espresso.org/2012>.
9. MAEDA K, VITEK V, SUTTON A. Inter-atomic potentials for atomistic studies of defects in binary-alloys. *Acta Metallurgica.* 1982;30(11):2001-2010. doi: 10.1016/0001-6160(82)90104-3.

10. NORSKOV J, LANG N. Effective-medium theory of chemical-binding - application to chemisorption. *Phys Rev B*. 1980;21(6):2131-2136. doi: 10.1103/PhysRevB.21.2131.
11. FINNIS M, SINCLAIR J. A simple empirical N-body potential for transition-metals. *Philos Mag A-Phys Condens Matter Struct Defect Mech Prop*. 1984;50(1):45-55.
12. Daw MS, Baskes MI. Embedded-atom method - derivation and application to impurities, surfaces, and other defects in metals. *Physical Review B*. 1984;29(12):6443-6453.
13. ERCOLESSI F, TOSATTI E, PARRINELLO M. Au (100) surface reconstruction. *Phys Rev Lett*. 1986;57(6):719-722. doi: 10.1103/PhysRevLett.57.719.
14. Sutton AP, Balluffi RW. *Interfaces in crystalline materials*. Oxford: Clarendon Press; 1995:150-239.
15. TERSOFF J. New empirical-approach for the structure and energy of covalent systems. *Phys Rev B*. 1988;37(12):6991-7000. doi: 10.1103/PhysRevB.37.6991.
16. TERSOFF J. Empirical interatomic potential for carbon, with applications to amorphous-carbon. *Phys Rev Lett*. 1988;61(25):2879-2882. doi: 10.1103/PhysRevLett.61.2879.
17. TERSOFF J. Modeling solid-state chemistry - interatomic potentials for multicomponent systems. *Phys Rev B*. 1989;39(8):5566-5568. doi: 10.1103/PhysRevB.39.5566.
18. BRENNER D. Relationship between the embedded-atom method and tersoff potentials. *Phys Rev Lett*. 1989;63(9):1022-1022. doi: 10.1103/PhysRevLett.63.1022.

19. ABELL G. Empirical chemical pseudopotential theory of molecular and metallic bonding. *Phys Rev B*. 1985;31(10):6184-6196. doi: 10.1103/PhysRevB.31.6184.
20. BRENNER D. Empirical potential for hydrocarbons for use in simulating the chemical vapor-deposition of diamond films. *Phys Rev B*. 1990;42(15):9458-9471. doi: 10.1103/PhysRevB.42.9458.
21. Pettifor D, Oleinik I. Analytic bond-order potentials beyond tersoff-brenner. I. theory. *Phys Rev B*. 1999;59(13):8487-8499. doi: 10.1103/PhysRevB.59.8487.
22. Drautz R, Pettifor DG. Valence-dependent analytic bond-order potential for transition metals. *Phys Rev B*. 2006;74(17):174117. doi: 10.1103/PhysRevB.74.174117.
23. Stoner E. Collective electron ferromagnetism. *Proc R Soc Lond A-Math Phys Sci*. 1938;165(A922):0372-0414. doi: 10.1098/rspa.1938.0066.
24. Los JH, Bichara C, Pellenq RJM. Tight binding within the fourth moment approximation: Efficient implementation and application to liquid ni droplet diffusion on graphene. *Phys Rev B*. 2011;84(8):085455. doi: 10.1103/PhysRevB.84.085455.
25. Schall JD, Padgett CW, Brenner DW. Ad hoc continuum-atomistic thermostat for modeling heat flow in molecular dynamics simulations. *Molecular Simulation*. 2005;31(4):283-288.

26. Ivanov D, Zhigilei L. Combined atomistic-continuum modeling of short-pulse laser melting and disintegration of metal films. *Phys Rev B*. 2003;68(6):064114. doi: 10.1103/PhysRevB.68.064114.
27. Lin Z, Zhigilei LV, Celli V. Electron-phonon coupling and electron heat capacity of metals under conditions of strong electron-phonon nonequilibrium. *Physical Review B*. 2008;77(7):-.
28. Zhigilei LV, Lin ZB, Ivanov DS. Atomistic modeling of short pulse laser ablation of metals: Connections between melting, spallation, and phase explosion. *Journal of Physical Chemistry C*. 2009;113(27):11892-11906.
29. Gao F, Bacon DJ, Flewitt PEJ, Lewis TA. The effects of electron-phonon coupling on defect production by displacement cascades in alpha-iron. *Model Simul Mater Sci Eng*. 1998;6(5):543-556.
30. Phillips CL, Crozier PS. An energy-conserving two-temperature model of radiation damage in single-component and binary lennard-jones crystals. *J Chem Phys*. 2009;131(7):11.
31. Kaganov MI, Lifshitz IM, Tanatarov LV. RELAXATION BETWEEN ELECTRONS AND THE CRYSTALLINE LATTICE. *Soviet Physics JETP-USSR*. 1957;4(2):173-178.

32. Anisimov SI, Kapeliov.BI, Perelman TL. Electron-emission from surface of metals induced by ultrashort laser pulses. *Zhurnal Eksperimentalnoi I Teoreticheskoi Fiziki*. 1974;66(2):776-781.
33. Tadmor EB, Ortiz M, Phillips R. Quasicontinuum analysis of defects in solids. *Philosophical Magazine a-Physics of Condensed Matter Structure Defects and Mechanical Properties*. 1996;73(6):1529-1563.
34. Shenoy VB, Miller R, Tadmor EB, Rodney D, Phillips R, Ortiz M. An adaptive finite element approach to atomic-scale mechanics - the quasicontinuum method. *J Mech Phys Solids*. 1999;47(3):611-642.
35. Wagner GJ, Liu WK. Coupling of atomistic and continuum simulations using a bridging scale decomposition. *Journal of Computational Physics*. 2003;190(1):249-274.
36. Padgett CW, Brenner DW. A continuum-atomistic method for incorporating joule heating into classical molecular dynamics simulations. *Molecular Simulation*. 2005;31(11):749-757.
37. Rappe AK, Goddard WA. Charge equilibration for molecular-dynamics simulations. *J Phys Chem*. 1991;95(8):3358-3363.
38. Streit FH, Mintmire JW. Electrostatic potentials for metal-oxide surfaces and interfaces. *Physical Review B*. 1994;50(16):11996-12003.

39. Yu J, Sinnott SB, Phillpot SR. Charge optimized many-body potential for the si/SiO₂ system. *Phys Rev B*. 2007;75(8):085311. doi: 10.1103/PhysRevB.75.085311.
40. Chelli R, Procacci P, Righini R, Califano S. Electrical response in chemical potential equalization schemes. *J Chem Phys*. 1999;111(18):8569-8575.

1.6 Tables and Figures

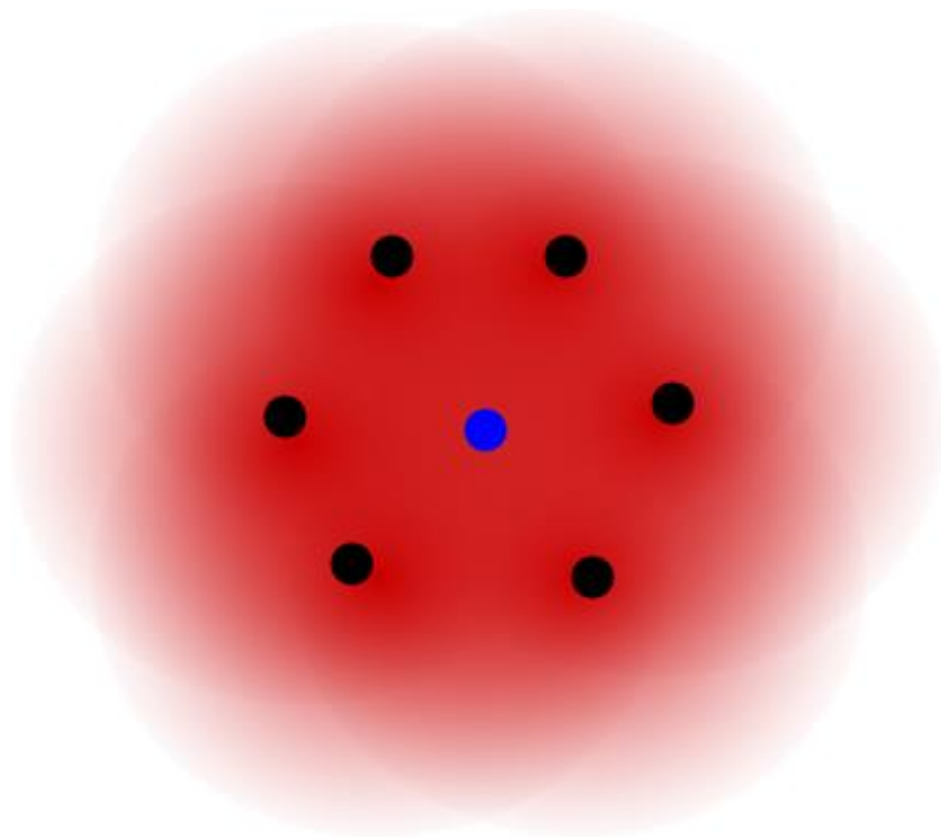


Figure 1.1 Schematic illustration of host atoms' (black dots) electron density (red cloud) contributing to the binding energy of an "embedded" atom (blue dot).

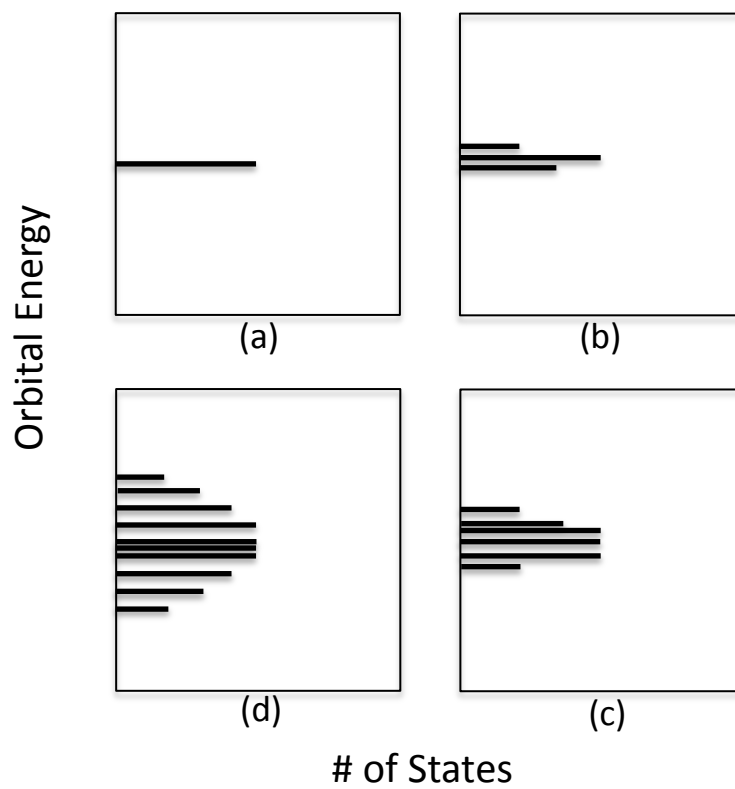


Figure 1.2 Schematic illustration of the broadening of density of states as the orbitals of two atoms transition from far apart (a) to overlapped (d).

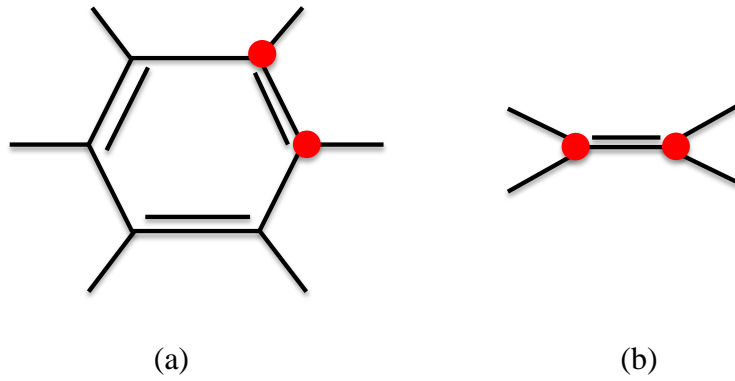


Figure 1.3 Illustration depicting the different bonding characteristics of atoms (red) with the same coordination (three) but different bond character in two different molecules: (a) graphite; (b) $(\text{CH}_3)_2\text{C}=\text{C}(\text{CH}_3)_2$

CHAPTER 2 – THEORY AND MODELING METHODS

In this chapter, the underlying principles of the methodologies utilized in Chapters 3 and 4 are reviewed in detail. The purpose of this chapter is to proceed through the background of each modeling technique to provide a theoretical justification for their present implementation. The computational details, parameters, and obstacles of typical simulations are outlined for each application.

2.1 Embedded Atom Method

Early classical dynamics simulations often used two-body pair potentials which express the energy for a collection of bodies as pair-wise additive. Different functional forms of this interaction have been specified. For example, the Lennard-Jones¹ potential gives the two-body energy as

$$V(r) = 4\varepsilon \left[\left(\frac{\sigma}{r}\right)^{12} - \left(\frac{\sigma}{r}\right)^6 \right] \quad (2.1)$$

where r is the distance between the atoms, ε is the equilibrium energy minimum for the pair, and σ is the distance at which $V(r)$ is equal to zero. The first term in the bracket describes the energy contribution from Pauli repulsion which occurs at short ranges due to overlapping electron orbitals; the second term in the brackets represents the long-range, cross-atomic attractive contribution. The Morse potential² similarly expresses pair interaction using competing repulsive and attractive components,

$$V(r) = \varepsilon [e^{2\beta(\rho-r)} - 2e^{\beta(\rho-r)}] \quad (2.2)$$

where ρ and ε are equilibrium bond length and dislocation energy, respectively, and β is an inverse length scaling factor that endows the Morse potential with more intermediate range of interaction. The exponential-6 potential³ modifies the Lennard-Jones potential by substituting a repulsive term with exponential form

$$V(r) = Ae^{-\beta r} - \frac{C}{r^6} \quad (2.3)$$

where A , B , and C are constants. The exponential term more appropriately captures the decay of intermolecular repulsions.

Pair potentials of these forms have severe limitations in predicting properties of crystalline solids stemming from the inability to capture the influence of local atomic environment on bonding. Intuitively, the energetic favorability of atomic bonding should diminish with increasing atomic density, and this is ignored in typical pair potentials. Pair potentials also do not account for directionality in bonding, as the interaction terms are dependent only on the distance between two atoms. Consequently, covalent bonding is not properly captured by pair potentials. These two limitations can result in highly inaccurate cohesive energies and elastic constants in metals.

One solution proposed⁴ to capture atomic environment contributions was to augment a pair potential expression with a volume term, such that

$$E_b = (1/2\Omega_0) \sum_m \phi(r^m) \quad (2.4)$$

where Ω_0 is the undeformed atomic volume and ϕ is the potential energy function for two atoms separated by the vector r^m . The volume-dependent energy term imparts some local environment effects, but is an unsatisfactory method for doing so because it requires a

definitive quantity for the volume to be known. This poses potential problems for systems with ambiguities in the total volume, as is the case for surface relaxations, point defects, and fracture surfaces.

The EAM⁵ is an expression for energy that combines a pair interaction term with an embedding term that more explicitly treats the local environment dependence of atomic energy. This approach essentially treats all atoms as impurities, and a contribution to energy is obtained from each impurity disturbing the electron density of the local environment. The functional form for the energy of atom i due to j neighbors is

$$E = \sum_i F(\rho_i) + \frac{1}{2} \sum_{i \neq j} V_{ij}(R_{ij}) \quad (2.5)$$

where F is the embedding energy of atom i , ρ_i is the electron density at site i , and V_{ij} is the pair interaction for neighbor j at a distance R_{ij} . This has the appealing characteristic of being philosophically rooted in density functional theory (DFT) principles, since the energy is being described as a functional of the atomic-like electron density⁶.

The embedding energy function and pair potential are determined empirically from physical properties of the solid. Foiles et al⁷ derive these for several fcc metals, including Au, Cu and Ni, using the lattice constant, elastic constants, vacancy-formation energy, and sublimation energy in fcc and bcc phases. The embedding energy can be uniquely specified by fitting the energy from Eq. 2.5 to Rose's equation of state⁸

$$E(a) = -E_{sub}(1 + a^*)e^{-a^*} \quad (2.6)$$

where E_{sub} is the absolute value of the sublimation energy at zero temperature and pressure, and a^* is the deviation from equilibrium lattice constant given by

$$a^* = \left(\frac{a}{a_0} - 1\right) / \left(\frac{E_{sub}}{9B\Omega}\right)^{1/2} \quad (2.7)$$

where B is the bulk modulus, Ω is the equilibrium volume per atom, and a and a_0 are the fcc lattice constant and equilibrium lattice constant, respectively. Then, all one needs to specify for the embedding function is the electron density, which is obtained from atomic densities computed from the Hartree-Fock wave functions by

$$\rho^a(R) = n_s \rho_s(R) + n_d \rho_d(R) \quad (2.8)$$

where n_s and n_d are the number of s and d electrons (the bonding electrons for transition metals), respectively, and ρ_s and ρ_d are the densities associated with the s and d wave functions. The sum $n_s + n_d$ is fixed for a given metal, and n_s is varied for the fitting procedure. The pair potential is expressed as

$$Z(R) = Z_0(1 + \beta R^v)e^{-\alpha R} \quad (2.9)$$

where Z_0 is the number of outer electrons, and α , β , and v are fitting parameters. The parameters are determined primarily by the shear moduli and vacancy-formation energy; the ones used for the Au EAM potential are given in Table 2.1.

In addition to the Au potential, the present work also models aluminum-copper systems using the Al-Cu potential developed by Liu et al⁹. This potential combines separate EAM potentials for Al¹⁰ and Cu¹¹, and derives a Al-Cu pair interaction term by fitting to the dilute heats of solution of each species in the other, as well as the heats of formation of the Al₂Cu and AlCu₃ phases. The data for the fitting procedures are sourced from DFT calculations.

Since its introduction, the EAM has been an important tool in atomistic simulations of nanoscale metallic properties. For example, Landman *et al* used the EAM to simulate the deformation of asperity tips to obtain a better understanding of how macroscopic scale contact mechanics apply to interfaces when the size scale is sufficiently small¹². The indentation and pull-off of Au and Ni pyramidal asperity tips was modeled using tips with an effective radius of about 30 angstroms. A “jump to contact” phenomenon during indentation was noted in which adhesion occurs by displacement of tip atoms, with a deformation method and pressure distribution similar to those predicted by contact mechanics theories. Pull-off of the asperity tips resulted in a “neck” that maintained crystalline structure, and the normal force through the neck was relatively constant during deformation, which is consistent with what would be predicted at the continuum level.

Kelchner *et al.*¹³ explored the capability of the EAM to resolve atomistic details of nanoindentation processes by treating the asperity tip as a purely repulsive element. This prevents the adhesive forces between tip and substrate that produce a “jump to contact” phenomenon, an effect that is not necessarily realistic because real indenters have unclean surfaces and hence much lower adhesion energies than clean metallic surfaces. The simulations by Kelchner showed that the nanoindentation force initially follows the continuum Hertzian solution for elastic deformation as $F = Kd^{3/2}$, where K is a fitted elastic constant and d is displacement. Beyond this elastic region, the force-displacement curves experience abrupt notches that the simulations reveal to be associated with the emanation of dislocation loops beneath the surface in the substrate opposite the indenter. An illustration of these sub-surface dislocation structures is presented in Figure 2.1.

2.2 Molecular Dynamics Simulations

Atomistic simulations with interatomic potentials use integration of classical equations of motion to determine the accelerations, velocities, and positions of atoms from the potential energy. At each time step in the simulation, the forces on the atoms are evaluated, and the system is evolved one timestep using a numerical integration scheme; for the current work, the numerical integration is completed using a Gear predictor-corrector algorithm. This algorithm uses up to fourth order time-derivatives of the current atomic positions to predict the positions of atoms at the next time step. The atoms temporarily “step” to these predicted positions, and forces computed from the potential at these positions are compared to the forces from the prediction stage. The differences between the new forces and the predicted forces are then used to correct the trajectory, and the positions at the next time step are then determined.

An alternative to the predictor-corrector algorithm is to integrate the equations of motion using the velocity Verlet algorithm. The velocity Verlet uses velocities and accelerations from the current time step to calculate velocities half way through the next time step. The half-step velocities are used to predict positions at the end of the time step. Forces on atoms at the next time step’s positions are calculated from the potential, and the velocities are then updated from the mid-time step values using the new forces. However, the velocity Verlet algorithm allows more energy fluctuation than the predictor-corrector since it includes lower order time-derivatives of position¹⁴.

The time step used for the integrator is one femtosecond. The selection of time step size for the integrator is system dependent, as it is required to be at least ten times shorter than the duration of the fastest motion in the system. Vibrations in molecules can have periods as short as $\sim 10^{-14}$ s. This sets the upper bound for the time step size in a typical molecular dynamics (MD) simulation to $\sim 10^{-15}$ s. The MD simulations reported here are typically run for a duration of ~ 100 picoseconds, or 100,000 time steps.

Basic MD simulations run in NVE, where the number, volume, and total energy are constant throughout the simulation. Consequently, the atoms experience fluctuations in temperature defined by average kinetic energy. However, it is often desirable to maintain a specified temperature in the system based on prescribed conditions or, as we will see later, feedback from external degrees of freedom. The simplest method of fixing atomistic temperatures is by re-scaling the velocities¹⁵ to “correct” the current temperature to the desired temperature. Although appealing from the standpoint of coding difficulty, velocity scaling potentially introduces non-physical effects, including localized, correlated motion. In addition, since the temperature is fixed over time, it does not produce fluctuations in temperature as required by statistical mechanics.

Alternatively, MD thermostats can be based on forces of constraint in the equations of motion. The Hoover thermostat¹⁶ is based on Gauss’ Principle of Least Constraint which essentially states that classical trajectories, such as those followed by atoms in an MD simulation, will minimize deviations from unconstrained trajectories. In other words, a system will tend to minimize the constraints applied through external forces. The thermostat is implemented through a frictional force term that is derived from a least-squares

minimization of differences between free and constrained accelerations. The term is incorporated into the equations of motion as follows:

$$a = \frac{F}{m} - \zeta v, \quad (2.10)$$

$$\zeta = \frac{\sum Fv}{\sum mv^2} \quad (2.11)$$

where F , v , and m , are the force, velocity, and mass, respectively. The frictional term, ζ , can be negative or positive for atoms depending on what is required to maintain constant temperature. The summation is typically over all atoms, but as will be shown later, the thermostat can be used in local regions of an MD simulation.

2.3 Continuum Principles of Current Flow at Metal-Metal Contacts

The physics for electrical contacts has been studied extensively¹⁷. The roughness of contacts creates groups of separate contact spots, known as a-spots. When an electrical current is present, the current flow lines distort to enter a contact spot. This creates a resistance, because the flow line constriction dictates that only a finite amount of electrical current may pass through a given contact spot. This is known as the constriction resistance, and for a circular contact with radius a much larger than the electron scattering length, it can be calculated as

$$R_c = \rho/2a \quad (2.12)$$

where ρ is the material resistivity.

An important phenomenon with electrical contacts is the relationship between potential and temperature¹⁷. The heat flow lines in a conductor follow the same path as the

current flow lines. An increase in the Joule heating due to a higher current density through an asperity is accompanied by a commensurate increase in heat flow due to a larger thermal gradient. Hence, the temperature increase is a function of the *voltage* applied, giving rise to the voltage-temperature relationship. Assuming the thermal conductivity and electrical resistivity, λ and ρ , respectively, are linearly dependent on temperature, the expression for temperature increase in a conductor with potential V applied is

$$V^2 = 8\lambda_0\rho_0\{(T_m - T_1) + (\alpha - \beta)(T_m^2 - T_1^2)/2 - \alpha\beta(T_m^3 - T_1^3)/3\} \quad (2.13)$$

where β and α are, respectively, the temperature coefficients of thermal conductivity and electrical resistivity. The quantity T_1 represents the bulk temperature of the conductor, and T_m is the maximum superheated temperature at steady state for the given voltage.

A simplified version of this V-T relation may be attained by exploiting the Wiedemann-Franz Law. This law expresses the temperature variations of thermal conductivity and electrical resistivity as

$$\lambda\rho = LT \quad (2.14)$$

where L is the Lorentz constant $2.45 \times 10^{-8} \text{ V}^2 \text{ K}^{-2}$. This law applies well to many conducting materials, and allows Equation 2.13 to be reduced to

$$V^2 = 4L(T_m^2 - T_1^2) \quad (2.15)$$

This relationship underscores an important corollary of the overlap of heat flow lines and electrical current lines. Reduction in the size of an electrical contact produces a higher current density for a given voltage, but does not increase the equilibrium temperature at the contact because the heat flow lines also become denser and consequently produce steeper

thermal gradients. The by-product of this is that the voltage required to melt (or boil) an electrical contact is an intrinsic material property without regard to the contact scale at equilibrium. Gold, for instance, melts at 1,337 K, which equates to an electrical potential drop of 0.43 V.

Although the maximum steady-state temperature in a conductor is fixed given the applied voltage, the time needed to reach this temperature is not, and is highly dependent on the voltage itself. The reduced time ($\mu\text{s}/\mu\text{m}^2$) for reaching steady state can be expressed as¹⁷

$$t = \frac{1}{V} \left[\frac{1}{\alpha} \ln \left[1 - \frac{T_m - T_0}{T_{eq} - T_0} \right] \right]^2 \quad (2.16)$$

where V is the applied voltage, T_{eq} is the equilibrium temperature from Equation 2.13, T_0 is the bulk temperature of the conductor, and α is a constant equal to $41.7852 \mu\text{m}/[\text{V } \mu\text{s}]^{0.5}$. The time needed to reach the steady-state temperature is thus inversely proportional to the applied voltage, and proportional to the contact area.

2.4 Continuum-Atomistic Thermostat

MD simulations are a powerful way to simulate large atomic systems consisting of 10^6 or more atoms. MD simulations use analytic potentials that replace the electronic degrees of freedom with analytic forces to reduce the computational burden. However, heat conduction in metals at room temperature occurs primarily via electrons. Discarding the electronic states results in the thermal transport coefficients that are underestimated by several orders of magnitude when using the embedded atom method (EAM) potentials¹⁸

There have been many other approaches in the past to build back in electronic effects that are not well described by empirical potentials. Zhigilei and others¹⁹⁻²¹ have combined the two-temperature model (TTM) with MD simulations in study laser heating of materials. This is a challenging application to model, because there are disparate sets of physics involved. For instance, the laser interaction in metals produces extremely rapid heating that exceeds the pace at which thermal energy can be transferred from electrons to phonons, requiring a description of electronic temperatures. On the other hand, the thermal energy deposition potentially induces microstructural changes, such as phase transformations, that are well-suited to atomistic simulation. The hybrid TTM-MD model by Zhigilei de-couples the lattice and electronic temperatures, allowing the former to be modeled by the MD simulation and the latter by the TTM. An electron-phonon scattering mechanism allows coupling between the electron temperatures and the lattice.

Wagner developed a continuum-atomistic technique^{22,23} motivated by the desire to extend the thermal boundaries of a system beyond what is computationally feasible for an all-atomistic system. This scheme allows thermal energy to be passed back and forth between a small atomistic system and a surrounding continuum body, as illustrated schematically in Figure 2.2. Heat flow in the continuum region is governed by Fourier's heat law, and uses experimental density, heat capacity and thermal conductivity, and is conveyed to the atomistic region by augmenting the interatomic potential energy used for the molecular dynamics simulation.

The continuum-atomistic method developed by the Brenner group^{18,24-26} takes a different approach to the multi-scale problem. This scheme utilizes *ad hoc* feedback from a

continuum simulation to project continuum heat transfer properties onto a concurrent atomistic simulation. In this *ad hoc* technique, a network of static, cubic grids is superimposed over the atomistic system. The grids contain continuously updated temperature, density and composition profiles determined by the atomistic simulation. The temperature of each grid section, for example, is equated to the average kinetic energy (minus the center of mass velocities) of the atoms in that grid section. Using this temperature distribution, new temperatures for the grid regions are then calculated by numerically solving the continuum heat flow equation of the form

$$\frac{\partial T}{\partial t} = D \frac{\partial^2 T}{\partial R^2} \quad (2.17)$$

where T is the temperature derived from the MD simulation, and D is the experimental thermal diffusivity.

In the original implementation of this methodology¹⁸, Equation 2.17 was evaluated explicitly via Euler's method, using a forward difference time derivative with a step size on the order of the MD simulation time step (~ 1 femtosecond). To preserve stability in the time derivative, the time step size is bounded by a maximum governed by the size of the finite difference grids and the value for D as

$$\Delta t^{max} = \frac{1}{2D \left(\frac{1}{\Delta x^2 + \Delta y^2 + \Delta z^2} \right)} \quad (2.18)$$

For gold at 300 K, the experimental thermal diffusivity is $1.283 \times 10^{-16} \text{ \AA}^2/\text{s}$. For a gold system with cubic grids with dimensions of 10 \AA , this leads to a maximum stable time step for the continuum simulation of approximately 1.2 femtoseconds.

A more recent version of the methodology uses thermal resistors for heat flow to circumvent the time step limitations induced by numerical instability. The use of thermal resistor-capacitor (RC) circuits is a common way of solving continuum heat transfer²⁷. Resistance, the product of voltage drop and current in electrical terms, can be analogously defined in thermal terms by replacing voltage drop with temperature differential, ΔT , and current flow with heat flow, q . Thermal resistance for the grid boxes is thus defined as

$$R = L/(\kappa \times A) \quad (2.19)$$

where L is the length of the box whose thermal resistance is defined, κ is the thermal conductivity, and A is the area of the box. Thermal capacitance of the grid is given by $c_p \times \rho \times V$, where c_p is the heat capacity of the material, ρ is the density, and V is the grid volume. Using these definitions, heat flow within the thermal circuit can be solved using Kirchoff's laws. Once the continuum temperatures in each grid are determined, they are communicated to the atoms by rescaling the atomic velocities. The integration of the atomic equations of motion is stepped forward in time one step while applying a Hoover thermostat locally to each grid region. The grid profiles are then recalculated and this feedback process between the atomic and continuum simulations is repeated as the simulation progresses.

A Hoover thermostat applied locally to each individual grid region in the atomic simulation was found to be necessary to create atomistic thermal profiles that match expected continuum results using experimental heat capacities and thermal conductivities¹⁸. The reason is that, while the temperature scaling alters the kinetic energy of each atom, part of this kinetic energy converts into potential energy of the system as required by the equipartition principle. The Hoover thermostat maintains an exact kinetic energy, thus

allowing heat to flow into the potential energy modes while maintaining an appropriate thermal profile. While perhaps unsatisfactory from a formal viewpoint, this is a pragmatic approximation for the simulations.

In addition to the thermal resistors connecting the continuum grid boxes, an electrical resistor network is implemented to model electrical potential drop and current flow. This differentiates the current methodology from the previous multi-scale techniques that primarily dealt with heat flow properties, and builds in the capability to model Joule heating through a continuously evolving atomistic system. As with the thermal properties, the electrical resistance of each grid region is calculated using information from the atomistic simulation. Based on the density profile of the grid, a resistivity is computed using the temperature-dependent experimental bulk resistivity for the material. For regions containing more than one species of atom, averaged bulk properties are used, while for regions that are devoid of atoms, the resistance of air is used. The virtual electrical resistors that connect neighboring grid regions then are assigned a resistance taken as the average resistance of the grid regions that they connect. An illustrative example of resistor grid construction is illustrated in Figure 2.3²⁴.

The potential drop and current flow through these resistors is calculated from a user-specified external applied voltage using Kirchoff's law assuming Ohmic behavior, and the velocities of the atoms in each grid region are appropriately scaled according to the Joule heating from the current flow. Like the virtual heat flow resistors, the virtual current flow resistor network is re-established as the atoms move so that the Joule heating and temperature profile tracks the evolution of the system. To maintain a constant current, the current is

calculated first for a given voltage without coupling to the atoms. The voltage is then adjusted and the current is recalculated. This procedure is continued until the desired current is attained within some pre-specified error. The coupling with the atomic dynamics is then resumed as detailed above. The experimental thermal and electrical transport values in the continuum simulations are taken from Slade²⁸.

A key advantage to the methodology utilized in this work is the flexibility it affords in system configurations. When the atomic and continuum simulations are carried out concurrently, the same step size is used to solve the atomic equations of motion as is used to numerically solve the current and heat transport equations via the resistor networks. However, a larger time step size can also be used with the virtual resistor system. This becomes particularly important in the case of Joule heating at a small contact, where the steady state thermal conditions are preceded by a transient period of heat flow. The rate at which the thermal transients give way to steady state conditions is determined by the thermal time constant, which is directly proportional to the heat capacity of the material and the thermal resistance. As Equation 2.19 implies, a narrow dimension (i.e. a small electrical contact) produces a large thermal resistance, which in turn lengthens the period of time before steady state thermal conditions. This necessitates a continuum-only “run-in” period of ~10-100 nanoseconds to determine the steady state thermal conditions. These conditions are then coupled to the atoms for the beginning of the atomistic simulation.

Similarly, the finite difference grid can extend well beyond an atomistic region, and by using larger grid sizes outside of the atomic region non-equilibrium heat flow determined from macroscopic-scale boundary conditions can be directly coupled to the atomic

simulation. Flow lines for electrical current and heat contort to enter a constriction point such as an asperity contact. Upon exiting the constriction, the flow lines spread out to ultimately re-attain geometry perpendicular to the contact. Figure 2.4 illustrates this for the simulations of Joule heating through aluminum-copper asperity contacts carried out by Irving²⁵. The darkened portions near the contact comprise the volume treated by the atomistic simulation and amount to approximately 15 nm in the contact direction. The lighter regions represent continuum volumes for the respective materials and have thicknesses five times greater than the contact substrates. As one can see from the flow lines represented by the black lines, the influence of the constriction on the spread of the flow lines extends well beyond the atomistic region. Therefore, applying the same boundary for both the continuum and atomistic simulations would introduce unphysical effects into the continuum solutions. In the case of a fixed temperature boundary, as utilized by Irving, the effect would be one of an artificially high thermal gradient. Therefore, the finite difference grid for the continuum simulation is typically displaced far from the atomistic region.

2.5 Charge Equilibration

Atomic charges in MD simulations are typically fixed. For systems with interfaces or phases with ionic bonding characteristics, this potentially introduces unrealistic treatment of the bond energies. The charge equilibration (QEq) approach taken by Rappe and Goddard²⁹ computes the optimum charge distribution of a system by minimizing the total energy with respect to on-site charges. The QEq scheme serves as the basis for the treatment of charge in simulations using the EAM³⁰ and bond order³¹ potentials.

The on-site energy of an atom with respect to charge can be expanded as a Taylor series as follows³²:

$$E_i(q_i) = E_{i0} + q_i \left(\frac{\partial E}{\partial q} \right)_{i0} + \frac{1}{2} q_i^2 \left(\frac{\partial^2 E}{\partial q^2} \right)_{i0} \quad (2.20)$$

When $q_i=-1$, the energy is equivalent to the electron affinity; when $q_i=+1$, the energy is the ionization potential. Using these solutions, the first and second-order derivatives become

$$\left(\frac{\partial E}{\partial q} \right)_{i0} = \frac{1}{2} (IP + EA) = \chi_i^0 \quad (2.21)$$

$$\left(\frac{\partial^2 E}{\partial q^2} \right)_{i0} = IP - EA \quad (2.22)$$

The first derivative term is the electronegativity; the second derivative is known as a hardness, or self-Coulomb³³, and represents repulsion between two electrons in a valence orbital. The local atomic energy can thus be expressed as^{29,30}

$$E_i(q_i) = \chi_i^0 q_i + \frac{1}{2} J_i^0 q_i^2 \quad (2.23)$$

where χ_i^0 is the electronegativity of atom i and J_i^0 is the self-Coulomb. The total electrostatic energy can then be described as

$$E_{es} = \sum_i E(q_i) + \frac{1}{2} \sum_{i \neq j} J_{ij} q_i q_j \quad (2.24)$$

with J_{ij} the Coulomb interaction between centers i and j resulting from overlapping charge distributions.

The optimum charge distribution corresponds to the equilibrium at which the atomic chemical potentials, or change in each atom's energy with respect to its charge, are equalized:

$$\chi_A(q_1 \dots q_N) = \chi_A^0 + J_{AA}^0 q_A + \sum_{B \neq A} J_{AB} q_B \quad (2.25)$$

$$\chi_A = \chi_B = \chi_C \dots = \chi_N$$

where χ_A is the chemical potential of atom A. Under the constraint that the N atom charges must sum to the total system charge,

$$Q_{total} = \sum_{i=1}^N Q_i \quad (2.26)$$

one is left with N simultaneous equations of the form $CQ = D$ where Q is a vector of all the charges, the components of C are

$$C_{1j} = 1 \quad (2.27)$$

$$C_{ij} = J_{1j} - J_{ij} \quad \text{for } I \geq 2 \quad (2.28)$$

and the components of D are

$$D_1 = Q_{total} \quad (2.29)$$

$$D_{ij} = \chi_i^0 - \chi_1^0 \quad \text{for } I \geq 2 \quad (2.30)$$

Rappe and Goddard proposed a method for constraining the charge solutions within a prescribed range. For instance, the charge on a lithium atom is required to be greater than -7, but less than +1. To enforce this constraint, the charge solutions obtained from Equations 2.27 – 2.30 are compared to the permitted range. A charge falling outside the range is set to the boundary limit. The equations are then re-solved for $N - p$ atoms, where p is the number of atoms for which charge has been fixed. The components of D from Equations 2.29 and 2.30 then become

$$D_1 = Q_{total} - \sum_{j=1}^p Q_j \quad (2.31)$$

$$D_i = \chi_i^{0F} - \chi_1^{0F} \quad \text{for } I \geq 2 \quad (2.32)$$

where

$$\chi_i^{0F} = \chi_i^0 - \sum_{j=1}^p J_{ij} Q_j \quad \text{for } I \geq 2 \quad (2.33)$$

and the charges on the non-fixed atoms are then solved. While charges for the NaCl crystals in the present work do not move outside of reasonable boundaries, this reduced equation methodology later will be shown to be important for modeling the extra electron of an f-center.

The values for χ_i^0 and J_i^0 are derived from atomic data²⁹; the two-center Coulomb interaction, J_{ij} , on the other hand, requires an assumption about the atomic charge densities. Assuming point charge interaction proportional to $1/R$ (Coulomb's law) is valid for atoms at large separation but approaches infinity for atoms that are closely spaced. Slater-type²⁹ and Gaussian-type³⁰ orbitals have been implemented in the QEq, which correct for overlapping charge densities. However, computing these orbitals continuously for a large number of atoms is impractical from a computational resource standpoint. A less computationally-demanding alternative is to express the Coulomb interaction using an approximation. Oda and Hirono³⁴ compared several forms for this approximation; the present work utilizes the form for J_{ij} that was found to be the most accurate and transferable, the DasGupta-Huzinaga (DH) equation³⁵

$$J_{ij} = \frac{1}{R_{ij} + \frac{1}{\frac{J_{ii} e^{0.4 R_{ij}}}{2} + \frac{J_{jj} e^{0.4 R_{ij}}}{2}}} \quad (2.34)$$

where R_{ij} is the distance between the atoms.

The QEq scheme is not appropriate for all systems. It provides a good approximation of the equilibrium charges in materials that are close to homogenous, but struggles to

accurately model charge transfer in long-chain polymers, for example, or molecules that undergo broken bonds. This is because the QEq scheme treats the entire atomistic system as one large conductor, resulting in potential non-physical charge transfer. Therefore, it is important to benchmark the charge distribution predictions of QEq against relevant data, such as first principles calculations, to determine the appropriateness of the scheme's application.

2.6 References

1. Lennard-Jones JE. *Proc R Soc Lond A*. 1924;106:463.
2. Morse P. Diatomic molecules according to the wave mechanics. II. vibrational levels. *Phys Rev*. 1929;34(1):57-64. doi: 10.1103/PhysRev.34.57.
3. Buckingham R. The classical equation of state of gaseous helium, neon and argon. *Proc R Soc Lond A-Math Phys Sci*. 1938;168(A933):264-283. doi: 10.1098/rspa.1938.0173.
4. JOHNSON R. Relationship between 2-body interatomic potentials in a lattice model and elastic-constants. *Physical Review B*. 1972;6(6):2094-&. doi: 10.1103/PhysRevB.6.2094.
5. Daw MS, Baskes MI. Embedded-atom method - derivation and application to impurities, surfaces, and other defects in metals. *Physical Review B*. 1984;29(12):6443-6453.
6. HOHENBERG P, KOHN W. Inhomogeneous electron gas. *Phys Rev B*. 1964;136(3B):B864-&. doi: 10.1103/PhysRev.136.B864.
7. Foiles SM, Baskes MI, Daw MS. Embedded-atom-method functions for the fcc metals cu, ag, au, ni, pd, pt, and their alloys. *Physical Review B*. 1986;33(12):7983-7991.
8. ROSE J, SMITH J, GUINEA F, FERRANTE J. Universal features of the equation of state of metals. *Phys Rev B*. 1984;29(6):2963-2969. doi: 10.1103/PhysRevB.29.2963.

9. Liu G, Zhang GJ, Ding XD, Sun J, Chen KH. Modeling the strengthening response to aging process of heat-treatable aluminum alloys containing plate/disc- or rod/needle-shaped precipitates. *Mater Sci Eng A-Struct Mater Prop Microstruct Process*. 2003;344(1-2):113-124.
10. ERCOLESSI F, ADAMS J. Interatomic potentials from 1st-principles calculations - the force-matching method. *Europhys Lett*. 1994;26(8):583-588. doi: 10.1209/0295-5075/26/8/005.
11. ROHRER C. Interatomic potentials for al-cu-ag solid-solutions. *Modell Simul Mater Sci Eng*. 1994;2(1):119-134. doi: 10.1088/0965-0393/2/1/009.
12. LANDMAN U, LUEDTKE W, RINGER E. Atomistic mechanisms of adhesive contact formation and interfacial processes. *Wear*. 1992;153(1):3-30. doi: 10.1016/0043-1648(92)90258-A.
13. Kelchner CL, Plimpton SJ, Hamilton JC. Dislocation nucleation and defect structure during surface indentation. *Physical Review B*. 1998;58(17):11085-11088.
14. Allen MP, Tildesley DJ, eds. *Computer simulation in chemical physics*. Dordrecht ; Boston: Kluwer Academic Publishers; 1993.
<http://www2.lib.ncsu.edu/catalog/record/DUKE001118237>.
15. WOODCOCK L. Isothermal molecular dynamics calculations for liquid salts. *Chem Phys Lett*. 1971;10(3):257-&. doi: 10.1016/0009-2614(71)80281-6.

16. Hoover WG. *Molecular dynamics lecture notes in physics*. Berlin: Springer-Verlag; 1986.
17. Timsit RS. Electrical contact resistance: Properties of stationary interfaces. *Ieee Transactions on Components and Packaging Technologies*. 1999;22(1):85-98.
18. Schall JD, Padgett CW, Brenner DW. Ad hoc continuum-atomistic thermostat for modeling heat flow in molecular dynamics simulations. *Molecular Simulation*. 2005;31(4):283-288.
19. Ivanov D, Zhigilei L. Combined atomistic-continuum modeling of short-pulse laser melting and disintegration of metal films. *Phys Rev B*. 2003;68(6):064114. doi: 10.1103/PhysRevB.68.064114.
20. Zhigilei LV, Lin ZB, Ivanov DS. Atomistic modeling of short pulse laser ablation of metals: Connections between melting, spallation, and phase explosion. *Journal of Physical Chemistry C*. 2009;113(27):11892-11906.
21. Lin Z, Zhigilei LV, Celli V. Electron-phonon coupling and electron heat capacity of metals under conditions of strong electron-phonon nonequilibrium. *Physical Review B*. 2008;77(7):-.
22. Wagner GJ, Liu WK. Coupling of atomistic and continuum simulations using a bridging scale decomposition. *Journal of Computational Physics*. 2003;190(1):249-274.

23. Wagner GJ, Jones RE, Templeton JA, Parks ML. An atomistic-to-continuum coupling method for heat transfer in solids. *Comput Methods Appl Mech Eng.* 2008;197(41-42):3351-3365. doi: 10.1016/j.cma.2008.02.004.
24. Padgett CW, Brenner DW. A continuum-atomistic method for incorporating joule heating into classical molecular dynamics simulations. *Molecular Simulation.* 2005;31(11):749-757.
25. Irving DL, Padgett CW, Brenner DW. Coupled molecular dynamics/continuum simulations of joule heating and melting of isolated copper-aluminum asperity contacts. *Modell Simul Mater Sci Eng.* 2009;17(1):-.
26. Irving DL, Padgett CW, Guo Y, Mintmire JW, Brenner DW. Multiscale modeling of metal-metal contact dynamics under high electromagnetic stress: Timescales and mechanisms for joule melting of al-cu asperities. *IEEE Trans Magn.* 2009;45(1):331-335.
27. *Fundamentals of heat and mass transfer.* Hoboken, NJ: John Wiley; 2007.
<http://www2.lib.ncsu.edu/catalog/record/DUKE003789783>.
28. Timsit RS, Slade PG, ed. *Electrical contacts: Principles and applications.* New York: Marcel Dekker; 1999.
29. Rappe AK, Goddard WA. Charge equilibration for molecular-dynamics simulations. *J Phys Chem.* 1991;95(8):3358-3363.

30. Streitzi FH, Mintmire JW. Electrostatic potentials for metal-oxide surfaces and interfaces. *Physical Review B*. 1994;50(16):11996-12003.
31. Yu J, Sinnott SB, Phillpot SR. Charge optimized many-body potential for the si/SiO₂ system. *Phys Rev B*. 2007;75(8):085311. doi: 10.1103/PhysRevB.75.085311.
32. Iczkowski R, Margrave JL. Electronegativity. *J Am Chem Soc*. 1961;83(17):3547-&.
33. Parr RG, Pearson RG. ABSOLUTE HARDNESS - COMPANION PARAMETER TO ABSOLUTE ELECTRONEGATIVITY. *J Am Chem Soc*. 1983;105(26):7512-7516.
34. Oda A, Hirono S. Geometry-dependent atomic charge calculations using charge equilibration method with empirical two-center coulombic terms. *Theochem-J Mol Struct*. 2003;634:159-170. doi: 10.1016/S0166-1280(03)00338-5.
35. DASGUPTA A, HUZINAGA S. New developments in cndo molecular-orbital theory. *Theor Chim Acta*. 1974;35(4):329-340. doi: 10.1007/BF00548482.

2.7 Tables and Figures

Table 2.1 Parameters used for fitting the pair interaction in the Embedded Atom Method potential for Au⁷.

Parameter	Value for Au
Z_0	11.0
α	1.4475
β	0.1269
ν	2
n_s	1.0809
Atomic Configuration	$5d^{10} 6s^1$

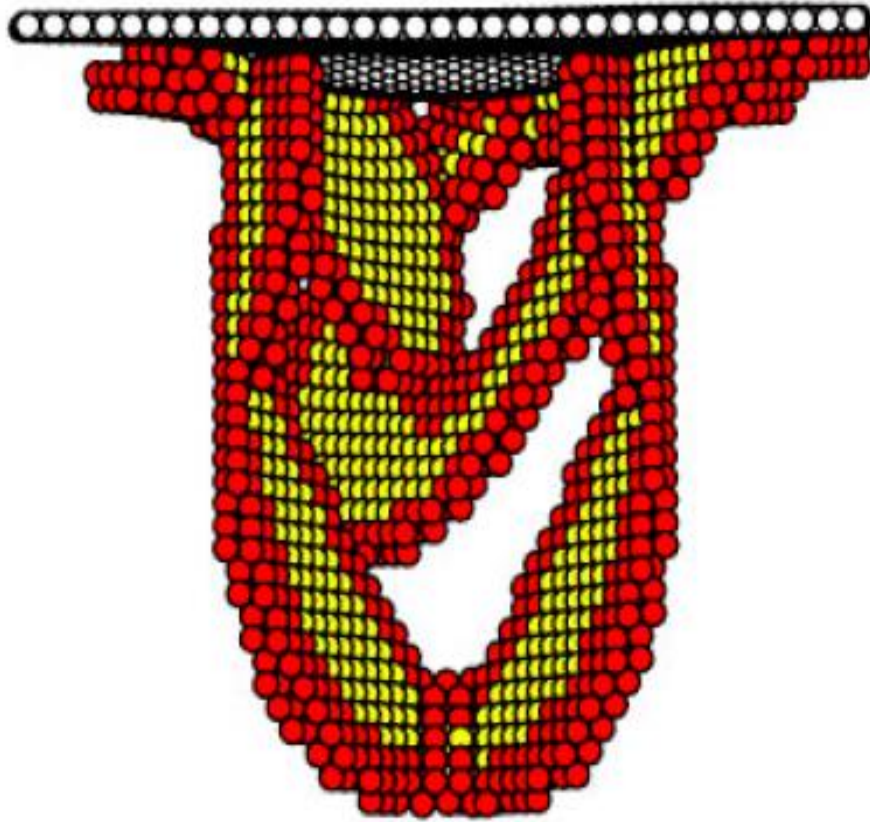


Figure 2.1 Image from Kelchner et al¹³ depicting subsurface dislocation loop formation during nanoindentation.

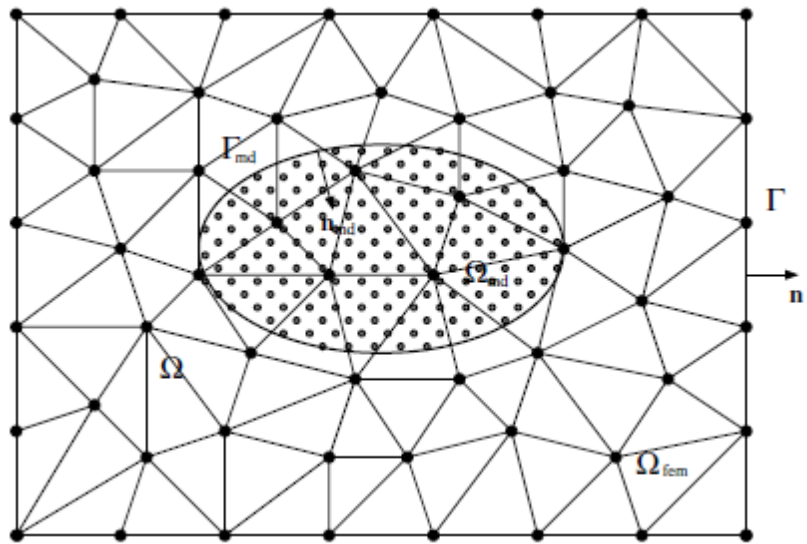


Figure 2.2 Multi-scale scheme of Wagner²³ in which the molecular dynamics simulation is embedded within a finite element domain, and continuum heat flow solutions are conveyed to the atoms at the nodal points.

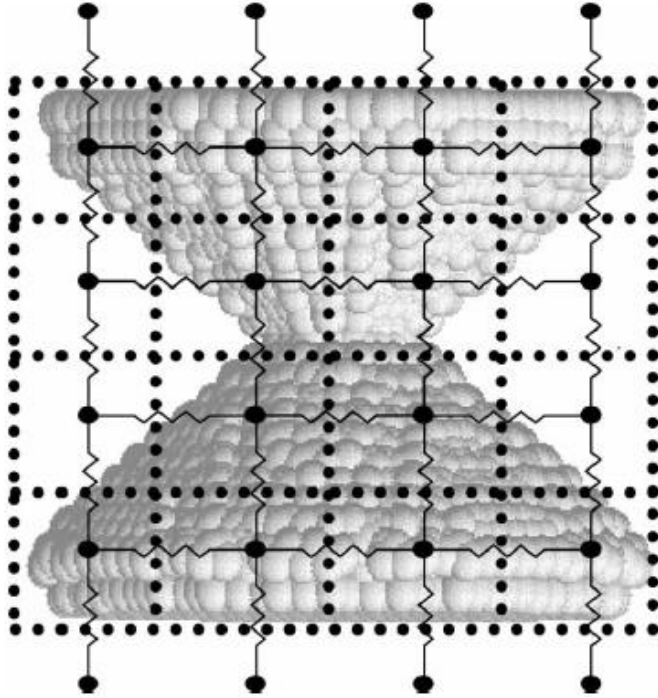


Figure 2.3 Illustration of the FD/MD multiscale approach²⁴ in which a network of resistors is superimposed over an atomistic system, allowing finite difference solutions of continuum thermal and electrical current equations to be determined.

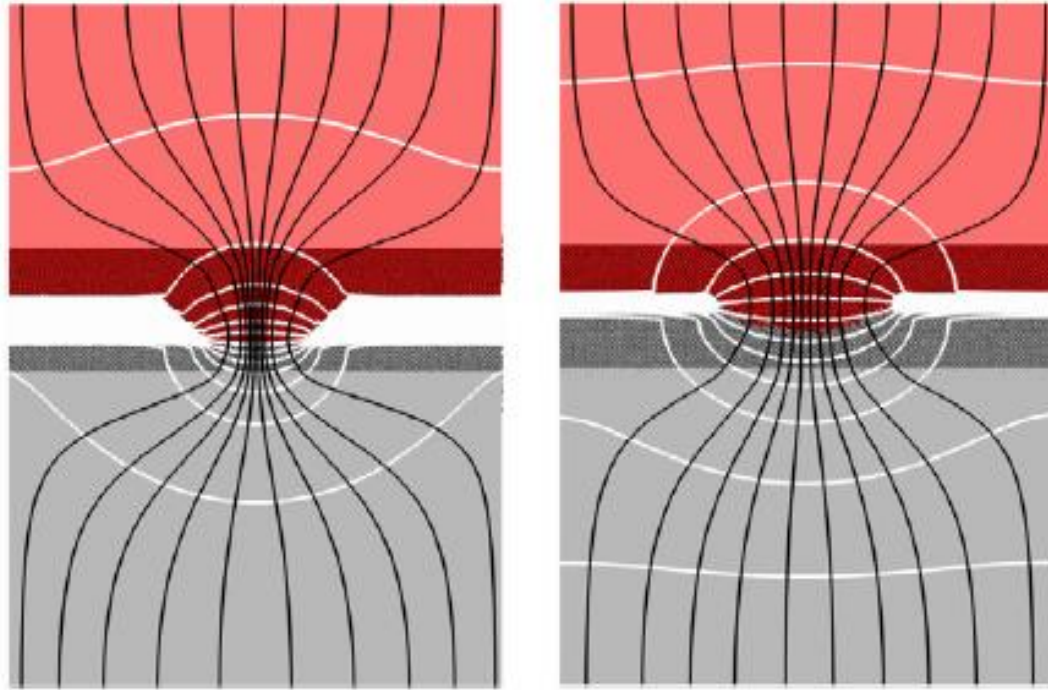


Figure 2.4 Illustration of the increase in current density and heat flow (black lines) and thermal gradients (white lines) as a contact area broadens from left to right²⁵.

CHAPTER 3 – ASPERITIES UNDER ELECTROMAGNETIC STRESS

3.1 Nanotribology

The surfaces of contacting metals contain nanoscale protrusions, or asperities, through which contact forces are transmitted. In an electrically conducting interface, the asperities become the conduits of current. It is known that plastic deformation of the asperities influences the contact area¹, which in turn alters contact resistance. Therefore, understanding the mechanisms of asperity wear is critical to ensuring the integrity of electrical contacts

The role of asperities in nanotribology is well-studied², particularly in the domain of modeling. Nanoindentation of metals, in particular, has been the subject of many molecular dynamics (MD) simulations. Li *et al*³ modeled the indentation of a flat $\langle 111 \rangle$ Al surface using a spherical indenter and witnessed glide loops emanating on three equivalent $\{111\}\langle 110 \rangle$ slip systems. A similar simulation of the indentation of a (111) Au surface by Kelchner and colleagues⁴ also produced dislocation loops, but without the same three-fold symmetry witnessed by Li. The presence of surface steps during nanoindentation of (100) Al was found by Hirel *et al*⁵ to strongly influence the critical size for a stable dislocation half-loop, below which a dislocation will retreat back to the surface. Indentation of a (111) Au surface with steps performed by Zimmerman⁶ indicated that close proximity to a surface step resulted in a greater dependence on the crystallographic orientation for dislocation morphology.

Adhesion and dynamic frictional wear are important components in the contact area between two conducting interfaces. Macroscopic phenomena in tribological wear are known

to break down when examined on the asperity scale⁷. A review of the recent progress made in this area has been published by Dedkov⁸. Landman and Luedtke⁹ carried out an MD simulation of a tapered Au tip brought slowly into contact with a Ni (001) substrate, and revealed “flattening” of the tip was accomplished by rearrangement of peripheral atoms to form an interstitial defect core region. Buldum *et al*¹⁰ found the contact area increase during asperity tip flattening to be discontinuous. This affects the conductance measured at the asperity contact, which increases with area as more electronic states fall under the Fermi level. Contact area increase during sliding was also witnessed by Nieminen¹¹ for a Cu asperity on a Cu substrate. A paraboloid asperity tip was reduced in height by the climb of two successive edge dislocations. The interlayer sliding was always found to be within the asperity rather than at the tip/surface interface, so that the frictional force was found not to increase despite an increase in contact area.

The friction encountered by a sliding asperity can give rise to the phenomenon of stick-slip. This erratic stop-start motion of the tip results from the competing components of static friction and inertia¹². The disparity between macroscopic and microscopic velocity limits of stick-slip¹³ calls for an atomistic-scale analysis. Luan and Robbins⁷ found that the critical velocity, beyond which stick-slip ceased to occur, increased with sliding mass. A comprehensive review of this area has been published by Braun¹⁴.

Adhesion in asperity contacts has been tackled extensively. The Srolovitz group performed Embedded Atom Method (EAM) simulations of a gold asperity contacting and separating from a flat substrate¹⁵ to determine the evolution of the force and conductance through the asperity. Srolovitz also used a version of the EAM modified to vary the

interfacial (and therefore, adhesive) energy¹⁶; higher strength of adhesion was found to be associated with more material transfer when an asperity contact was separated. Work by the Robbins group demonstrated the breakdown of continuum mechanics equations when applied to asperities with varying atomic structures and adhesion⁷.

In short, prior research on asperities has contributed great insight into asperity adhesion and contact force. However, there are still many unanswered questions, primarily in regards to Joule heating effects that exist with an applied electrical potential. In each of the aforementioned MD simulations the electronic degrees of freedom have been course-grained to allow for large systems, because determining energies via quantum mechanics in a first principles approach would impose too great a scale limitation in both size and time domains. This loss of electronic detail is manifest in the inaccuracy of thermal transport coefficients for a metallic system. Heat conduction in metals occurs primarily via electrons; without an explicit treatment of the electrons, analytic potentials cannot accurately treat heat flow in a metal. The importance of this omission comes down to the engineering application for which the asperity contact is being studied. In the following sections, two applications are highlighted for which neglecting electronic effects in asperity contacts prevents succinct analysis.

3.2 Radio Frequency Micro-Electromechanical Systems

Micro-electromechanical systems (MEMS) comprise a burgeoning industry of signal processing and communications, impelled by industry trends towards miniaturization. The technology allows batch fabrication of microscale devices, with consequent reductions in

cost and size as well as improved performance as corollaries. MEMS components have myriad arenas of use, such as accelerometers, pressure sensors, and ink-jet nozzles. Another such application for MEMS is the radio frequency (RF) switch, which is the subject of great interest because of its many inherent advantages over solid state switches. Among these are high linearity and low power consumption (since the switch does not draw current when disengaged)¹⁷. RF MEMS switches also have low insertion loss, wide temperature applicability and low cost¹⁸. These switches have slower switching speeds than solid state devices, and, because they operate mechanically, are subject to contact physics which further complicate usage. While the former is a design consideration, the latter can be a major impediment to commercial use.

RF MEMS switches fall into essentially two different classes: resistive and capacitive. Resistive switches feature metal-to-metal series-configured ohmic contacts (i.e. Au-Au or Au-Ni)¹⁹. Capacitive switches are parallel-configured and contain a thin dielectric film and an air gap separating metallic contact surfaces (e.g. silicon nitride on Au)¹⁹. Schematic illustrations of both designs are shown in Figure 3.1¹⁸. For the series switch, electrostatic actuation pulls the upper electrode in contact with a lower electrode, allowing RF signals to pass. In the capacitive switch, the electrostatic actuation modulates the capacitance between the pull-down electrode and the membrane above. This capacitance increases greatly when the bridge is pulled down, restricting the flow of an RF signal. For both types, the pull-down electrodes are typically¹⁹ $\sim 100 \times 100 \mu\text{m}^2$ with a gap of $1 \mu\text{m}$, and the two contacting areas are $\sim 3 \times 3 \mu\text{m}^2$.

Resistive and capacitive switches have different frequency response behavior in accordance with their dissimilar electrical circuits, which ultimately dictates their suitability for a given application. As shown by Brown²⁰, the isolation of a series switch degrades with the square of frequency, whereas that of a parallel-configured switch remains relatively constant at high frequencies, but drops off significantly at lower frequencies (below 1Ghz).

The two classes of RF MEMS switches also have different obstacles to their long-term reliability. In capacitive switches, the high- ϵ materials needed for the pull-down electrodes are prone to charging when an applied voltage is present²¹, which over time can cause a drift in device performance. Still, without an ohmic contact, capacitive switches typically have much greater lifetimes than series contact switches that are subject to adhesion, material transfer and surface damage. These phenomena all conspire to increase device resistance, which is crippling for a MEMS switch.

As discussed in the continuum heating section of Chapter 2, a small amount of voltage will significantly increase the temperature of an electrical contact. With such localized temperature elevation occurring at the asperities in a contact, the potential for a variety of failure incidents becomes a large concern with RF MEMS. In an experiment using a nanoadhesion apparatus to simulate switching, Patton and Zabinski²² tested the effect of electrical current on adhesive failure. The results at high current ($\sim 1\text{mA}$) suggested the presence of melting and re-solidification, with post-failure SEM images (e.g. left image of Figure 3.2) showing the remnants of nanowires. A schematic illustration in the right of Figure 3.2 highlights the formation of nanowires between the contacts.

Patton and Zabinksi also found material transfer between contacts, which was in accordance with findings²³ by Hyman and Mehregany, who witnessed cathode-to-anode material transfer and asperity melting/flattening. The latter is also evidence that, prior to melting, contact heating can soften the asperities sufficiently for them to be compressed, which reduces resistance by creating more contact surface area. Work by Kruglick revealed explosive failure of a MEMS switch with a voltage of 5 V²⁴. The author surmised that a thin bridge formed between contacts had sublimated, but could not be sure of the exact mechanism.

While the theoretical and experimental evidence both point to material transfer at asperity contacts, the experiments also strongly suggest that the mechanisms are exacerbated by Joule-heating during current transfer. This is an element that is beyond the resolution of traditional empirical potentials. Capturing the deformation of asperity contacts while considering the electromagnetic components of the stress are therefore of great interest in RF MEMS research.

3.3 Electromagnetic Launchers

The desire for non-volatile ordnance and the concomitant advantages in transportation and storage safety has led to the adoption and development of the electromagnetic launcher (EML) or railgun, the schematics of which are displayed in Figure 3.3²⁵. By running a current in a loop through Cu rails and an Al armature, an EML can exploit an immense Lorentz force to propel a projectile up to 5 km/s. A laboratory device as used by Gee²⁶, for

example, comprised a 7m-long rail with a 40mm square “bore” (or displaced cross-sectional width).

Accelerating the armature down the rails produces an extreme amount of friction, and the operational principle dictates that electrical contact must be maintained, preferably for multiple firings. Therefore, contact materials must be able to withstand very high temperatures generated by power dissipation comparable to laser surface melting²⁷ in addition to the frictional heating effects of sliding. The deformation mechanisms of railguns include armature melting and erosion (Figure 3.4²⁸), intermixing of Cu atoms with molten Al atoms, and arcing due to loss of electrical contact. All of these can conspire to reduce longevity of the launcher and reliable operation in naval applications.

Continuum models have been developed to couple the electromagnetics and solid mechanics of the rail and armature, providing insight into the engineering design of EMLs^{29,30}. However, the problems of premature rail wear have remained mostly unsolved. Irving *et al*³¹ simulated compression of an asperity in an Al-Cu contact. It was reported that for an applied potential of 0.3V (greater than the melting voltage of Al but less than that of Cu) the molten Al formed a meniscus around a Cu asperity, and the ensuing change in contact geometry dictated current fluctuations. There was also substantial atomic intermixing of Cu into Al, consistent with findings by Dutta *et al*³². A critical next step would be to include sliding dynamics into the simulation in order to better understand the effects of friction on tip erosion and substrate deformation.

3.4 Pull-Apart of Gold RF MEMS Asperity Contacts

The aim of the RF MEMS portion of the current study is to extend the analysis of previous research on the separation of asperity contacts by introducing the non-steady state thermal effects of Joule heating from an electrical current. The intended contributions to the RF MEMS literature are two-fold. The first is to better understand the effects of Joule heating on the plastic deformation processes during contact de-adhesion. The second goal is to potentially gain insight as to the mechanisms responsible for the experimentally-observed material transfer across contacts. The following sections outline the atomistic systems used, the simulation setup details, and the results from pulling apart the asperity contacts.

3.4.1 Multiscale asperity tip construction – From device to atomistic

Recent continuum simulations of gold RF MEMS switches constructed using fractal model geometry³³ have resulted in new insights into the topography of asperity contacts. For the RF MEMS asperity simulations reported here, we use the surface topography generated by this continuum-level research to inform our atomistic geometry. The progression from continuum to atomistic is summarized using sequentially magnified images in Figure 3.5. The highest of many asperities from the continuum system is selected, and, using its geometry, the very top was carved out of a block of fcc gold atoms oriented with the [111] direction normal to the asperity tip. It can be seen in the resulting atomic structure that the asperity curvature is reduced to three layered monolayers at the atomistic scale, much flatter than the asperity tips simulated in previous research such as the Srolovitz studies^{15,16}.

Constructing a 1:1 scale asperity from the fractal data would require a contacting monolayer of 565 nm^2 and a substrate of 7500 nm^2 . Abiding by these dimensions, equipping the substrate with adequate depth for subsurface plastic events to propagate would result in an atomic system approaching $\sim 10^8$ atoms, which is presently beyond our computing capabilities. To build systems that are more tenable, a sharpening factor was applied to the raw fractal data that uniformly scales the dimensions of the asperity tip while preserving the geometric features. This decreases the substrate area, reducing the required number of atoms to 10^6 - 10^7 . All future references to this scaling factor will be in the form of “ nx ,” where n is the integer factor by which the fractal data is scaled; contact area changes by $1/n^2$.

The fully-constructed atomistic system for the gold RF MEMS contact is illustrated in Figure 3.6. Crystallographic directions for the system are labeled and atoms colored by a local symmetry parameter⁴, which formulates the extent to which an atom is distorted from an ideal bulk lattice point by analyzing nearest neighbor distances. In this figure, the blue atoms are bulk and red atoms denote a surface. The contacting monolayer is bulk because it is in the correct fcc stacking sequence of its opposing flat substrate. Periodic boundaries are applied in each of the three directions. The dimensions of the contact and substrate vary with the aforementioned sharpening factor. Table 3.1 reports the dimensions for the four sharpening factors used in this study.

3.4.2 Simulation details

The atomic forces for all gold simulations were calculated using the embedded atom method potential for gold developed by Foiles³⁴. Numerical integration of the forces uses a Gear

predictor-corrector algorithm and a time step of one femtosecond. Each system began with an equilibration at 300 K for three picoseconds using a Langevin thermostat. The atoms were allowed to relax via zero-pressure conditions at the boundaries, during which time the lattice parameter expanded from gold's zero K value of 4.08 Å to 4.095 Å. To simulate contact pull-apart, a constant engineering strain rate of 0.0043 picosecond⁻¹ was applied in the direction perpendicular to the asperity contact.

For the simulations that include an applied electrical potential, the finite difference grid for the continuum portion of the simulation is superimposed on the atomistic system with boundary lengths matching the atomistic system in the directions parallel to the contact, but twice the substrate length in the transverse direction. Since the atomistic system terminates in periodic boundaries in the asperity direction, this will result in phononic heat transfer from one end of the simulation to the other as atoms move across the periodic boundary. This is inconsistent with the continuum solution, as finite difference grids on opposite ends of the atomistic system are not connected by thermal resistors. However, this issue is justifiable given that the electronic heat transfer dominates the phononic transfer in metals. Since the continuum thermostat is correcting the atomic temperatures, the atomic movement across the period boundaries in the asperity direction will not influence the overall heat transfer dynamics.

The first section consists of simulations of “cold” gold contacts (without an applied voltage) pulling apart, and investigates the deformation mechanisms at work during the pull-apart process. The simulations are run with varying contact areas to ascertain if molecular dynamics can capture the experimentally-observed material transfer between contacts, and

whether this can be “scaled” to device level in order to agree with experiment. This is where the utilization of asperity geometry derived from continuum modeling is potentially advantageous, in that the modeling process inherently assumes a multiscale approach.

The second section of pull-apart simulations with current flow seek to shed light on the effect of Joule heating on the deformation mechanisms observed in the cold simulations. This is the primary topic of interest here that has yet to be addressed in modeling of RF MEMS contacts. The “hot” gold contact simulations are also used to further explore the material transfer and wear mechanisms, including melting and boiling of nanowires, which appear from the experimental research to be among the main culprits of premature RF MEMS device wear.

3.4.3 “Cold” contact pull-apart

Our analysis begins by pulling apart a “cold” asperity contact (“null” or zero voltage) using the constant strain rate on the $4x$ gold system. A sequence of snapshots from the null-voltage simulation is illustrated in Figure 3.7. The atoms are colored by the aforementioned local symmetry parameter, and all atoms of bulk symmetry are removed, leaving only those associated with a surface (red) or defects/thermal noise (white). As the contact begins to pull apart, partial dislocations nucleate at the step edges surrounding the contacting monolayer, and the resultant stacking faults (SFs) grow into the bulk substrates along the preferred slip systems. The stacking faults intersect to form a Thompson tetrahedron, shown in close-up detail in Figure 3.8, at which point the SF planes must slice through one another to continue growing. At this point, it becomes preferable for the stress to be taken up within the material

between the contact surfaces. This transferal of load begins the drawing of material into a wire, simultaneously reversing the direction of SF growth, because the contact surfaces snap back as a result of contact yielding and wire drawing. Therefore, substrate stress that was once tensile becomes compressive. The wire continues to lengthen until it fractures at a monatomic cross-section.

If nanowires formed during pull-apart are among the primary contributors to material transfer in RF MEMS switch contacts, then the volume of atoms comprising the wire must be an appreciable portion of the transferred volume that is observed in experimental MEMS switches. Of course, the atomistic systems constructed for the present work represent only a single asperity of a vast population residing on a real contact surface. Therefore, to make any statement about whether nanowires might constitute a major material transfer mechanism, we must extrapolate from our atomistic contact scale up to device contact scale. This requires us to estimate a relationship between contact size and the size of the nanowire formed. To accomplish this, the null-voltage pull-apart simulations were carried out for the four atomistic systems that result from varying the sharpening factor, and the number of atoms taken up into the wire was measured for each system.

A number of assumptions are required to extrapolate from the atomistic results to the device scale. The first is that we assume the relationship between contact area and nanowire size is linear. Although a small sample size, our results for the four atomistic systems seem to support this. In addition, a linear relationship intuitively follows from the fact that the nanowire volume is composed of the monolayers forming the initial contact. As the area of the monolayers increases, so too should the nanowire volume. A linear relationship also

poses the implicit assumption that the myriad asperities in a contact can essentially be treated as a single asperity with contact area equivalent to the sum of individual asperity contact areas. In a homogenous contact material, it seems reasonable to expect that the asperity deformation mechanisms illustrated in Figure 3.7 will be common to all contacting asperities regardless of size, supporting this assumption. And finally, given the highly disordered nature of the nanowire volume, we make the assumption that the atoms have no tendency to remain attached to either contact, meaning the atoms will be divided roughly in half between the two surfaces upon fracture.

Will these caveats out of the way, Figure 3.9 plots the nanowire atom count versus initial contact area for each “ nx ” atomistic system. A linear regression line fit to the data is extrapolated to the experimentally observed device-scale contact area, obtained from a recent investigation³⁵ in which SEM images were used to estimate material transfer in an accelerated RF MEMS contact simulator. The units of the plot are shown on logarithmic scales for expositional clarity. The linear extrapolation to this area ($1 \times 10^6 \text{ nm}^2$) predicts ~25 million atoms in a wire, or ~12.5 million amenable to transfer. This is an upper bound, as not all the atoms will necessarily transfer for a given cycle, but the figure agrees well with the contact simulator experiment in which a volume of $1.19 \times 10^{-4} \text{ } \mu\text{m}^3$ was transferred per cycle³⁵, equivalent to approximately 7 million atoms. This doesn’t provide a definitive statement about the mechanisms involved in material transfer, but rather makes a case that, at the very least, nanowires formed between metallic contacts during separation contain enough atoms to serve as a source for much of the volume transferred.

3.4.4 Effect of Joule heating during contact pull-apart

The next question we study is the how the deformation mechanisms that one observes in the null-voltage simulations are affected by Joule heating from current flow. Three separate simulations were carried out using the $4x$ system: two were performed under constant applied electrical potentials of 0.1 V and 0.2 V, while another was completed with constant current fixed at 0.01 A while allowing the voltage to vary up to a chosen cutoff value (0.43 V in this case, corresponding to the melting voltage of gold). As discussed in the continuum heating section of Chapter 2, the constant voltage conditions will produce steady-state temperature elevations at the contact predicted by the voltage-temperature relation (Equation 2.10). The superheated temperatures determined by the finite difference thermostat during the simulation runs for 0.1 V and 0.2 V were 430 K and 684 K, respectively, which are in close agreement with V-T relation predictions of 438 K and 706 K. The voltage drop in the constant current simulations changes as the contact area evolves, thereby dynamically altering the temperature.

Figure 3.10 reports sequential snapshots of the constant-voltage simulations. The snapshots are taken at 15, 25 and 25 picoseconds of simulation time for each voltage, and the atoms are colored by local symmetry as described previously. It is apparent from the symmetry-colored images that the stacking faults which are generated from the partial dislocations formed at the contact step-edges grow far larger than in the absence of electrical current. The Joule heating enhances dislocation nucleation and stacking fault mobility, leading to greater plastic damage as the voltage increases.

Another feature witnessed in these snapshots is the aspect ratio of the wire 25 picoseconds into the simulations. Increasing voltage slows the drawing of the wire, which can be traced to the deformation mechanism detailed in the previous section. Where the stacking faults became pinned in the null-voltage pull-apart, transferring load to the contact which then pulled the wire, Joule heating in the “hot” contact pull-apart enhances dislocation motion and allows the stacking faults to slice through one another. This continues the stress accommodation in the bulk and delays the contact yielding. The net result is slower wire drawing compared to the null-voltage pull-apart.

While the constant voltage conditions slow the wire-pulling process, applying constant current has the opposite effect. Figure 3.11 presents a comparison of the nanowires after 15 picoseconds for all three of the simulations with Joule heating. The simulation with constant current has drawn a longer wire than the simulations with constant voltage, while the plastic deformation in the substrate is less and bears closer resemblance to that of the null-voltage simulation. The explanation for this disparity in behavior can be traced to the voltage evolution, which is scaled to maintain the constant 0.01 A of current. As a result, the initial potential drop consisted of only millivolts, and the contact temperature remained at 300 K as in the null-V run. Thus, the initial plastic deformation with constant current closely resembles that of the null-voltage simulation. The contact resistance increases during straining, which causes the voltage to increase commensurately to maintain the current. This resulting surge in the voltage, up to the cutoff, is plotted in Figure 3.12. The resultant heating at the contact enhances its ductility; when the stacking faults interact at the summit of

the tetrahedron, the impediment to their motion transitions the strain accommodation to the now-ductile contact spot, drawing out a wire rather than continuing stacking fault growth.

A comparison of the temperature-colored snapshots from the 0.2 V and 0.01 A simulations in Figure 3.13 illustrates the effect different electrical conditions have on the temperature evolution of the contact. The entire substrate in the constant voltage simulation is elevated to above 400 K early in the simulation, with local superheating of greater than 600 K at the contact slowly spreading from the center. Under constant current, both substrate and contact remain near 300 K until a sudden spike in resistance quickly produces asperity temperatures above 600 K after 15 ps, and above melting (1070 K for this potential) by 17.5 ps.

3.4.5 Material transfer mechanisms

As detailed in Section 3.4.3, the wires between contacts appear to provide ample volume of atoms amenable to material transfer when scaled to the device-size. The mechanism(s) that may contribute to the transfer are still unclear and require further analysis. Among the most likely candidates are: 1) atoms comprising a liquefied wire that, upon wire severance, solidify upon the surface to which they are still attached; 2) sublimation if voltage broaches the boiling limit; and 3) evaporation of atoms due to a high electric field created between fracture surfaces of the wire. While the former two may be captured by the finite difference thermostat, the latter is not a phenomenon which this methodology is currently capable of simulating. To explore the feasibility of field evaporation in this system, exploratory calculations have been performed using kinetic Monte Carlo simulations based on the image-

hump model, a first-principles description³⁶ of the energy barrier resisting the pull-away of a charged atom from an electric field. This preliminary work indicated that, short of colossal electrical potentials which could not be sustained through an intact contact, the time scale of evaporation events would exceed the switching times of RF MEMS contacts, precluding field evaporation from being a plausible mechanism of material transfer.

Melting certainly occurs for the asperities subjected to constant-current, as well as any constant voltage exceeding 0.43 V. If the voltage cutoff of the constant current simulations were much higher than 0.43 V, the wire between contacts would ultimately be expected to boil. This was the case when the constant current simulation was repeated with a voltage cutoff of 2.0 V. As shown in Figure 3.14, after 16 picoseconds the entire nanowire is above the boiling point of gold (3239 K). With the nanowire vaporized, an electrical field would form between the contacts from the applied voltage. Collisions among vapor phase atoms could potentially produce ions that would then follow the field to the positively charged contact. The results from the RF MEMS contact simulator strongly suggest that the direction of material transfer is dictated by the electric field and not by device orientation³⁵. Nanowire formation and vaporization, not melting, would seem to be the mechanism most consistent with directional material transfer.

3.5 Sliding of Asperity Contacts in Electromagnetic Launchers (EMLs)

The next application for the continuum/atomistic multiscale methodology is asperities in aluminum-copper contacts representative of the interfaces between the armature and rail of an electromagnetic launcher (EML). The simulations are intended to extend the analysis of Irving^{31,37} by including the effects of sliding wear into the analysis. As with the gold simulations, the atomistic systems used and simulation setup details are outlined, followed by results and analysis.

3.5.1 Asperity tip construction and simulation details

Two different atomistic systems are used, each containing approximately 1.9 million atoms. Both systems contain two opposing substrates, one each of copper and aluminum, with thickness 7.2 nm and cross-sectional area 1,720 nm². The “top” substrate contains a truncated trapezoidal asperity tip of area 196 nm² and height 1.9 nm. Both the substrates and the asperity are [100]-oriented; the faceted sides of the asperity are (111) planes. The atomistic systems differ by the choice of materials for the top and bottom substrates. An illustrative example of the geometry is shown in Figure 3.15. Each system is periodic in the non-asperity dimensions and free surface boundaries in the direction of the asperity.

The atomic forces were calculated using the embedded atom method (EAM) potential developed by Liu³⁸ for Al and Cu, with a Gear predictor-corrector algorithm and a time step of 1×10^{-15} s. The bottom substrate is attached to a rigid plane, and the top substrate is brought into contact by compressing using a plane under constant force ($\sigma_{11}=55\text{MPa}$) for a duration of 10 picoseconds. During this indentation phase a Hoover thermostat is used to

maintain a constant 300K. The top substrate is then accelerated to a velocity of 500 ms^{-1} over 10 ps while still under constant compressive force. Sliding is maintained at a constant 500 ms^{-1} for at least 20 ps.

Due to the high sliding rate and consequent frictional heating, the continuum finite difference grid is implemented both with and without an applied voltage. The grid is superimposed on the atomistic system with boundary lengths matching the atomistic system in the periodic directions, but extended to three times the atomic thickness in the compression (asperity) direction for the reasons described in Section 3.4.2. An illustration of the atomistic and continuum construction is presented in Figure 3.16.

The following section contains the results from simulations of compression and sliding of the Al/Cu asperity contacts, both “cold” and with 0.2 V applied. The goal is to better understand the effect of Joule heating on the deformation mechanisms associated with a sliding asperity tip in an aluminum/copper contact. The results from Irving’s Al/Cu simulations³¹ corroborated at the atomistic level experimentally-observed effects, such as intermixing of Cu and Al atoms, which are exacerbated by the presence of Joule heating. The present work extends that analysis with the inclusion of sliding dynamics.

3.5.2 Al/Cu sliding simulations

Figure 3.17 shows asperity tip sliding for the system with an Al top substrate and asperity tip on a Cu substrate. Sequential snapshots taken at sliding times of 5, 10, and 15 picoseconds are displayed from top to bottom; the left and right columns are the results with 0 and 0.2V

applied, respectively. The images contain only atoms with non-bulk configurations as determined by their local symmetry parameter.

The sliding force in the asperity produces a shear strain which is taken up in the asperity tip. The result of this strain in the absence of voltage is deformation by the successive slip of atomic planes within the tip as partial dislocations are nucleated at edges of contact between the asperity and bottom substrate, shown in Figure 3.18. This mechanism was also reported by Nieminen *et al*¹¹. The bottom asperity layer remains in contact with the Cu substrate, and the pyramid shape of the tip is distorted. The partial dislocations grow through the substrates on the favorable $\{111\}$ planes, leaving behind stacking faults.

Applying a potential of 0.2V across the contact changes the results, as the images in the right column of Figure 3.17 depict. The Joule heating produces a contact temperature of 730 K, enhancing the ductility of the Al which melts at 939K (with this EAM potential). The resulting softness of the Al asperity allows it to slide on the Cu substrate without inducing dislocations within the Cu substrate. Partial dislocations and stacking faults are still present in the Al substrate, although obscured by thermal noise in Figure 3.17. The asperity deformation still contains a component of planar slip, but the strain is no longer accommodated homogeneously as the tip itself begins to disorder. The bottom two images in Figure 3.17 show that the deformed asperity tip preserves its symmetry with respect to the compressive direction in the absence of voltage, but not in the presence of Joule heating. As the asperity tip erodes, it begins to leave behind Al deposits on the substrate, consistent with experiment.

Figure 3.19 presents snapshots from a similar set of simulations, but this time with a Cu top substrate/asperity and Al bottom substrate. As with Figure 3.17, the left and right columns are 0V and 0.2V, respectively, and the top to bottom progression shows sliding durations of 5, 10, and 15 picoseconds. The Cu substrate incurs more stacking fault generation than the Al top substrate in Figure 3.17. This is likely a combination of two factors: First, the higher stiffness of Cu reduces asperity tip wear and accommodates the shear strain by nucleating and growing more stacking faults; Second, the higher stacking fault energy in Al makes it more averse to growing stacking faults.

The application of 0.2 V to the contact during sliding softens the Al so that molten material is piled up in front of the moving Cu asperity. In contrast to the 0V simulation, the Cu asperity with current flowing undergoes some internal slip and shape change. The elevated contact temperature also dissolves Cu atoms into the disordered Al surface (Figure 3.20), an effect not witnessed with an Al asperity under current. The plowing of the Al substrate and intermixing of species are experimentally-observed³² phenomena that are also consistent with the previous asperity compression modeling³¹.

3.6 References

1. Greenwood.Ja, Williams.Jb. Contact of nominally flat surfaces. *Proceedings of the Royal Society of London Series a-Mathematical and Physical Sciences*. 1966;295(1442):300-&.
2. Szlufarska I, Chandross M, Carpick RW. Recent advances in single-asperity nanotribology. *Journal of Physics D-Applied Physics*. 2008;41(12):-.
3. Li J, Van Vliet KJ, Zhu T, Yip S, Suresh S. Atomistic mechanisms governing elastic limit and incipient plasticity in crystals. *Nature*. 2002;418(6895):307-310.
4. Kelchner CL, Plimpton SJ, Hamilton JC. Dislocation nucleation and defect structure during surface indentation. *Physical Review B*. 1998;58(17):11085-11088.
5. Hirel P, Godet J, Brochard S, Pizzagalli L, Beauchamp P. Determination of activation parameters for dislocation formation from a surface in fcc metals by atomistic simulations. *Physical Review B*. 2008;78(6):-.
6. Zimmerman JA, Kelchner CL, Klein PA, Hamilton JC, Foiles SM. Surface step effects on nanoindentation. *Phys Rev Lett*. 2001;87(16):art. no.-165507.
7. Luan BQ, Robbins MO. Contact of single asperities with varying adhesion: Comparing continuum mechanics to atomistic simulations. *Phys Rev E*. 2006;74(2):17.
8. Dedkov GV. Experimental and theoretical aspects of the modern nanotribology. *Physica Status Solidi a-Applications and Materials Science*. 2000;179(1):3-75.

9. Landman U, Luedtke WD. NANOMECHANICS AND DYNAMICS OF TIP SUBSTRATE INTERACTIONS. *J Vac Sci Technol B*. 1991;9(2):414-423.
10. Buldum A, Ciraci S, Batra IP. Contact, nanoindentation, and sliding friction. *Physical Review B*. 1998;57(4):2468-2476.
11. Nieminen JA, Sutton AP, Pethica JB. Static junction growth during frictional sliding of metals. *Acta Metallurgica Et Materialia*. 1992;40(10):2503-2509.
12. Braun OM, Peyrard M, Bortolani V, Franchini A, Vanossi A. Transition from smooth sliding to stick-slip motion in a single frictional contact. *Physical Review E*. 2005;72(5):-.
13. Braun OM, Peyrard M. Friction in a solid lubricant film. *Physical Review E*. 2001;63(4):art. no.-046110.
14. Braun OM, Naumovets AG. Nanotribology: Microscopic mechanisms of friction. *Surface Science Reports*. 2006;60(6-7):79-158.
15. Cha PR, Srolovitz DJ, Vanderlick TK. Molecular dynamics simulation of single asperity contact. *Acta Materialia*. 2004;52(13):3983-3996.
16. Song J, Srolovitz DJ. Adhesion effects in material transfer in mechanical contacts. *Acta Materialia*. 2006;54(19):5305-5312.
17. Muldavin JB, Rebeiz GM. Inline capacitive and DC-contact MEMS shunt switches. *Microwave and Wireless Components Letters, IEEE*. 2001;11(8):334-336.

18. Rebeiz GM, Muldavin JB. RF MEMS switches and switch circuits. *Microwave Magazine, IEEE*. 2001;2(4):59-71.
19. Yao JJ. RF MEMS from a device perspective. *J Micromech Microeng*. 2000;10(4):R9-R38.
20. Brown ER. RF-MEMS switches for reconfigurable integrated circuits. *IEEE Trans Microw Theory Tech*. 1998;46(11):1868-1880.
21. van Spengen WM, Puers R, Mertens R, De Wolf I. A comprehensive model to predict the charging and reliability of capacitive RF MEMS switches. *J Micromech Microeng*. 2004;14(4):514-521.
22. Patton ST, Zabinski JS. Failure mechanisms of capacitive MEMS RF switch contacts. *Tribology Letters*. 2005;19(4):265-272.
23. Hyman D, Mehregany M. Contact physics of gold microcontacts for MEMS switches. *Ieee Transactions on Components and Packaging Technologies*. 1999;22(3):357-364.
24. Kruglick EJJ, Pister KSJ. Lateral MEMS microcontact considerations. *J Microelectromech Syst*. 1999;8(3):264-271.
25. Harris W. How rail guns work. . Updated 2005.
26. Gee RM, Persad C. Multishot performance of an insulator in a laboratory electromagnetic launcher. *IEEE Trans Magn*. 2001;37(1):257-262.

27. Persad C. Railgun tribology - chemical reactions between contacts. *IEEE Trans Magn.* 2007;43(1):391-396.
28. Watt T, Crawford M. Experimental results from a two-turn 40-mm railgun. *IEEE Trans Magn.* 2009;45(1):490-494.
29. Hopkins D, Stefani F, Hsieh K, Kim B. Analysis of startup behavior in a "C-shaped" armature using linked EMAP3D/DYNA3D finite element codes. *IEEE Trans Magn.* 1999;35(1):59-64. doi: 10.1109/20.738376.
30. Newill J, Powell J, Zielinski A. Coupled finite-element codes for armature design. *IEEE Trans Magn.* 2003;39(1):148-152. doi: 10.1109/TMAG.2002.805873.
31. Irving DL, Padgett CW, Brenner DW. Coupled molecular dynamics/continuum simulations of joule heating and melting of isolated copper-aluminum asperity contacts. *Modell Simul Mater Sci Eng.* 2009;17(1):-.
32. Dutta I, Delaney L, Cleveland B, Persad C, Tang F. Electric-current-induced liquid al deposition, reaction, and flow on cu rails at rail-armature contacts in railguns. *IEEE Trans Magn.* 2009;45(1):272-277.
33. Rezvanian O, Zikry MA, Brown C, Krim J. Surface roughness, asperity contact and gold RFMEMS switch behavior. *J Micromech Microengineering.* 2007;17(10):2006-2015.

34. Foiles SM, Baskes MI, Daw MS. Embedded-atom-method functions for the fcc metals cu, ag, au, ni, pd, pt, and their alloys. *Physical Review B*. 1986;33(12):7983-7991.
35. Yang Z. *Contact material optimization and contact physics in metal-contact microelectromechanical systems (MEMS) switches*. North Carolina State University; 2008.
36. Sanchez CG, Lozovoi AY, Alavi A. Field-evaporation from first-principles. *Mol Phys*. 2004;102(9-10):1045-1055.
37. Irving DL, Padgett CW, Brenner DW. Coupled molecular dynamics/continuum simulations of joule heating and melting of isolated copper-aluminum asperity contacts. *Modell Simul Mater Sci Eng*. 2009;17(1):-.
38. Liu XY, Xu W, Foiles SM, Adams JB. Atomistic studies of segregation and diffusion in al-cu grain boundaries. *Appl Phys Lett*. 1998;72(13):1578-1580.

3.7 Tables and Figures

Table 3.1 Atomistic system size and dimensions for the gold asperity contacts.

	Sharpening Factor			
	3x	4x	5x	6x
Dimensions (nm)				
[1 1 1]	46.1	46.1	46.1	46.1
[1 -2 1]	52.1	40.2	32.6	27.1
[1 0 -1]	23.7	23.2	20.2	12.7
Contact area (nm ²)	69.7	39.8	25.6	17.2
Number of atoms	3,286,949	2,464,476	1,751,599	915,460

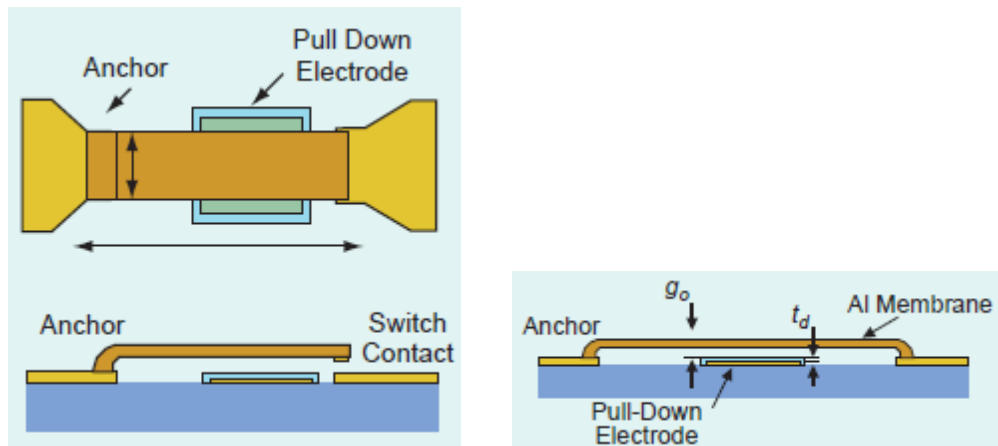


Figure 3.1 Schematic illustration of basic classes of RF MEMS switches. Left: Series-configured resistive; Right: Parallel-configured capacitive. ¹⁸

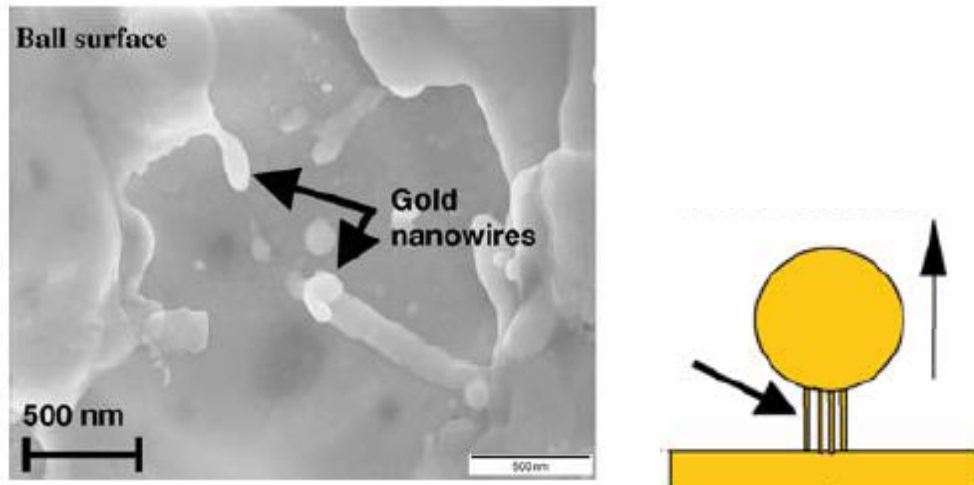


Figure 3.2 Left: SEM image of nanowires on failed gold contact surface; Right: schematic illustration of theoretical mechanism for nanowire formation.²²

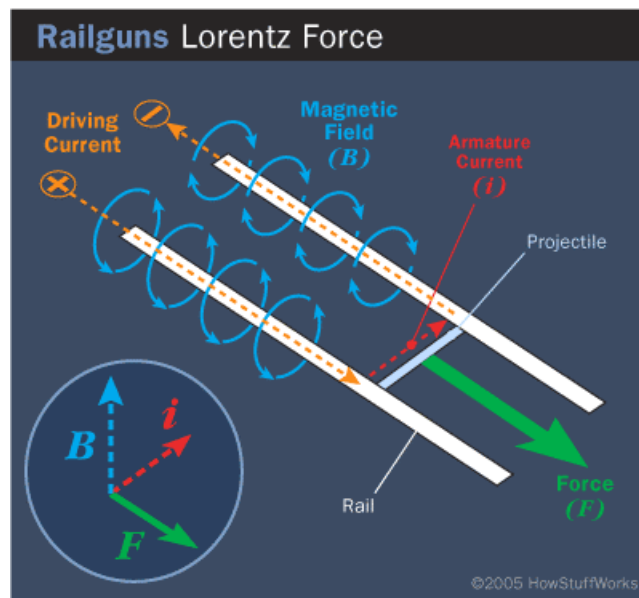
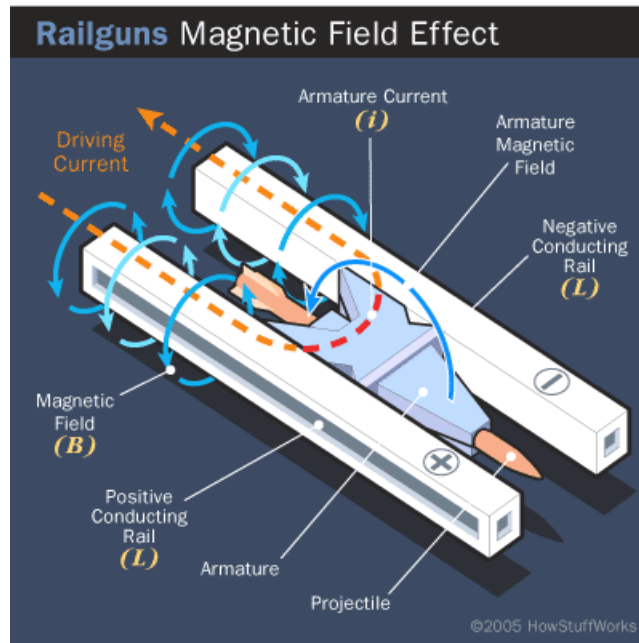


Figure 3.3 Schematic illustration of railgun components (top) and operation (bottom).²⁵

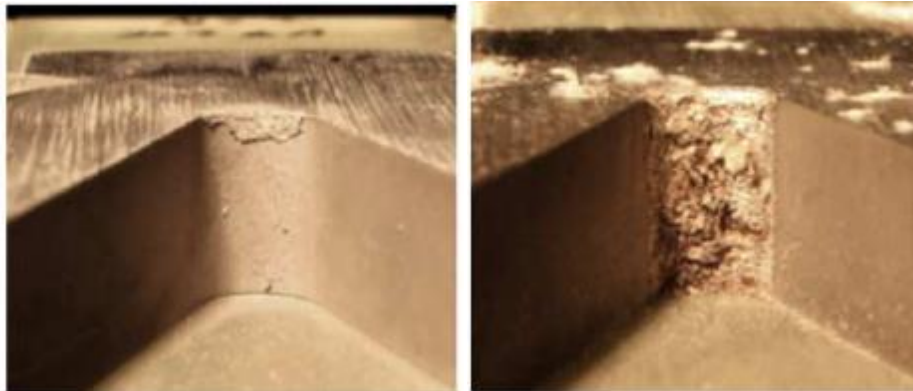
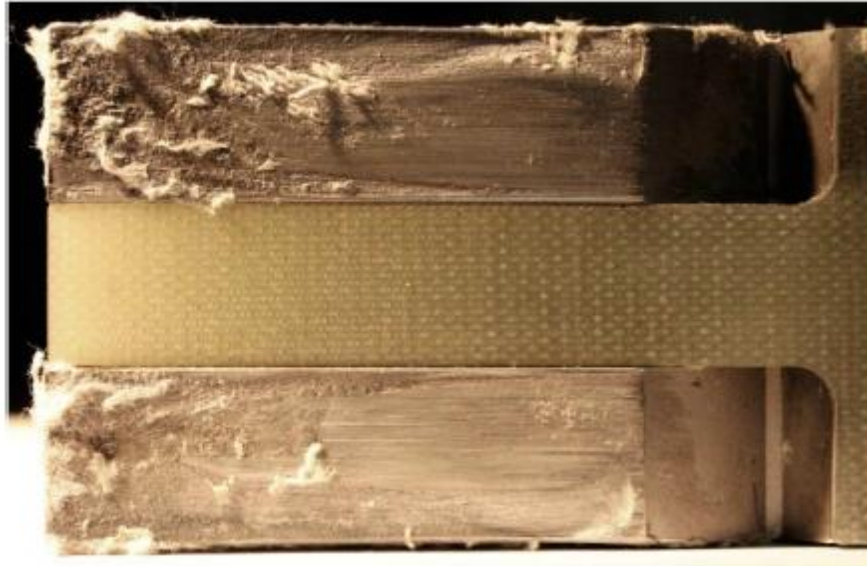
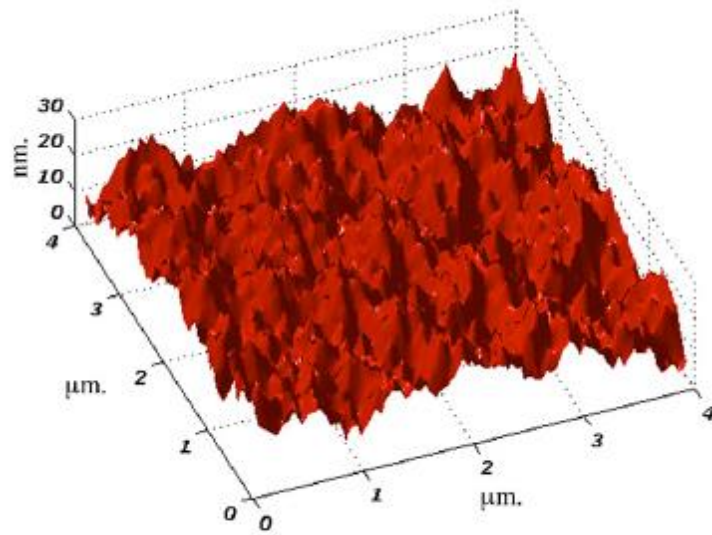


Figure 3.4 Top: Wear on contact surface of armature; Bottom: molten Al accumulated in throat of armature. ²⁸



(a)



(b)



(c)

Figure 3.5 Scale progression of a gold RF MEMS contact surface from (a) fractal model³³ μm -level topography to (b) nm-level single asperity to (c) atomistic tip with \AA -level detail.

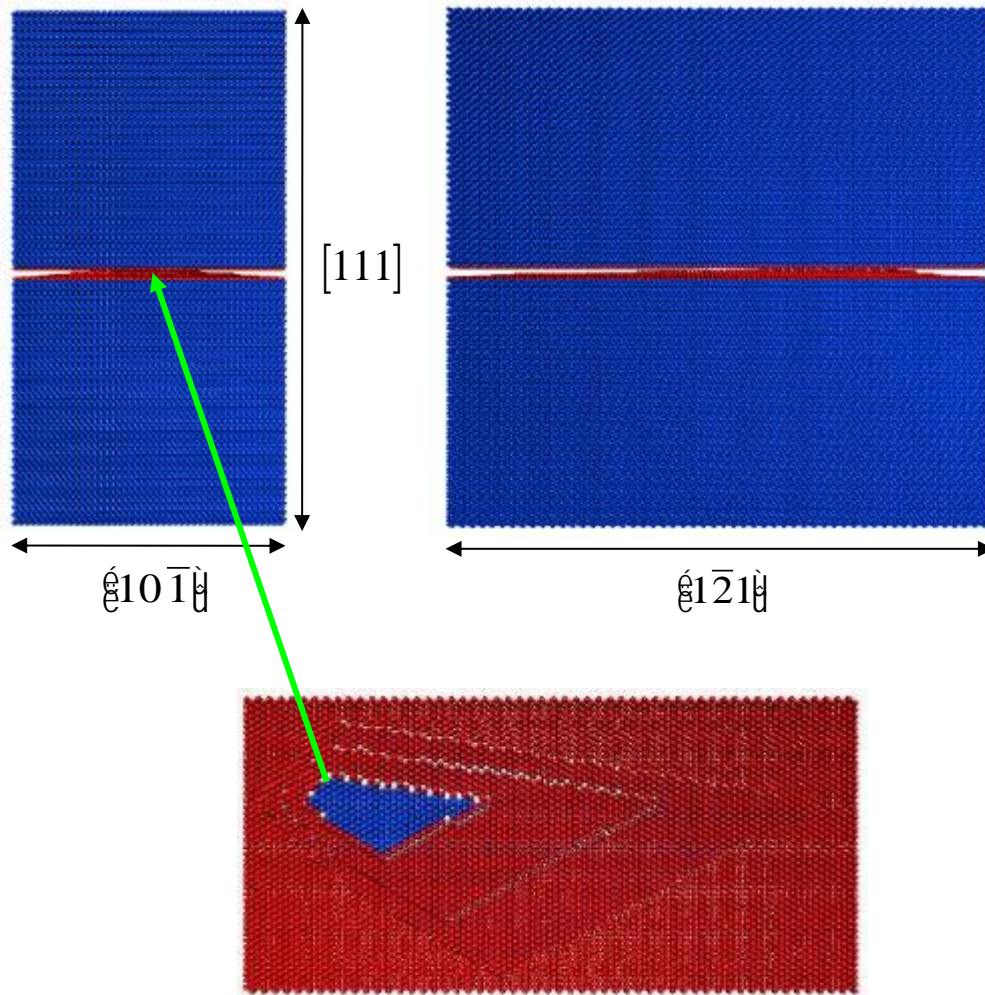


Figure 3.6 Illustration of atomistic system for the gold RF MEMS asperity contact simulations. Atoms colored by local symmetry. Blue indicates bulk, and red represents a surface. Crystallographic directions are labeled.

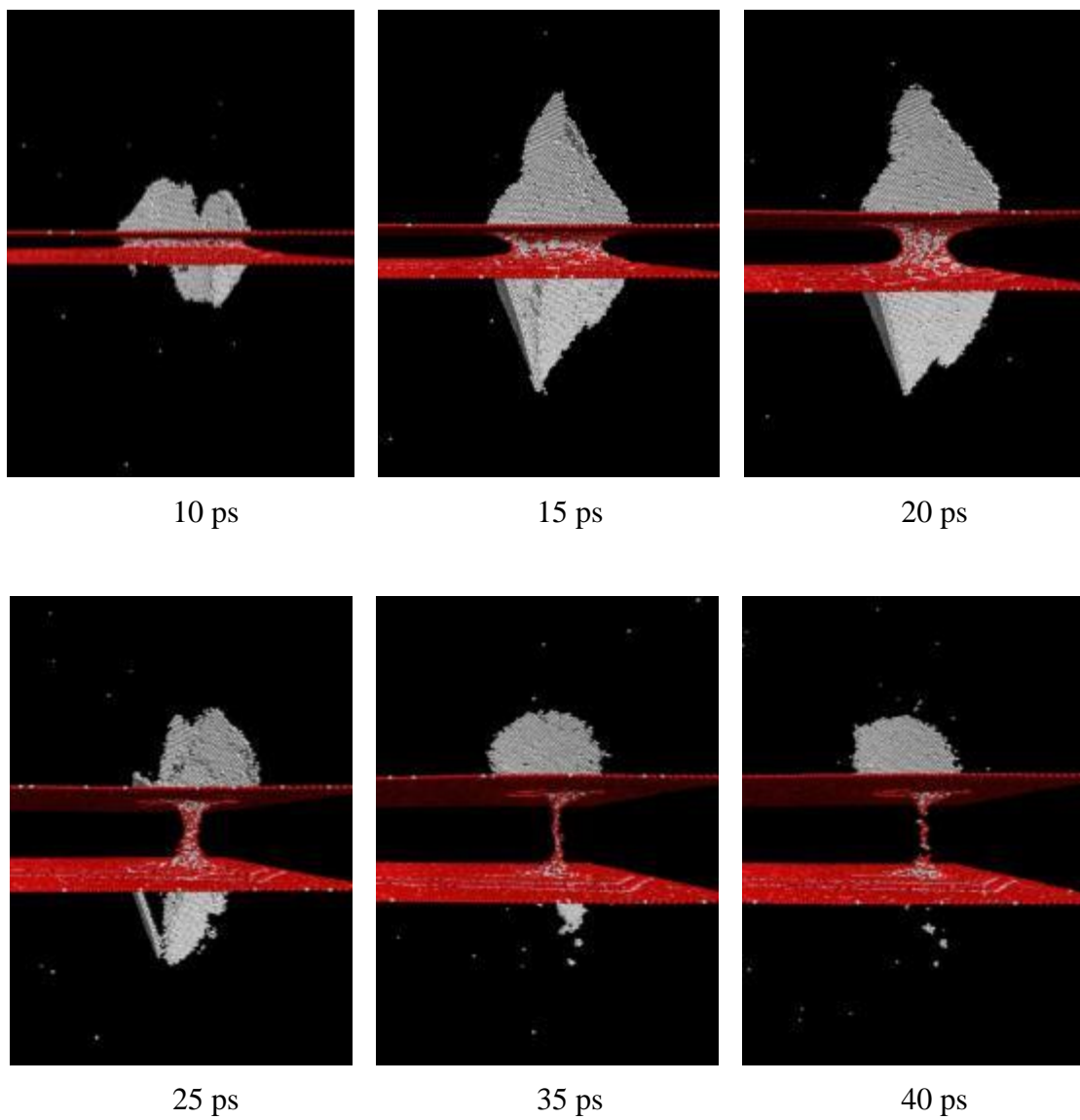


Figure 3.7 Sequential snapshots of a null-voltage simulation of nanowire formation and fracture during pull-apart of a gold asperity contact. Simulation time is noted in picoseconds. Atoms colored by symmetry; bulk atoms removed.

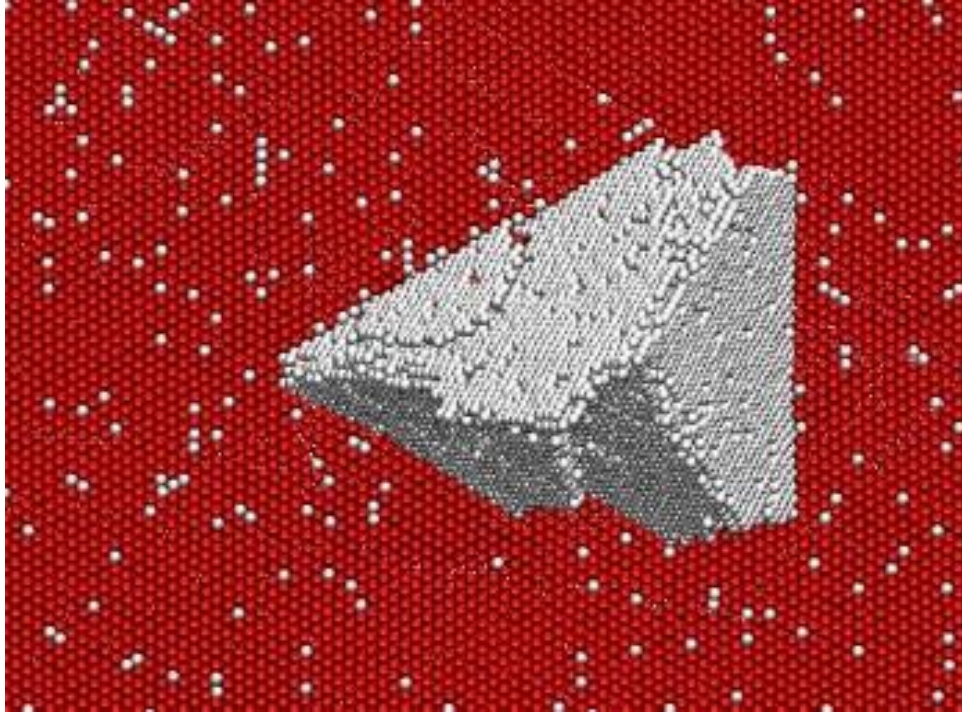


Figure 3.8 Snapshot of Thompson tetrahedron forming under the surface after 15 picoseconds of pull-apart in a gold asperity contact simulation. Atoms colored by local symmetry; bulk atoms removed.

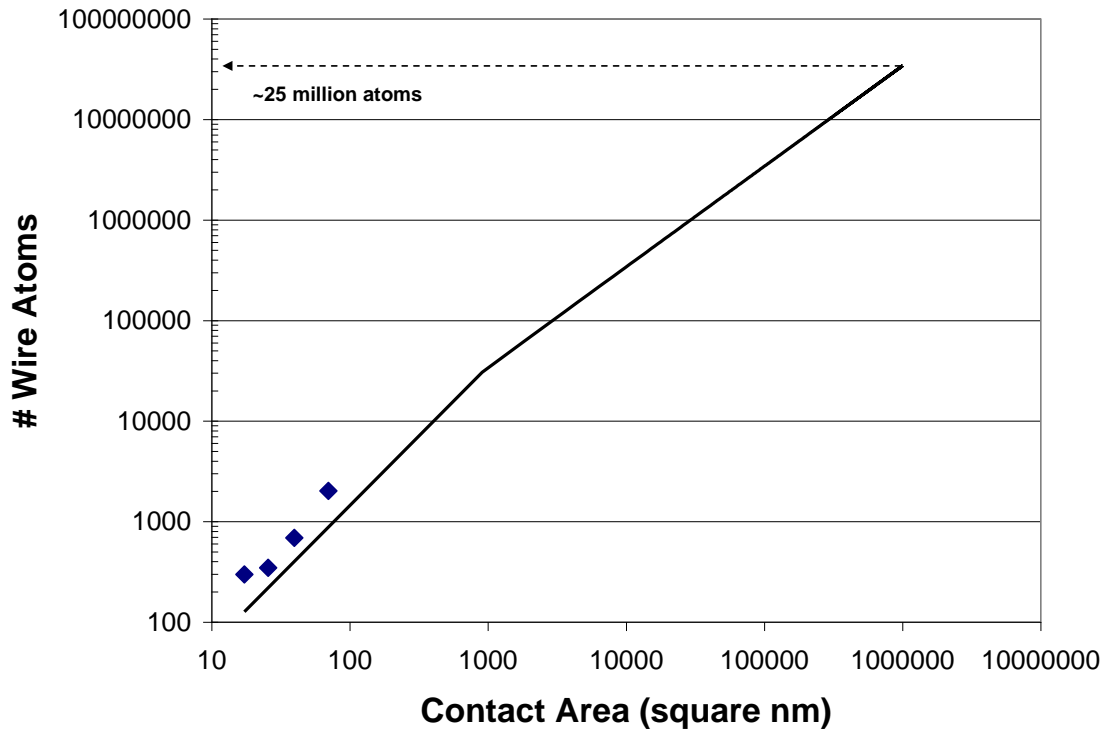


Figure 3.9 Log-log plot of the number of atoms comprising the wire drawn for each initial contact area (blue points) during simulation of pull-apart for gold contacts. A linear regression line fitted to the data is used to extrapolate out to the device-scale contact area of $1 \times 10^6 \text{ nm}^2$ (one square micrometer).

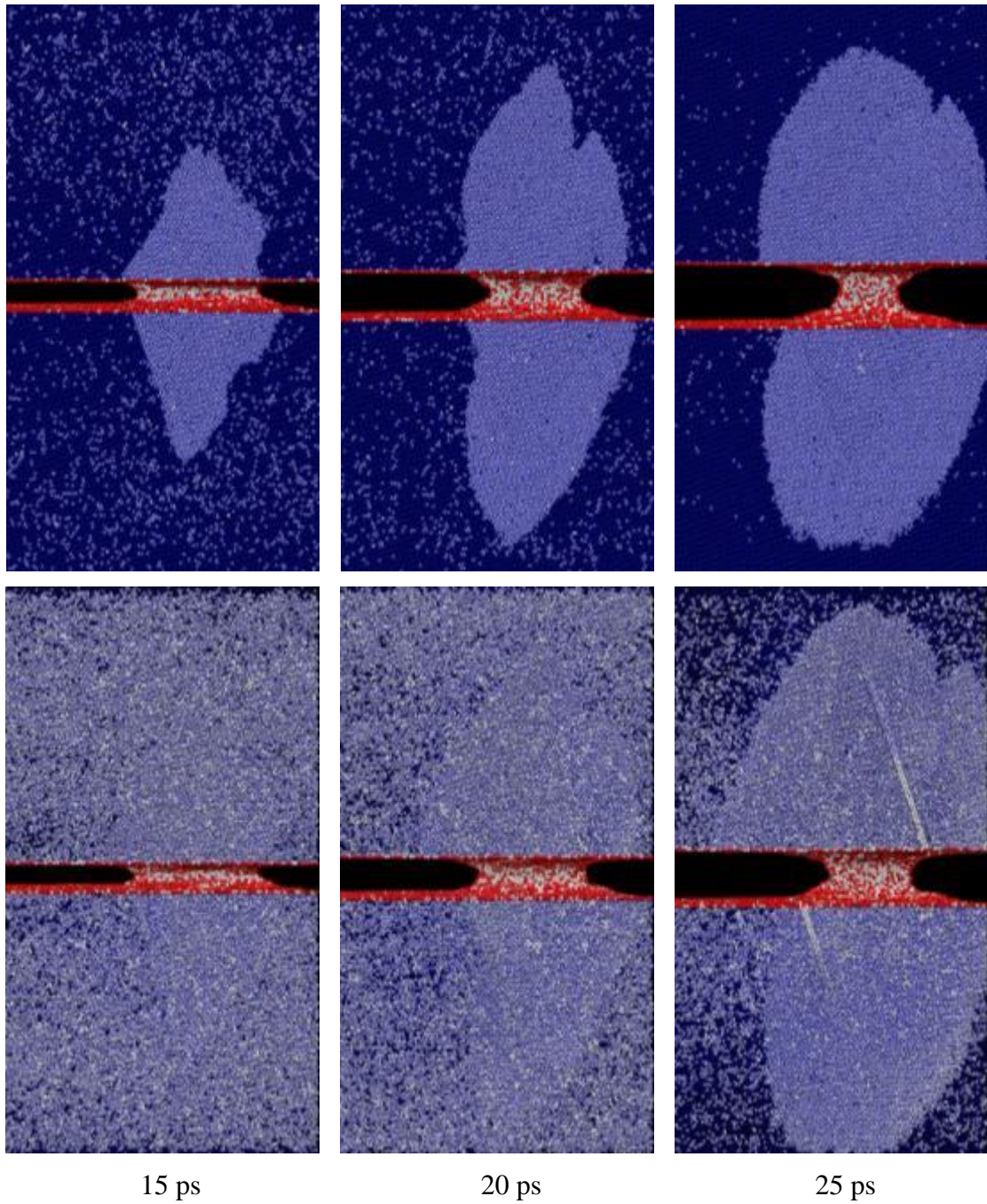


Figure 3.10 Sequential configurations from two gold asperity contact pull-apart simulations. Top row: 0.1 V; bottom row: 0.2 V. Atoms colored by local symmetry; bulk atoms (blue) present, but transparent. The apparent disorder in the 0.2 V simulation is from thermal noise.

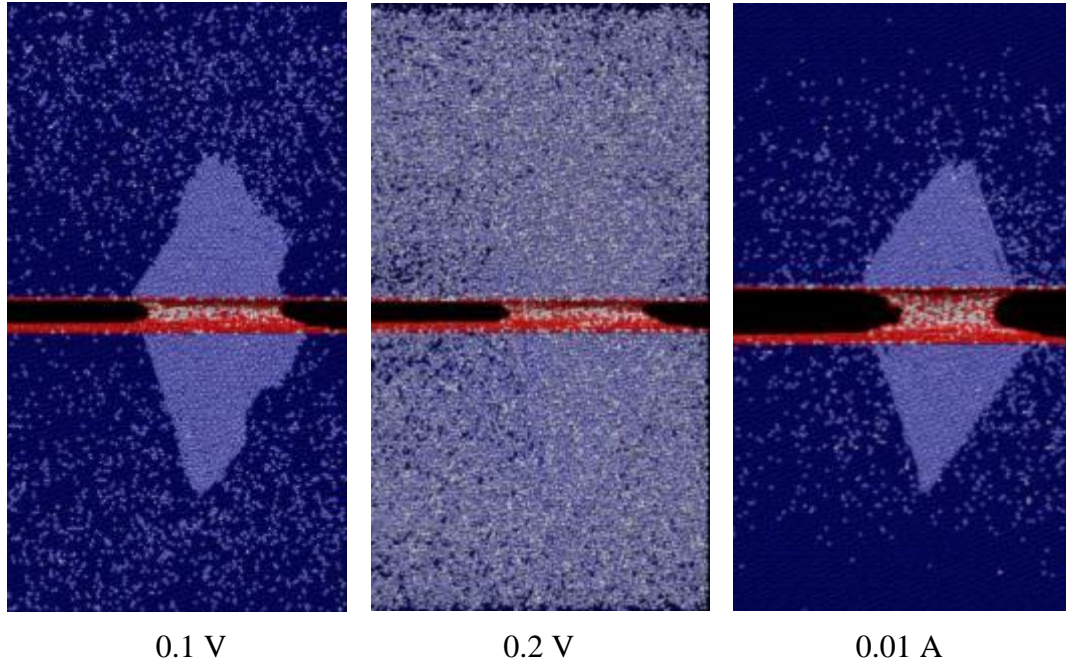


Figure 3.11 Comparison of wire-drawing and deformation after 15 ps of strain for the three gold asperity contact simulations with Joule heating contribution. Atoms colored by local symmetry.

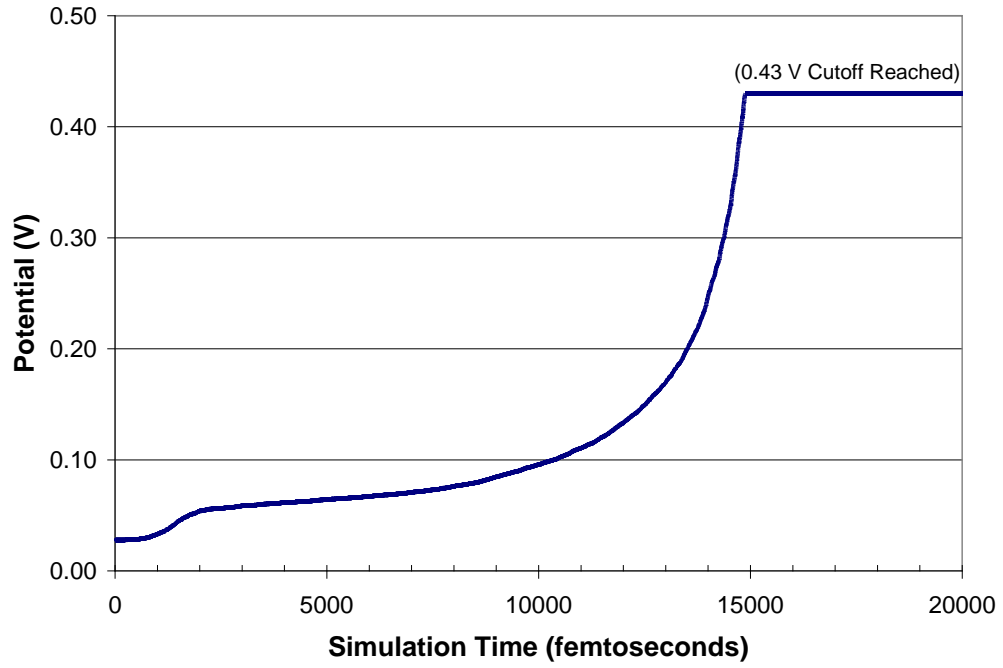


Figure 3.12 Electrical potential drop across contact as a function of time during gold contact pull-apart simulation with constant current of 0.01 A and 0.43 V cutoff.

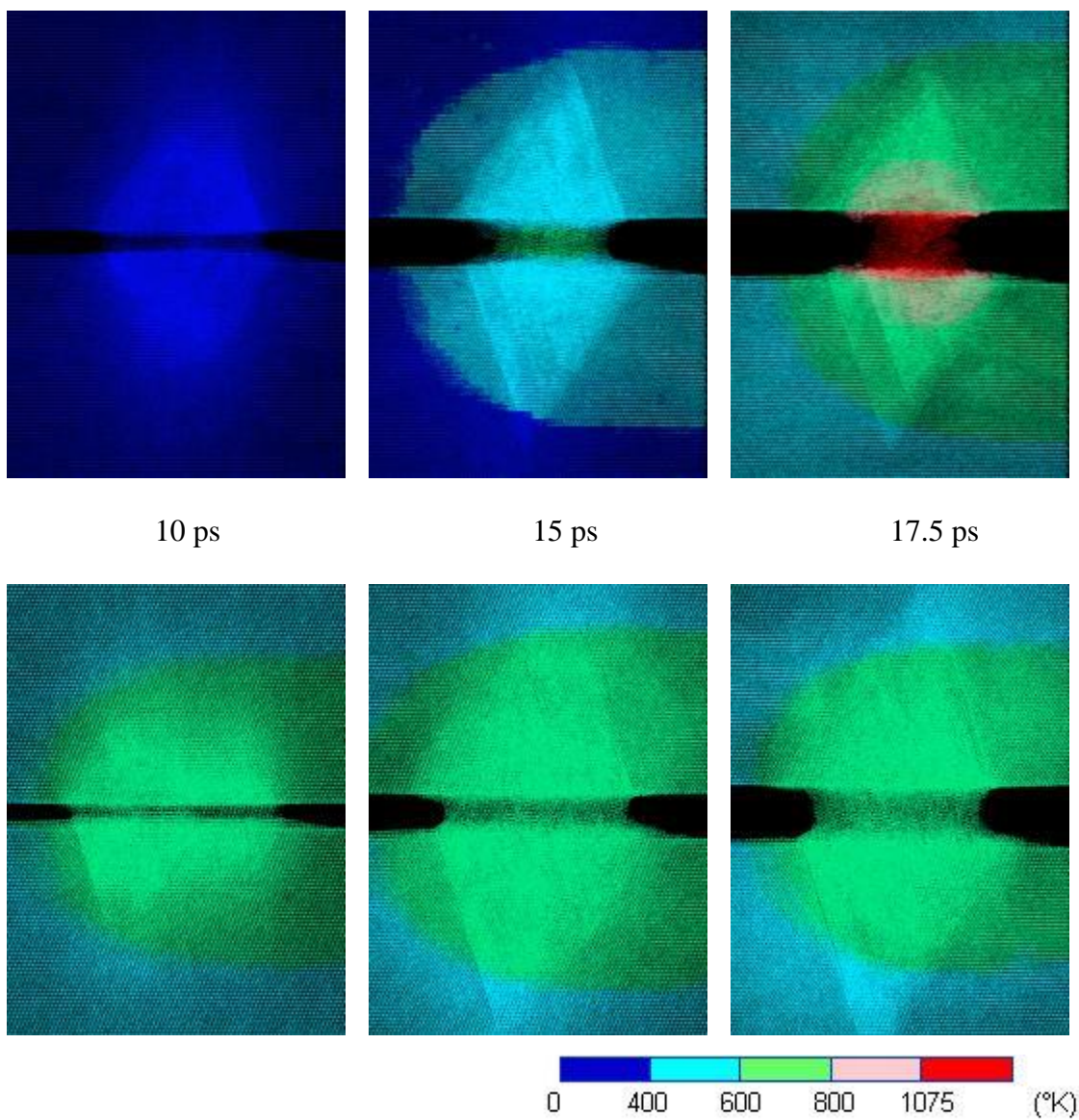


Figure 3.13 Temperature evolution during simulation of gold asperity contact pull-apart. Top: 0.01 A; bottom: 0.2 V. Atoms colored by temperature as indicated in scale.

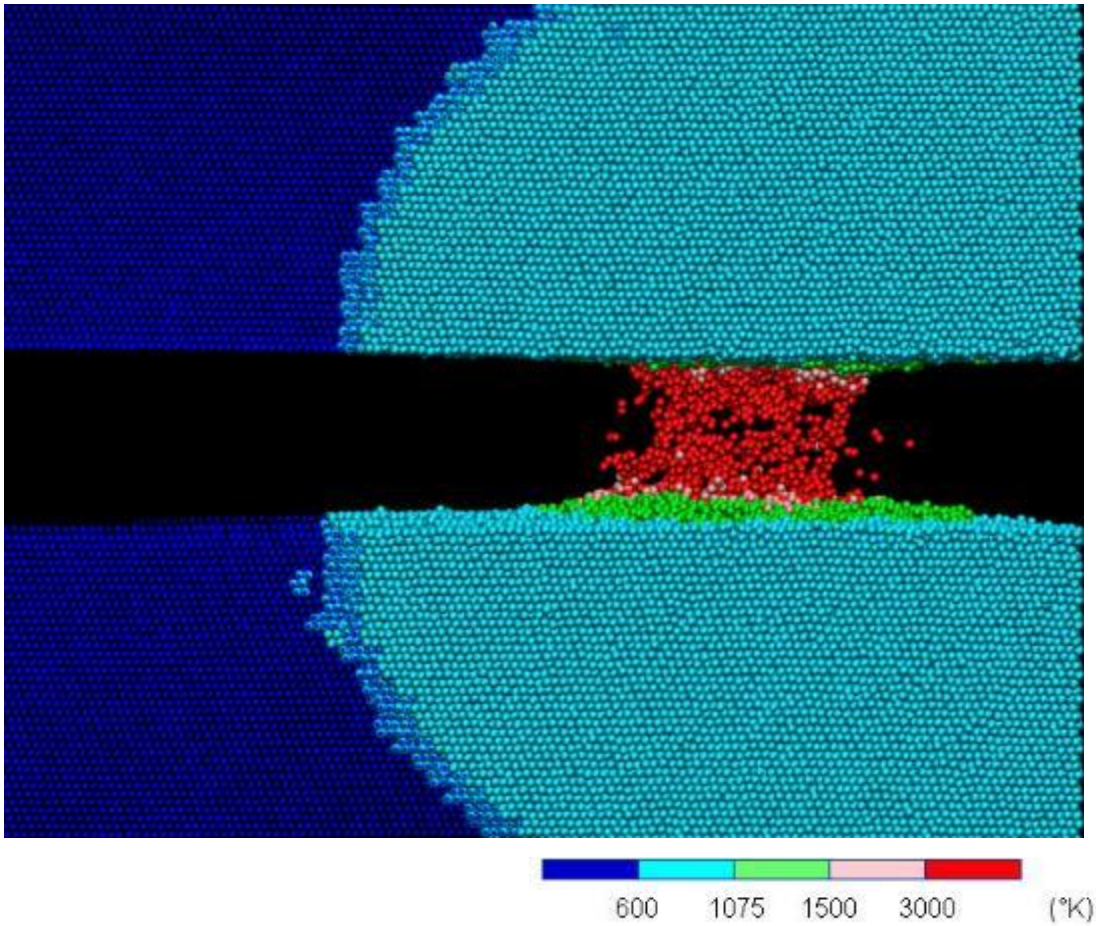


Figure 3.14 Snapshot from simulation of gold asperity contact pull-apart with constant current of 0.01 A after 16 picoseconds with two-volt cutoff employed. Atoms colored by temperature as indicated in scale; all atoms in red are above gold's boiling point of 3239 K.

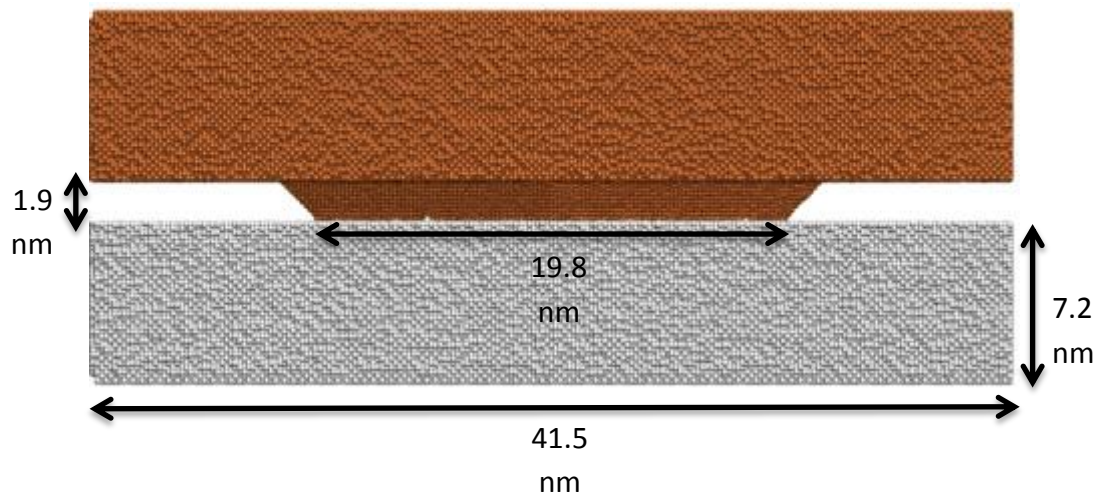


Figure 3.15 Details for atomistic asperity contact used in aluminum/copper sliding simulations.

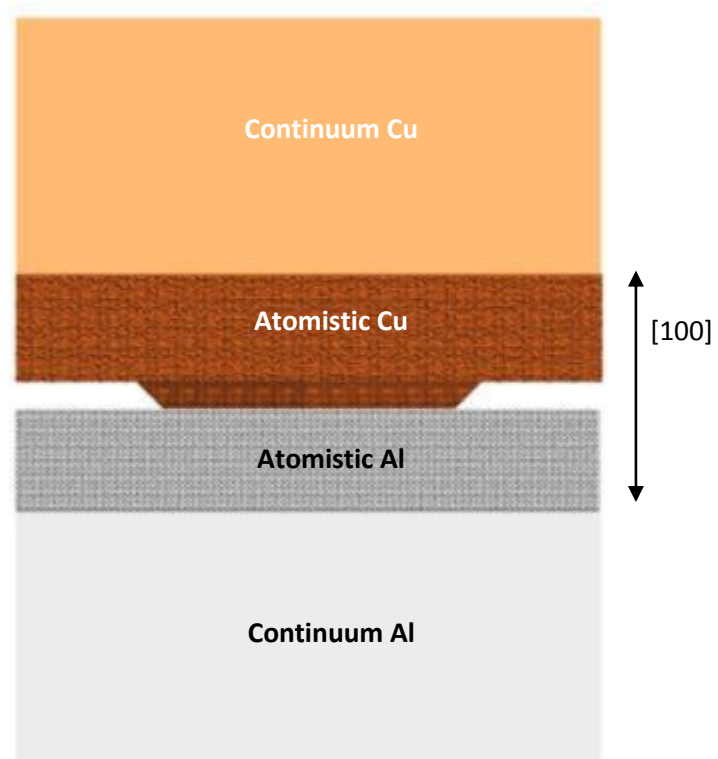


Figure 3.16 Illustration of continuum and atomistic domains for aluminum/copper asperity sliding simulations.

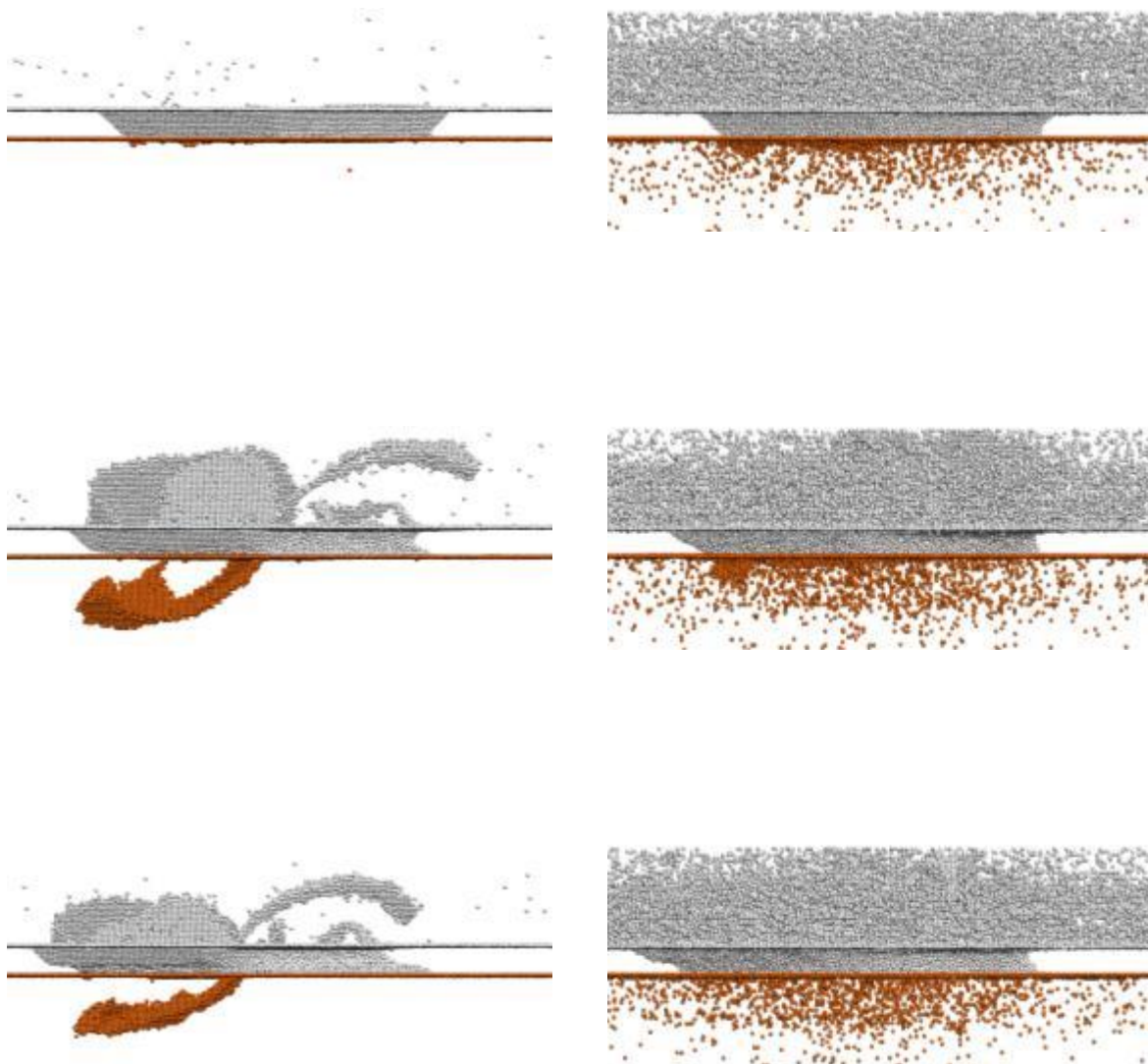


Figure 3.17 Snapshots of Al (light gray) asperity sliding on Cu (orange) substrate with 0 V (left) and 0.2 V (right) taken at 5, 10, and 15 picoseconds (top to bottom, respectively). Atoms with bulk symmetry removed.

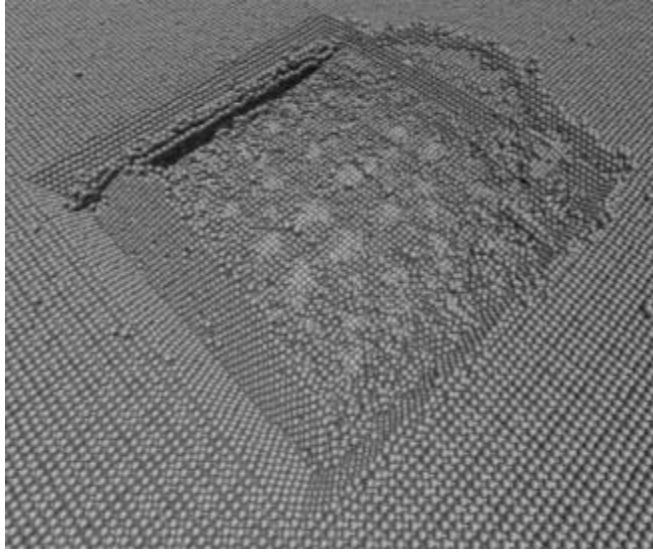


Figure 3.18 Close-up view of stacking faults emanating from the base of an Al asperity inside the Al substrate as the asperity slides on Cu. Atoms with bulk symmetry removed.

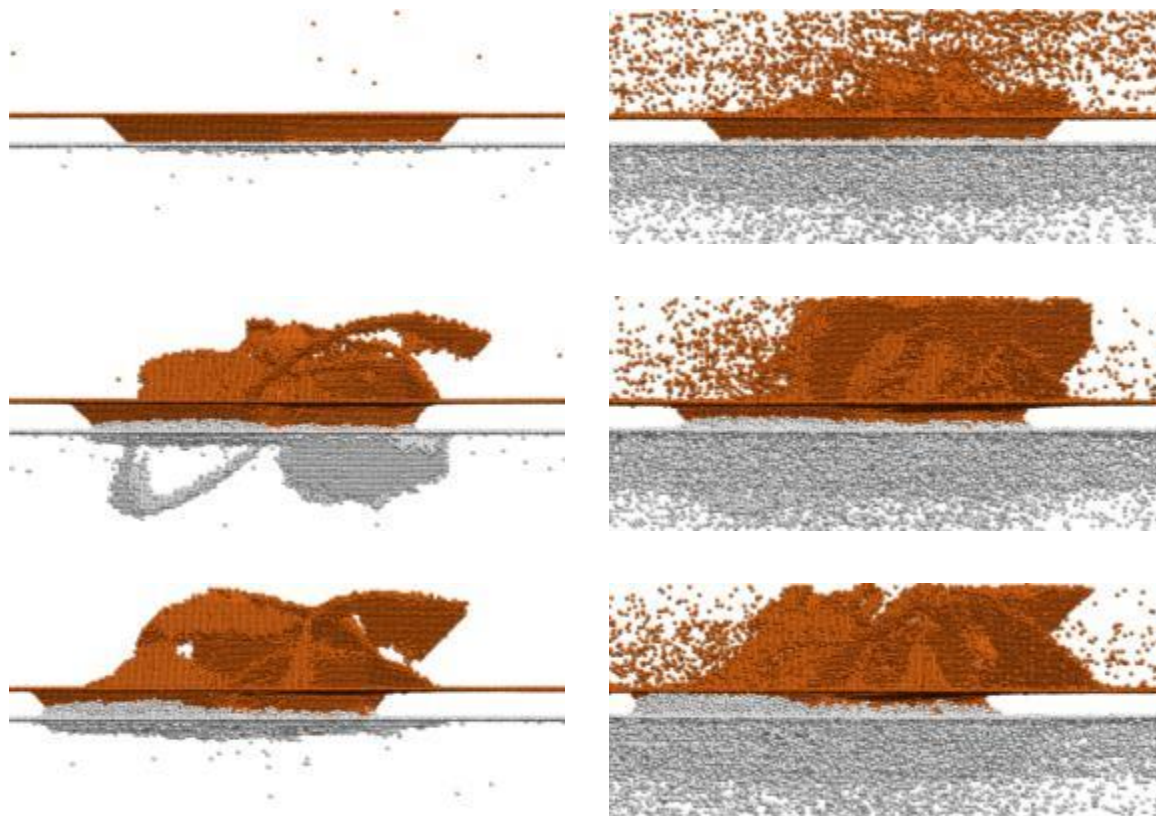


Figure 3.19 Snapshots of Cu (orange) asperity sliding on Al (silver) substrate with 0 V (left) and 0.2 V (right) taken at 5, 10, and 15 picoseconds (top to bottom, respectively). Atoms with bulk symmetry removed.

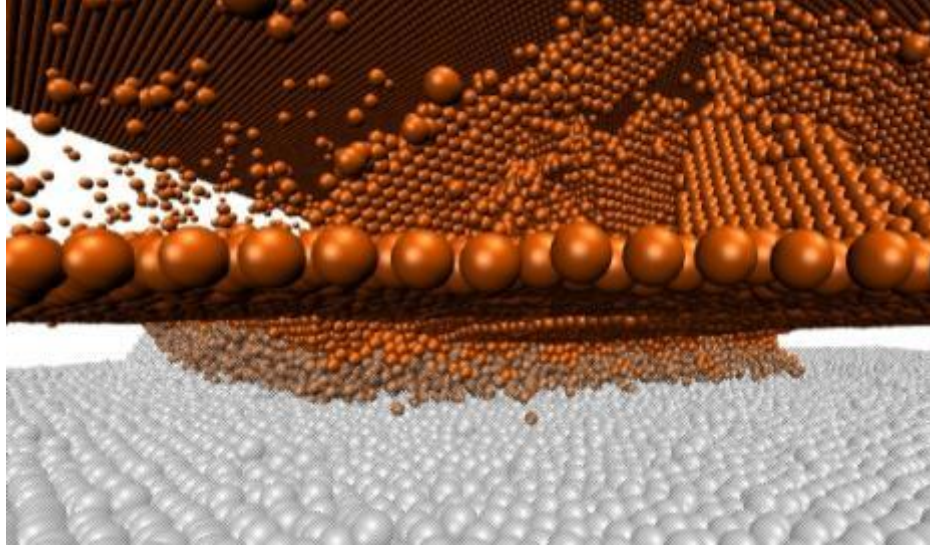


Figure 3.20 Close-up snapshot of Cu (orange) atoms dissolving in Al (light gray) during sliding of a Cu asperity on an Al substrate with 0.2 V applied. Atoms with bulk symmetry removed. Al atoms made transparent.

CHAPTER 4 – MODELING AN F-CENTER WITH THE CHARGE EQUILIBRATION SCHEME

4.1 F-Centers

Color centers, also known as F-centers (“F” standing for Farbe, German for color), are produced when an anion is replaced with an extra electron in an alkyl halide crystal. These charge-neutral defects absorb radiation in the visible spectrum and emit the energy as color. F-centers can be formed in multiple ways¹. Alkyl halide crystals can be subjected to alkali metal rich atmospheres; halide atoms in the crystal bond with the excess alkali atoms, and anionic vacancies are left behind. They can also be formed by X-ray radiation, which produces self-trapped exciton pairs consisting of an anionic vacancy and a halide interstitial². A major engineering application of F-centers is tunable lasers. Such lasers require materials that have strong and broad optical transitions. Alkyl halides fulfill this requirement. Due to the variety of defect types and host materials possible, color centers may have optical transitions which cover wavelengths ranging from 0.3 to 4 μm ³.

Spectroscopy⁴ and Raman scattering⁵ techniques have revealed a wide spectrum of optical absorption energies for F-centers in alkyl halides, ranging from 1.705 eV for RbI to 5.083 eV for LiF, with NaCl F-centers about in the middle at 2.746 eV. The absorption energy depends on the size of the vacancy site; as the lattice parameter increases, absorption energy decreases and the wavelength of emitted light increases, a relationship known as the Mollwo-Ivey Law⁶.

F-centers typically exhibit large Stokes shift (1-2 eV)⁴ resulting from strong electron-phonon coupling. Energy levels of the F-center have been measured using the Stark effect^{7,8}, with the results suggesting the defect to be extremely localized. The charged vacancy has a $1s$ ground state and first excited states of $2s$ and $2p$, leading to F-center defects being described as analogous to a hydrogen-like atom.

Computational techniques have also been used to study F-centers. Some early studies treated F-centers as a single electron trapped in a field of point-charge representations of ions. Gourary and Adrian⁹ and Wood and Korringa¹⁰ used a variational approach starting with a vacancy-centered function to solve the Hartree Fock equation for an F-center vacancy in, respectively, LiF and LiCl. Both found energy levels that agree well with experiment, with Wood and Korringa demonstrating that replacing the wavefunctions of the ions surrounding the vacancy with a Coulomb potential from point charges was an accurate approximation.

Murrell and Tennyson¹¹ were critical of treating the ions surrounding F-centers as point charges and asserted that the agreement with experimental data was simply fortuitous. They sought to obtain the true potential imparted by the surrounding ions of an F-center in LiF using LCAO cluster calculations. However, their more detailed treatment of the ions resulted in less accurate energy level calculations, in particular, underestimation of the $2s \rightarrow 2p$ transition. The proposed culprit for the inaccurate energy levels was inadequate system size due to computational limits; these size limitations preclude modeling contributions from non-nearest neighbors. Kung, Kunz and Vail¹² similarly postulated that absence of

wavefunctions for distant neighbors results in underestimated optical absorption energies, specifically obtaining 3.54 eV versus 5.14 eV experimentally for LiF F-centers.

Density functional theory (DFT) calculations have also been used to study F-centers.

Because DFT approaches the electronic structure problem using electron density rather than electron wavefunctions, it offers the potential for a larger simulation scale than LCAO calculations, although still limited to $\sim 10^3$ atoms depending on computational resources and various approximations in the calculations. However, DFT calculations are known to underestimate bandgap energies; the predicted values for NaCl are 4.5-5.0 eV^{13,14} compared to the experimental value of 8.5 eV¹⁵. This handicap arises from the functionals used in DFT, which essentially separate the energy expression into contributions from classical Coulomb and non-classical electron interactions. The classical component contains an electron-electron repulsion in which every electron is repelled by the total charge in the system. Therefore, each electron will experience repulsion from its own charge, a spurious effect known as a self-interaction error.

The self-interaction error is in principle canceled out by the exact exchange-correlation (XC) functional, but DFT calculations typically use approximation functionals, such as the local density approximation (LDA) or generalized gradient approximation (GGA), which do not completely compensate for the error. This has inspired the development of hybrid functionals that augment the local or semi-local exchange functional with the exact Hartree-Fock exchange functional, reducing the self-interaction energy. Chen et al¹⁶ studied an NaCl F-center using a hybrid functional approach in which a Thomas-Fermi screened exchange operator was combined with the LDA XC interaction, and compared the calculations to those

carried out with LDA only. The hybrid functional was much more accurate in predicting bandgap energy of bulk NaCl (8.47 eV calculated), and produced relaxations in the Na atoms surrounding a Cl vacancy that were not predicted using LDA only. The hybrid functional improved upon the LDA approach in its predictions of optical absorption and emission energies and Stokes and anti-Stokes shifts, although the values were still pretty low compared to experiment.

Fang and de Groot¹⁷ studied the character of the wavefunction in an NaCl crystal using DFT calculations carried out with the local spherical-wave method. The LSW method uses local truncated basis sets which allows for simulation of a 2,744-atom system, larger than the capacity of traditional DFT. They found that the density of states for a crystal containing an F-center was nearly identical to that of the bulk crystal, except for a peak at the vacancy associated with a 1s band for the trapped electron. Madelung energies for Cl atoms neighboring the F-center showed a dip in the electrostatic energy that extended to about 1.2 nm from the vacancy site, while the rest of the crystal preserved its bulk electrostatic energy profile.

Molecular dynamics simulations are quite suitable for modeling defect structures, but must be modified or augmented to describe electronic charge behavior due to the coarse-graining of the electronic degrees of freedom in constructing the interatomic potentials. Landman et al¹⁸ used quantum path-integral molecular dynamics to study alkyl-halide clusters with a vacancy interacting with an excess electron. This method combines an MD treatment of atoms with path-integrals that model an electron's trajectory by integrating over many possible trajectories rather than the classical description of a single one. The

simulations indicated an excess electron to be localized in the vacancy of the NaCl crystal, in agreement with experimental evidence.

An alternative method of analyzing F-centers is proposed here in the form of the Charge Equilibration (QEq) scheme^{19,20}. This approach seeks to calculate optimal charge distributions based upon the equalization of atomic chemical potential driven by electronegativity differences between atoms. A key advantage of the QEq method is its scalability and thus suitability for incorporation into large-scale MD simulations. If QEq is able to mimic the charge distribution properties of an F-center, it could be helpful in modeling systems such as intermetallic compounds, where a standard MD treatment neglects the electrostatic energy contributions.

4.2 Charge Equilibration (QEq) Scheme

The QEq scheme requires a description of the energy of an atom as a function of its charge.

The on-site energy of an atom with respect to charge can be expanded in a Taylor series as²¹:

$$E_i(q_i) = E_{i0} + q_i \left(\frac{\partial E}{\partial q} \right)_{i0} + \frac{1}{2} q_i^2 \left(\frac{\partial^2 E}{\partial q^2} \right)_{i0}. \quad (4.1)$$

When $q_i=-1$, the energy is equivalent to the electron affinity; when $q_i=+1$, the energy is the ionization potential. Using these solutions, the first and second-order derivatives become

$$\left(\frac{\partial E}{\partial q} \right)_{i0} = \frac{1}{2} (IP + EA) = \chi_i^0$$

$$\left(\frac{\partial^2 E}{\partial q^2} \right)_{i0} = IP - EA.$$

The first derivative term is the electronegativity; the second derivative is known as a hardness, or self-Coulomb²², and represents a repulsion between two electrons in a valence orbital. The expression for local atomic energy can thus be expressed as^{19,20}

$$E_i(q_i) = \chi_i^0 q_i + \frac{1}{2} J_i^0 q_i^2 \quad (4.2)$$

where χ_i^0 is the electronegativity of atom i and J_i^0 is the self-Coulomb. The total electrostatic energy can then be described as

$$E_{es} = \sum_i E(q_i) + \frac{1}{2} \sum_{i \neq j} J_{ij} q_i q_j \quad (4.3)$$

with J_{ij} the Coulomb interaction between centers i and j resulting from overlapping charge distributions.

The optimum charge distribution corresponds to the equilibrium at which the atomic chemical potentials, or change in each atom's energy with respect to its charge, are equalized:

$$\chi_A(q_1 \dots q_N) = \chi_A^0 + J_{AA}^0 q_A + \sum_{B \neq A} J_{AB} q_B \quad (4.4)$$

$$\chi_A = \chi_B = \chi_C \dots = \chi_N \quad (4.5)$$

where χ_A is the chemical potential of atom A . Under the constraint that the N atom charges must sum to the total system charge,

$$Q_{total} = \sum_{i=1}^N Q_i \quad (4.6)$$

one is left with N simultaneous equations of the form $CQ = D$ where Q is a vector of all the charges, the components of C are

$$C_{1j} = 1 \quad (4.7)$$

$$C_{ij} = J_{1j} - J_{ij} \quad \text{for } I \geq 2 \quad (4.8)$$

and the components of D are

$$D_1 = Q_{total} \quad (4.9)$$

$$D_i = \chi_i^0 - \chi_1^0 \quad \text{for } I \geq 2 \quad (4.10)$$

Rappe and Goddard proposed a method for constraining the charge solutions within a prescribed range. For instance, the charge on a lithium atom is required to be greater than -7, but less than +1. To enforce this constraint, the charge solutions obtained from Equations 4.7 – 4.10 are compared to the permitted range. A charge falling outside the range is set to the boundary limit. The equations are then re-solved for $N - p$ atoms, where p is the number of atoms for which charge has been fixed. The components of D from Equations 4.9 and 4.10 then become

$$D_1 = Q_{total} - \sum_{j=1}^p Q_j \quad (4.11)$$

$$D_i = \chi_i^{0F} - \chi_1^{0F} \quad \text{for } I \geq 2 \quad (4.12)$$

where

$$\chi_i^{0F} = \chi_i^0 - \sum_{j=1}^p J_{ij} Q_j \quad \text{for } I \geq 2 \quad (4.13)$$

and the charges on the non-fixed atoms are then solved. While charges for the NaCl crystals in the present work do not move outside of reasonable boundaries, this reduced equation methodology later will be shown to be important for modeling the extra electron of an f-center.

The values for χ_i^0 and J_i^0 are derived from atomic data²³; the values of χ_i^0 for Na and Cl are 2.853 and 8.564, respectively, and the values of J_i^0 are 4.592 and 9.892, respectively

for Na and Cl. The form for the two-center J_{ij} interaction requires an assumption about the charge distributions for the atoms. Slater¹⁹ and Gaussian orbitals²⁰ have been used, but Oda and Hirono²⁴ showed the charge equilibration scheme to work well using less computationally intensive empirical approximations of the two-center integrals. The present work utilizes the form for J_{ij} that Oda and Hirono found to give the most accurate results, the DasGupta-Huzinaga²⁵ (DH) equation

$$J_{ij} = \frac{1}{R_{ij} + \frac{1}{\frac{J_{ii} e^{0.4 R_{ij}}}{2} + \frac{J_{jj} e^{0.4 R_{ij}}}{2}}} \quad (4.14)$$

where R_{ij} is the distance between the atoms.

The matrices used to solve the simultaneous potential energy equations are implemented as described above, apart from one small difference. To reproduce bulk Na/Cl charges close to the +/- 0.828 e obtained from the Bader method²⁶, the C matrix terms for $i > l$ are scaled by a constant factor of 0.48.

4.3 Convergence of lattice sums

The QEq method requires summation of charge terms (e.g. Equation 4.4). These summations are notoriously difficult to converge. A simple illustration of this involves computing the Madelung constant for electrostatic energy. The electrical potential felt by an ion due to the charges of all other ions in the crystal can be calculated as

$$V_i = \frac{e}{4\pi\epsilon_0} \sum_{i \neq j} \frac{z_j}{r_{ij}} \quad (4.15)$$

where r_{ij} is the distance between the ions and z_j is the number of charges on ion j . A

Madelung constant can be extracted from this expression as

$$V_i = \frac{e}{4\pi\epsilon_0 r_0} \sum_{i \neq j} \frac{z_j}{r_{ij}/r_0} = \frac{e}{4\pi\epsilon_0 r_0} M_i \quad (4.16)$$

where the M_i is the Madelung constant,

$$M_i = \sum_j \frac{z_j}{r_{ij}/r_0} \quad (4.17)$$

and r_0 is the nearest neighbor distance, or one-half the lattice parameter.

Consider the case of the NaCl lattice illustrated in Figure 4.1. The Madelung constant of the center Cl atom can be broken down into contributions from sequentially more distant sets of neighbors. The first set of neighbors, the 6 closest Na atoms at distances $\langle 001 \rangle$ relative to the Cl atom, contribute +6 units of charge to the energy (for simplicity, we will assume the Na and Cl atoms have +/- 1q of charge). The next set of neighbors, 12 Cl atoms at relative distances $\langle 110 \rangle$, contribute $12/\sqrt{2}$ units of charge. In an infinite bulk seeded from the NaCl lattice in Figure 4.1, the Madelung constant will take the form of the series:

$$M = 6 - \frac{12}{\sqrt{2}} + \frac{8}{\sqrt{3}} - \frac{6}{2} + \frac{24}{\sqrt{5}} + \dots = -1.74756 \quad (4.18)$$

However, this series is very slow to converge. Figure 4.2 illustrates the system size dependence for a bulk Madelung constant computed for a NaCl lattice seeded by the $\text{Na}_{14}\text{Cl}_{13}$ cube. Even with nearly 3.5 million atoms, the Madelung constant is not fully converged to the accepted value of 1.74756. Given the matrix operations required to solve Equations 4.7 – 4.10, simulations of $\text{Na}_{14}\text{Cl}_{13}$ -seeded lattices that obtain convergent atomic charges using the QEq method will impose a considerable computational burden.

There have been many solutions proposed for this convergence problem. One of the earliest, the Ewald method²⁷, assumes two components of the electrostatic energy: a short-range component, which converges at very short distances from the atom while diverging at long distances, and a long-range component, which converges at long distances but diverges near the atom. The energy summations are carried out separately to produce two convergent series. However, the Ewald method uses various error functions that can be computationally demanding to implement²⁸.

A simpler methodology for getting convergent lattice sums is proposed by Harrison²⁹. Summing charges in sequentially larger spheres, as in Equation 4.18, is not rapidly convergent because the summation is occurring over non-charge-neutral sub-sections. As the sphere over which charge is calculated expands outward, its charge fluctuates, de-stabilizing the total summation. Harrison's solution was to apply a thin shell of compensating charge at the edge of each sequential sphere. Using this method, the Madelung constant of a rock salt structure could be computed using $\sim 1/200^{\text{th}}$ of the volume required without the compensating charge.

Baker and Baker³⁰ note that charge corrections are only necessary because the expanding volumes over which charges are summed are not charge-neutral. By extension, if the atomic volume is discretized into charge-neutral sub-entities, convergent summation of charge can be accomplished without correction. Equivalently, if the entire system is constructed using a charge-neutral seed, charge summations over the whole lattice will thus be convergent. Baker and Baker demonstrate that the calculated Madelung constant of a Na atom in a Na_4Cl_4 cube with just 8 atoms is within $\sim 0.2\%$ of the accepted value.

Using the 8-atom Na_4Cl_4 cube, illustrated in Figure 4.3, as the repeat structure for NaCl crystals, one can see the improvement in convergence for the Madelung constant in Figure 4.4. The value computed for 216 atoms is within 0.03% of the accepted value; by 1,000 atoms, the error is on the order of one-thousandth of a percent. The calculations that follow use a system with 1,728 atoms. This cube has 12 atoms per side (6 Na, 6 Cl) for side length 3.10 nm.

4.4 Charge distribution with an anionic vacancy

The first sets of calculations are for the case of an anionic vacancy produced by removing a chlorine atom from a sodium chloride crystal. The removal of the chlorine atom results in a net charge of +1; however, f-center defects are charge-neutral due to the localized electron that replaces the ion. The charge constraint in Equation 4.9, used to solve the set of simultaneous equations, is thus set to zero for a meaningful comparison to prior f-center calculations.

Figure 4.5 reports the distribution of charges for sodium and chlorine atoms for the ideal bulk NaCl crystal (blue) and the crystal with the vacancy. Charges in the figure are averages by radial distance from the location of the removed chlorine atom. The levels of charge for both sodium and chlorine dip markedly in the vicinity of the vacancy. The six sodium atoms comprising the nearest neighbors of the missing chlorine atom have the largest reduction in charge. For both sodium and chlorine, the disturbance in charge stretches between 1.0 and 1.5 nm radially outward from the vacancy, where the charges then level off to bulk values (± 0.832).

Fang and de Groot¹⁷ demonstrated the effect of an F-center on electrostatic energy, showing a valley in Madelung energy about 12 angstroms (1.2 nm) in radius with a pronounced dip to 0.19 eV less than bulk for the chlorine atoms closest to the defect. Inside the potential valley, a large peak in electrostatic energy (~0.55 eV higher than bulk) appears due to the presence of the extremely localized charge. Figure 4.6 reproduces this analysis for the QEq model, illustrating the electrostatic energy of the chlorine atoms using the solved charges. Because the defect system in this case contains an anionic vacancy without a corresponding localized charge, there is no energy value for the defect site. The electrostatic energy dip at the nearest chlorine atoms is about 2.0 eV lower than bulk, an order of magnitude higher than the first principles result. In addition, the radius of the potential well is more than 2.0 nm, again exceeding the previous computational evidence. It is clear that the localized charge in the vacancy has an important influence on the overall energetics of the system.

4.5 Charge distribution with an f-center

The next step is to incorporate a charge at the site of the vacancy. But an f-center charge cannot be included in the set of electronegativity equalization equations used to solve charges. The prior evidence on f-centers indicates the charge is extremely localized; however, the QEq treats the whole system as a conductor and redistributes any charge in the system accordingly. A better approach is to exclude the f-center's charge from the QEq but include the influence of the fixed charge on the remaining atoms.

The framework outlined above for restricting charges within a prescribed range provides a way to implement an f-center charge. After fixing the charge at the vacancy site, the other charges can then be solved using Equations 4.11 – 4.13, which results in a total charge neutral system. Charge transfer to and from the f-center is prevented, but the effect of its charge is transmitted to the other atoms through the modified electronegativity parameter. Figure 4.7 reports the average charges on chlorine atoms surrounding the defect with different values of charge assumed for the f-center. Fixing the charge to zero reproduces the charge distribution obtained in the anionic vacancy calculation. Using the bulk Cl charge (-0.832, shown in purple) essentially reproduces bulk-like conditions for the surrounding atoms, resulting in a flat charge distribution. This intuitively follows from the fact that the QEq doesn't "know" the f-center isn't an atom; it only "sees" the f-center's charge. A charge between zero and the bulk results in a dip in neighboring chlorine charges, but the dip is not as pronounced as for the case of a vacancy. Fang and de Groot¹⁷ obtained a charge of about -0.6 e at the location of the f-center; using this charge in our model introduces only a slight disturbance to the surrounding charge.

The electrostatic energy spatial profile for the defect crystal is illustrated in Figure 4.8 for the f-center fixed at -0.6 e ; the energy data from [17] are included for comparison. To aid the comparison, the Fang and de Groot data have been scaled by a factor of 0.945 to account for the lower bulk energies in the first principles calculation. The energy potential valley is now much shallower than in Figure 4.6. The chlorine atoms closest to the f-center have Madelung energies that are on average about 0.5 eV lower than bulk; while still overstating the dip observed in the first principles calculation, this is much closer than for the case of the

uncharged vacancy. The width of the potential well is also narrower than in Figure 4.6. Electrostatic energies level off to bulk values between 1.2 and 1.4 nm away from the f-center, compared to over 2.0 nm. This model thus seems capable of mimicking some of the characteristics of the f-center's effect on local energy even if the absolute dip in energy is overstated.

Figure 4.9 illustrates the total Madelung energy and self-energy, summed for all ions within 1.5 nanometers of the f-center, as a function of charge at the f-center. Each atom's Madelung energy is the sum of Coulombic potentials from all other ion sites (Equation 4.15); self-energy for each atom is computed using the second-order Taylor expansion of energy with respect to on-site charge (Equation 4.2). The crystal's self-energy in the vicinity of the defect has positive concavity with a local minimum around $-0.4 e$, while the total local Madelung energy is increasing with charge. The sum of the two energy components, $\Sigma(\text{Madelung}) + \Sigma(\text{Self})$, reported in the bottom panel of Figure 4.9, is minimized for the surrounding ions when the f-center charge is approximately $-0.6 e$. In other words, the self-energy terms drive the QEq model to favor an f-center charge that agrees well with the first principles calculation.

4.6 Conclusions

The purpose of this work was to study the capability of the charge equilibration method in reproducing some of the basic characteristics of f-centers in alkyl halides. These properties, observed both experimentally and computationally, include: 1) a nearly-bulk charge centered

at the vacancy; 2) an electrostatic energy valley surrounding the f-center, and; 3) disturbance of surrounding charges that is restricted to within a few lattice positions of the defect.

A limitation of the QEq method is that it treats the entire atomic system as a single conductor, allowing charge to flow freely across all atoms. As such, a localized charge cannot be directly input into the model. An “f-center” modeled as a charge-neutral anionic vacancy results in charge distributions that produce a dip in electrostatic energy that is unrealistically large compared to a true f-center. A better approach is to include the f-center charge indirectly by incorporating the fixed charge into the equations used to equalize electronegativity of the atomic charges. A model using a fixed f-center charge based on first principles enables the QEq to mimic the electrostatic energy characteristics of the f-center to a reasonable extent.

Further opportunities for this methodology could include additional point defect simulations. In addition to f-centers, alkyl halides can contain h-centers, or halide interstitials. Formed during irradiation, h-centers consist of a neutral halogen atom that forms a chemical bond with the nearest halogen ion to produce a dumbbell-shaped X_2^- molecule, where X is the halide species.

DFT calculations of h-centers have provided evidence that the charge concentration around the defect is lattice orientation dependent. An X_2^- molecule formed along the $\langle 111 \rangle$ direction has a higher electron concentration between the two atoms than the same molecule formed along the $\langle 110 \rangle$ direction³¹. It would be interesting to simulate this with the QEq model. In this system, two distinct fixed charges would be assumed at the defect site, with the interstitial location being varied to represent the differing bond orientations. One

question for this model would be whether the defect should be treated as non-reactive (no self-energy term, as was the case for the f-center simulation), or whether charge can be transferred to and from the h-center.

On a larger scale, the QEq methodology could be incorporated into MD simulations of intermetallic compounds, such as the omega phase formed in aluminum-copper alloys. The omega phase is a hexagonal, disk-like Al_2Cu precipitate produced during the aging of Al-Cu, and imparts high strength and toughness to the alloy. Using the QEq method to assign charges to the Al-Cu interfaces and incorporating the resulting electrostatic energies into interatomic potential could help capture the influence of Coulombic interactions on the physical properties of aluminum-copper alloys.

4.7 References

1. ITOH N, TANIMURA K. Formation of interstitial-vacancy pairs by electronic excitation in pure ionic-crystals. *J Phys Chem Solids*. 1990;51(7):717-735. doi: 10.1016/0022-3697(90)90145-6.
2. WILLIAMS R, SONG K. The self-trapped exciton. *J Phys Chem Solids*. 1990;51(7):679-716. doi: 10.1016/0022-3697(90)90144-5.
3. GELLERMANN W. Color center lasers. *J Phys Chem Solids*. 1991;52(1):249-297. doi: 10.1016/0022-3697(91)90068-B.
4. Popov AI, Kotomin EA, Maier J. Basic properties of the F-type centers in halides, oxides and perovskites. *Nucl Instrum Methods Phys Res Sect B-Beam Interact Mater Atoms*. 2010;268(19):3084-3089. doi: 10.1016/j.nimb.2010.05.053.
5. PERREGAU.A, ASCARELL.G. Piezo-optic study of F-center in alkali-halides - evidence for structure in F band of Kc1,kbr, and nacl. *Phys Rev B*. 1974;10(4):1683-1698. doi: 10.1103/PhysRevB.10.1683.
6. IVEY H. Correction. *Physical Review*. 1947;72(9):873-873. doi: 10.1103/PhysRev.72.873.
7. Grassano UM, Margaritondo G, Rosei R. Unrelaxed 2S state of the F center in alkali halides studied by the stark effect. *Physical Review B-Solid State*. 1970;2(8):3319-3322. doi: 10.1103/PhysRevB.2.3319.

8. BOGAN L, FITCHEN D. Stark effects in F-center emission. *Physical Review B*. 1970;1(10):4122-&. doi: 10.1103/PhysRevB.1.4122.
9. GOURARY B, ADRIAN F. Approximate wave functions for the F-center, and their application to the electron spin resonance problem. *Physical Review*. 1957;105(4):1180-1192. doi: 10.1103/PhysRev.105.1180.
10. WOOD R, KORRINGA J. Electronic structure of F center in licl. *Physical Review*. 1961;123(4):1138-&. doi: 10.1103/PhysRev.123.1138.
11. MURRELL J, TENNYSON J. Molecular scf calculations on the F-center of lif. *Chem Phys Lett*. 1980;69(2):212-215. doi: 10.1016/0009-2614(80)85047-0.
12. KUNG A, KUNZ A, VAIL J. Unrestricted-hartree-fock cluster-analysis of F-center and fa-center in some alkali-halides. *Phys Rev B*. 1982;26(6):3352-3360. doi: 10.1103/PhysRevB.26.3352.
13. Li B, Michaelides A, Scheffler M. Density functional theory study of flat and stepped NaCl(001). *Phys Rev B*. 2007;76(7):075401. doi: 10.1103/PhysRevB.76.075401.
14. Chen W, Tegenkamp C, Pfnuer H, Bredow T. Tailoring band gaps of insulators by adsorption at surface defects: Benzoic acids on NaCl surfaces. *Phys Rev B*. 2009;79(23):235419. doi: 10.1103/PhysRevB.79.235419.

15. POOLE R, LIESEGANG J, LECKEY R, JENKIN J. Electronic band-structure of alkali-halides .2. critical survey of theoretical calculations. *Phys Rev B*. 1975;11(12):5190-5196. doi: 10.1103/PhysRevB.11.5190.
16. Chen W, Tegenkamp C, Pfnuer H, Bredow T. Color centers in NaCl by hybrid functionals. *Phys Rev B*. 2010;82(10):104106. doi: 10.1103/PhysRevB.82.104106.
17. Fang CM, De Groot RA. Wavefunction character of the F-center in table salt. *J Phys - Condes Matter*. 2008;20(7):075219. doi: 10.1088/0953-8984/20/7/075219.
18. LANDMAN U, SCHARF D, JORTNER J. Electron localization in alkali-halide clusters. *Phys Rev Lett*. 1985;54(16):1860-1863. doi: 10.1103/PhysRevLett.54.1860.
19. Rappe AK, Goddard WA. Charge equilibration for molecular-dynamics simulations. *J Phys Chem*. 1991;95(8):3358-3363.
20. Streitz FH, Mintmire JW. Electrostatic potentials for metal-oxide surfaces and interfaces. *Physical Review B*. 1994;50(16):11996-12003.
21. Iczkowski R, Margrave JL. Electronegativity. *J Am Chem Soc*. 1961;83(17):3547-&.
22. Parr RG, Pearson RG. ABSOLUTE HARDNESS - COMPANION PARAMETER TO ABSOLUTE ELECTRONEGATIVITY. *J Am Chem Soc*. 1983;105(26):7512-7516.

23. Mulliken RS. A new electroaffinity scale; together with data on valence states and on valence ionization potentials and electron affinities. *J Chem Phys*. 1934;2(11). doi: 10.1063/1.1749394.
24. Oda A, Hirono S. Geometry-dependent atomic charge calculations using charge equilibration method with empirical two-center coulombic terms. *Theochem-J Mol Struct*. 2003;634:159-170. doi: 10.1016/S0166-1280(03)00338-5.
25. DASGUPTA A, HUZINAGA S. New developments in cndo molecular-orbital theory. *Theor Chim Acta*. 1974;35(4):329-340. doi: 10.1007/BF00548482.
26. Tang W, Sanville E, Henkelman G. A grid-based bader analysis algorithm without lattice bias. *J Phys -Condes Matter*. 2009;21(8):084204. doi: 10.1088/0953-8984/21/8/084204.
27. Ewald P. The calculation of optical and electrostatic grid potential. *Ann Phys -Berlin*. 1921;64(3):253-287.
28. McCann BW, Acevedo O. Pairwise alternatives to ewald summation for calculating long-range electrostatics in ionic liquids. *J Chem Theory Comput*. 2013;9(2):944-950. doi: 10.1021/ct300961e.
29. Harrison W. Simple calculation of madelung constants. *Phys Rev B*. 2006;73(21):212103. doi: 10.1103/PhysRevB.73.212103.

30. Baker AD, Baker MD. Rapid calculation of individual ion madelung constants and their convergence to bulk values. *Am J Phys*. 2010;78(1):102-105. doi: 10.1119/1.3243281.
31. Svane A, Kotomin E, Christensen N. First-principles calculations of the vibrational properties of H centers in KCl crystals. *Phys Rev B*. 1996;53(1):24-27. doi: 10.1103/PhysRevB.53.24.
32. Grosso R, Fermann J, Vining W. An in-depth look at the madelung constant for cubic crystal systems. *J Chem Educ*. 2001;78(9):1198-1202.

4.8 Tables and Figures

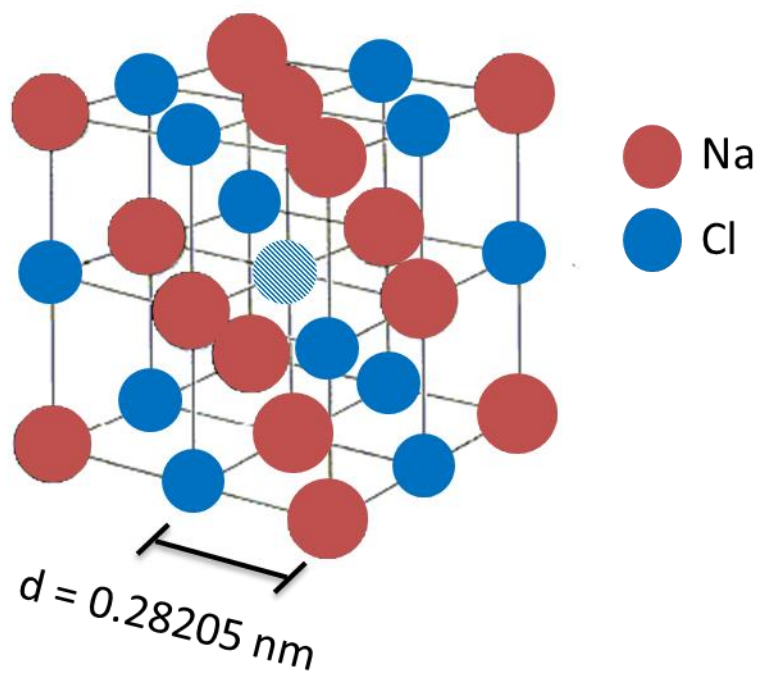


Figure 4.1 Illustration of $\text{Na}_{14}\text{Cl}_{13}^{1-}$ seed structure. Sodium atoms in red; chlorine atoms in blue.

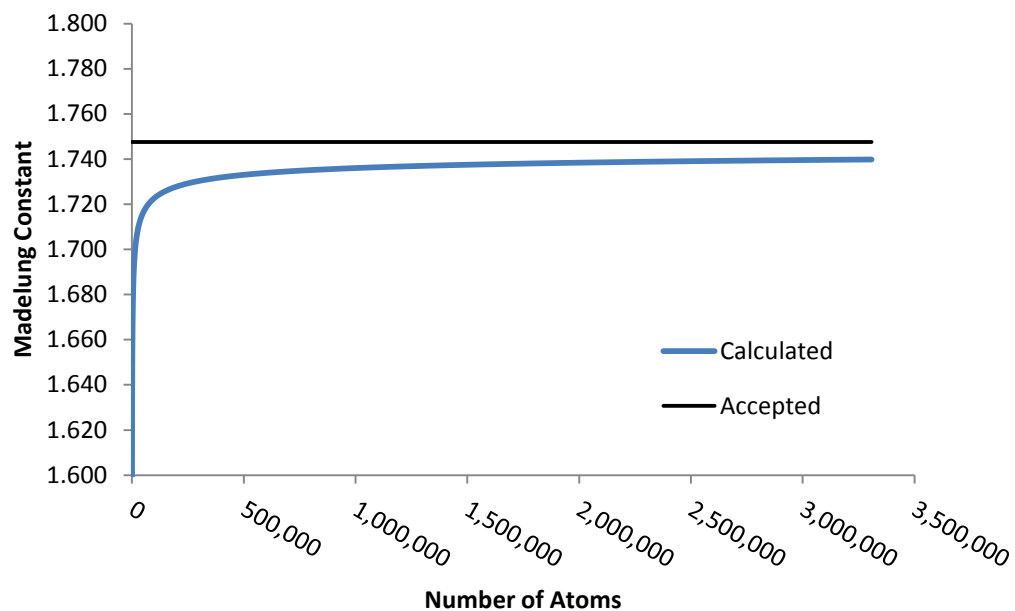


Figure 4.2 Calculated bulk Madelung constant for center sodium atom as a function of the number of atoms in a NaCl lattice seeded by the $\text{Na}_{14}\text{Cl}_{13}$ cube. Experimental value of 1.74756 is denoted in black³².

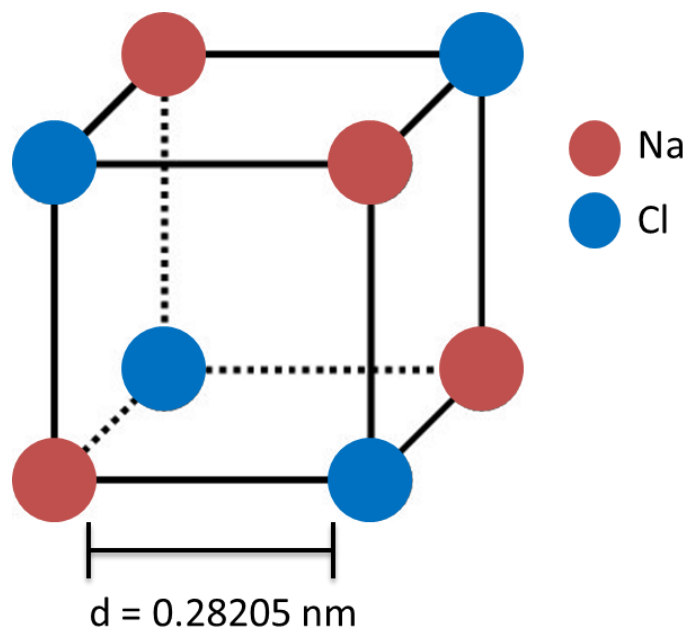


Figure 4.3 Illustration of Na_4C_4^0 seed structure. Sodium atoms in red; chlorine atoms in blue.

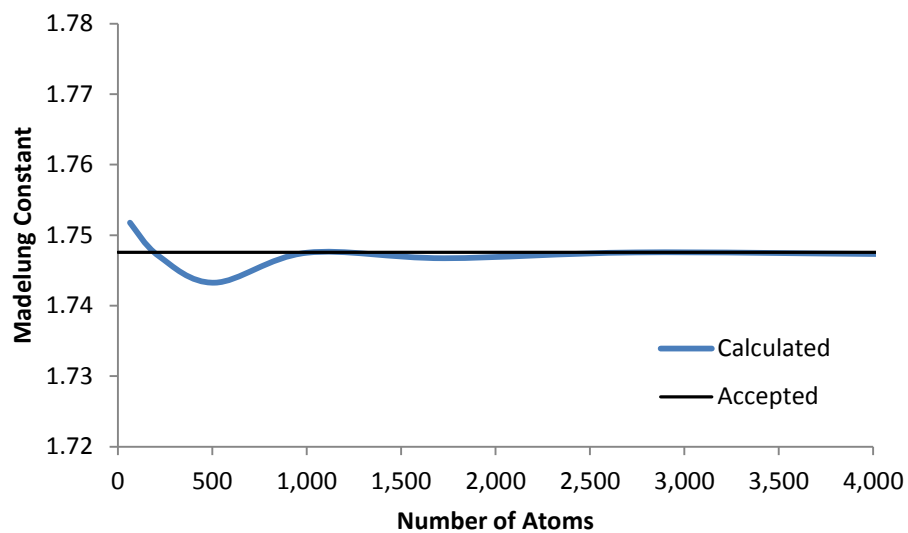
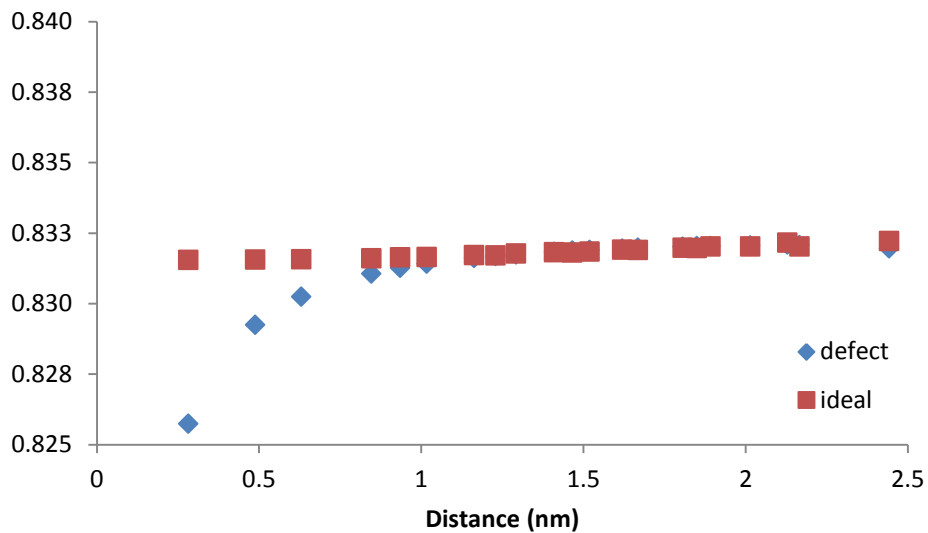
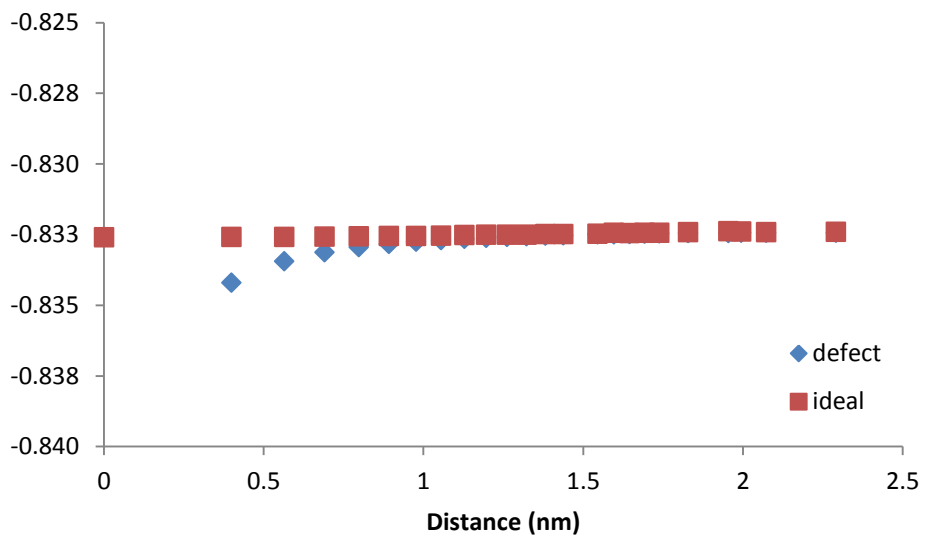


Figure 4.4 Calculated bulk Madelung constant for center sodium atom as a function of the number of atoms in a NaCl lattice seeded by the Na_4Cl_4 cube. Experimental value of 1.74756 is denoted in black³².



(a)



(b)

Figure 4.5 Average charge, in electrons, by radial distance from center site of NaCl cube for (a) sodium atoms and (b) chlorine atoms. Charges labeled in blue refer to the ideal bulk crystal; the red points denote system with an anionic vacancy.

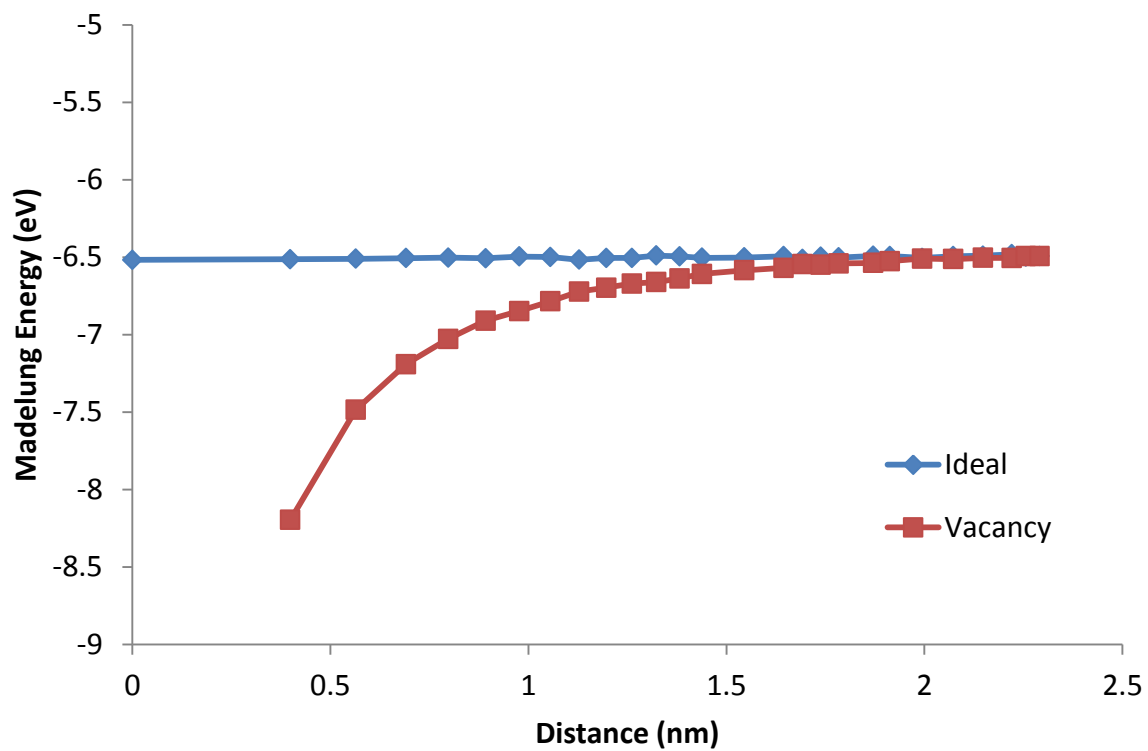


Figure 4.6 Average Madelung energy of chlorine atoms by radial distance from the anionic vacancy in NaCl.

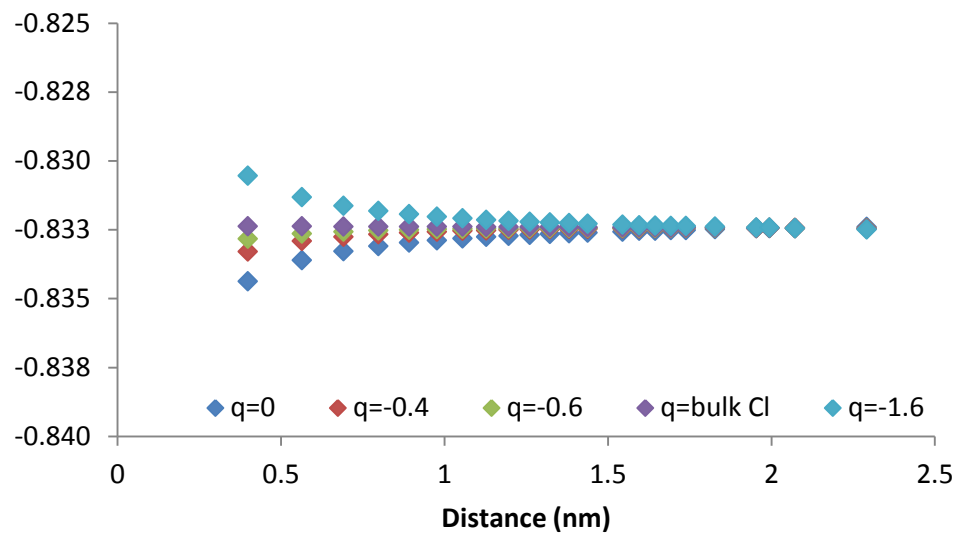


Figure 4.7 Average charges, in electrons, for chlorine atoms by radial distance from the f-center in NaCl as a function of fixed charge localized in the anionic vacancy.

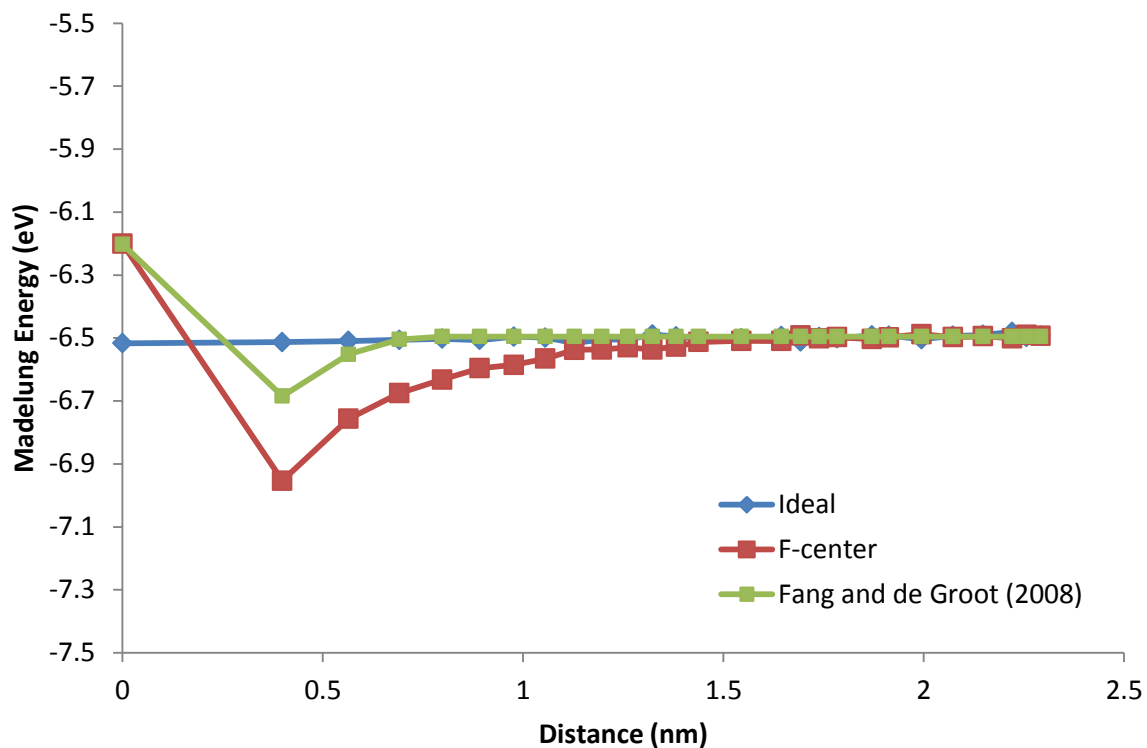


Figure 4.8 Average Madelung energy of chlorine atoms by radial distance from the f-center in NaCl. Points in green are from [17] and have been scaled by a factor of 0.945 for comparison to current data to account for the lower bulk charges computed in [17].

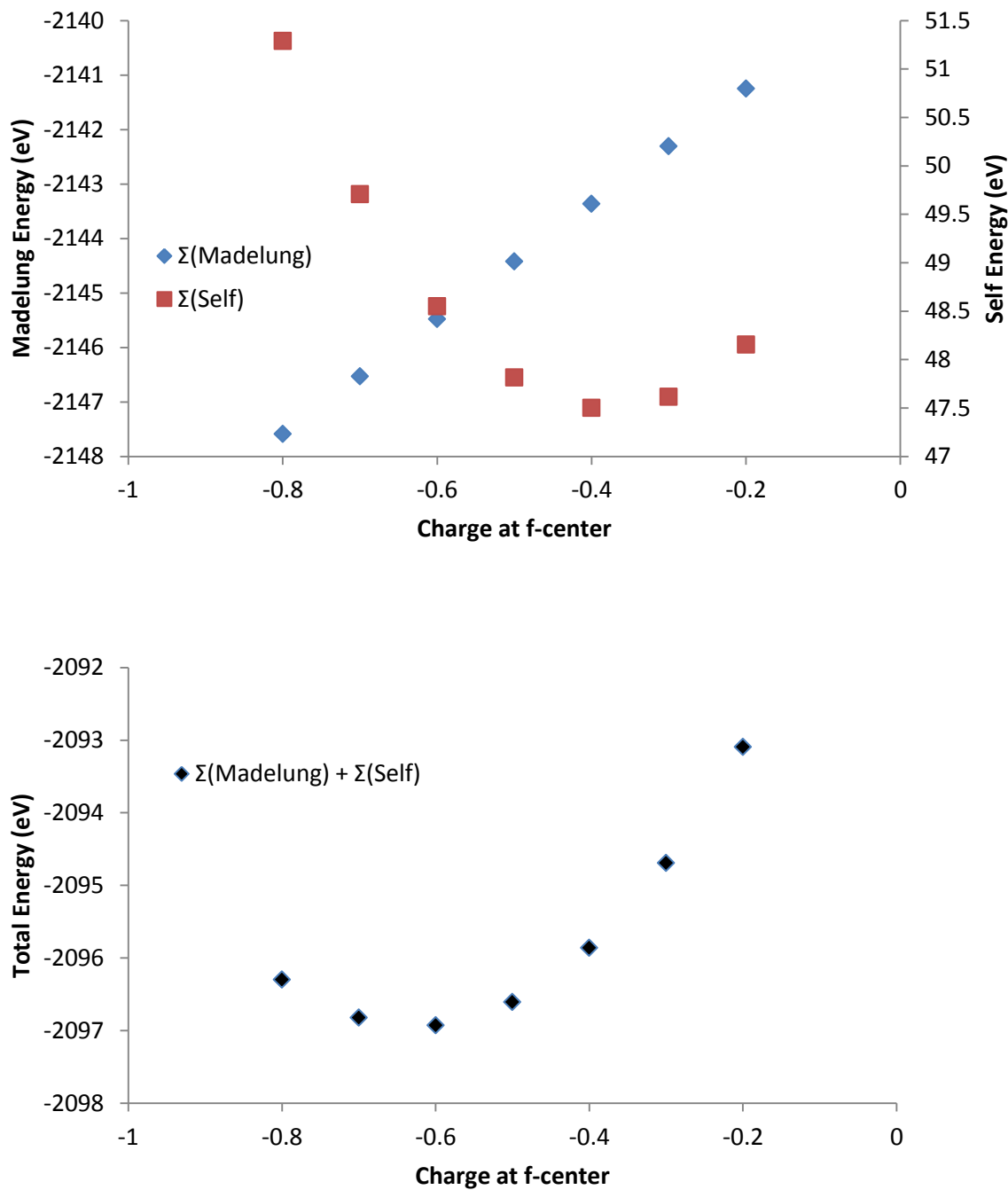


Figure 4.9 Top: Sum of Madelung energies and self-energies for all ions within 1.5 nm of the f-center. Bottom: Total energy (Madelung + self) as a function of f-center charge. The energy summations are reported as a function of fixed charge in the f-center.